ISSN: 0972-8392

INDIAN CARTOGRAPHER

Volume 44 Number 1 & 2 2024

Indian National Cartographic Association
Survey of India, Uppal, Hyderabad – 500 039
Telangana [India]

INDIAN CARTOGRAPHER

ISSN: 0972-8392

A Peer Reviewed Journal of the Indian National Cartographic Association (INCA)

[Founded in 1979]

Survey of India, Uppal, Hyderabad – 500 039 (Telangana, India)

Email: editorinca.journal@gmail.com

Editorial Board [2023-2024]

Subscription

In India : ₹ 1000

Outside India: US $ 25

INDIAN CARTOGRAPHER

A Peer Reviewed Journal of the Indian National Cartographic Association (INCA)

[ISSN: 0972-8392 OCLN No.: 637645018]

Volume 44 Number 1 & 2 2024

Chief Editor

Bimal Kumar Kar

Indian National Cartographic Association

Headquarters: Survey of India, Uppal, Room No. 234, APGDC Block

Hyderabad – 500 039 (Telangana, India)

Email: secretarygeneralinca935@gmail.com / editorinca.journal@gmail.com

Phone & Fax No.: +91-40-2702217 :: Website: https://www.incaindia.org

ISSN: 0972-8392
INDIAN CARTOGRAPHER
Volume 44 Number 1 & 2 2024

Indian Cartographer, Vol. 44, No. 1 & 2, pp. 1-11
ISSN: 0972-8392 © INCA, 2024

Forest Biomass Estimation using Multi Frequency SAR Data

Rakesh Fararoda[1*], Souvik Maji[1], Rakesh Paliwal[1], G. Rajashekar[2], A. K. Bera[1] and S. K. Srivastav[3]
[1]Regional Remote Sensing Centre-West, ISRO, Jodhpur-342005 (India)
[2]Forestry & Ecology Group, National Remote Sensing Centre, ISRO, Hyderabad (India)
[3]Regional Centre, National Remote Sensing Centre, ISRO, New Delhi (India)
Corresponding Author's email: rakesh@nrsc.gov.in

Abstract

Forest biomass and carbon estimates are the key inputs to the understanding of the global carbon cycle and reliable and accurate estimates of tropical forest above ground biomass (AGB) are important for terrestrial carbon accounting, and climate change modeling research. Traditional field-based approaches have been considered the most accurate, but the processes are time consuming, costly and, most importantly, it can only be done in small and accessible regions. Emergence of remote sensing and GIS technique provides methods for reliable AGB estimates at large scales. SAR sensors provide unique opportunities to characterize forest vegetation through its sensitiveness to vegetation structure and all-weather imaging capability over regions of persistent cloud cover. SAR signal is strongly correlated with the forest structure due to volumetric scattering with the tree canopies depending on the operating frequencies. This study explores the potential of multi frequency SAR data for forest biomass assessment in the state of Madhya Pradesh. We used the L-band data from ALOS-2 PALSAR-2 and C-band data from EOS-04 and Sentinel-1. Field Inventory data from the 215 sample plots of 0.1ha size were used for field biomass estimation. The plot-level AGB estimates were empirically modeled with the EOS-04, Sentinel-1, and ALOS PALSAR-2 backscatter information in HH, HV polarization. Cross polarisation backscatter in L band shows better relation than the C band due to saturation of C-band in higher biomass ranges. EOS-04, Sentinel-1 and ALOS-2 PALSAR-2 based models predicts AGB with R^2 of 0.37, 0.41 and 0.59, respectively. Synergistic utilization of the C and L-band improve upon individual bands model and gives a correlation coefficient of 0.64. Total biomass of the study area is estimated as 612.34 million tons with synergistic utilization of C and L-band with an estimation error of 28.98.

Keywords: Above Ground Biomass, SAR, EOS-04, ALOS-2 PALSAR-2.

Introduction

Forest stores carbon in the form of biomass (Gibbs et al., 2007) and plays a significant part in preserving the world carbon cycle and controlling the earth's climate (Pan et al., 2011). Therefore, accurate measurement of forest biomass is crucial for maintaining the carbon accounting, climate change mitigation plans, and for sustainable forest management (Zhang et al., 2015).

Traditional approaches for estimating biomass include destructive sampling and allometric equations, among others. The field measurement has been proven to give accurate estimate and a pre-requisite to generate any biomass database but is destructive in approach, time consuming and expensive (Gier et al., 2003, Kumar et al., 2017). Remote sensing methods are non-destructive and have many advantages, viz. synoptic view, large area and multi-temporal coverage, etc. and greatly increase efficiency (Patenaude et al., 2005; Balsamo et al., 2018; Xiao et al., 2019), thereby overcoming some of the challenges associated with field measurement. As a result, remote sensing techniques have emerged as a viable

option for precise and cost-effective biomass assessment using optical and microwave remote sensing data (Nandy et al., 2017; Muukkonen et al., 2007; Padalia et al., 2023; Das et al., 2024). Remote sensing data are being integrated with field data to generate precise and comprehensive spatial estimations of forest biomass (Lu 2005; Fararoda et al., 2021). However, the accuracy of such remote sensing based method largely depend on the robustness of the field inventory data and sampling design (Rajashekar et al., 2017, Chave et al., 2014).

Optical RS is used to retrieve forest variables based on reflectance from individual bands, band ratios and normalized vegetation indices (Zhang et al., 2014). Microwave signal interact with forest canopies, penetrate deep into the canopies based on the operating wavelength and returning backscatter signal is used to correlate with forest biomass. Forest biomass is stored in multiple canopy stories and passive optical sensors interact with the top of the surface feature leaving understory vegetation properties unaddressed (Joshi et al., 2016). Spectral saturation of the optical sensors is also observed in the high biomass region (Lu et al., 2005). The persistent cloud conditions in tropical forests limits the standalone uses of optical data and their applications often ends up in unreliable AGB estimate and tends to underestimate in high biomass regions. The Synthetic Aperture Radar (SAR) systems operating in microwave region of the electro-magnetic spectrum (EMS) have the advantage over optical data sets as it can see through the clouds as tropical forests are often cloud infested. SAR systems are capable to penetrate through vegetation cover depending on wavelength used, and collects structural information of the vegetation that is more relevant to the biomass (Huang et al., 2018).

So far X, C, L and P band SAR data have been extensively used in retrieving forest parameters. Radar scattering mechanism is controlled by the particle size and radar wavelength. Short wavelengths are scattered by smaller constituents of trees such as leaves and branches, whereas the longer wavelengths are scattered by components such as trunks. This leads to saturation of the smaller wavelength signals such as C and X-band at relatively low-AGB forests, whereas the saturation of the longer wavelength such as L and P-band are observed at relatively higher AGB. For this reason, X and C-band SAR were predominantly utilized for assessment of forest canopy characterization (primary interaction with top canopy layer due to less penetration capacity). Low wavelength radar systems such as Sentinel and RadarSAT and Terra-X SAR are mainly used to estimate the AGB in low biomass regions (e.g., sparse savannas), shrublands, grasslands, or agricultural crops (Das et al., 2024).L-band and P-band SAR sensors are therefore preferred over smaller wavelengths as longer wavelengths radar signal can penetrate the tree canopy and interact with larger woody components (stems and branches) of the forest (Le Toan et al., 1992).

The open access availability of dual pol L-band global mosaic from JAXA has provided opportunities for large scale AGB mapping and several studies have noted saturation of L-band datain high biomass regions. Bouvet et al. (2018) used 2010 PALSAR-2 mosaics and observed the saturation of the L-band data in regions with AGB over 85 Mg/ha to estimate woody AGB in African savannahs and woodlands using Bayesian methods and. Hame et al. (2013)used L-band effectively in mapping AGB in Laos with dense tropical forest. Shugart et al. (2010) found L-band synthetic aperture radar data saturated in the AGB range of 100–150 Mg ha^{-1}. However, upcoming P-band BIOMASS mission from ESA will be capable of estimating AGB in high biomass regions more effectively (Le Toan et al., 2011).

Earlier studies reported the uses of different SAR sensors in reliably mapping forest AGB over Indian forests. Thumaty et al. (2016)used L-band ALOS PALSAR data to spatially estimate the forest biomass the central Indian deciduous forest in the state of Madhya Pradesh for the Year 2010. Study shows the HV backscatter in L-band is strongly correlated with forest biomass. Suresh et al. (2014) also used L-band SAR data for forest type mapping and biomass estimation for the state of Odisha. C and L-band data has been used in isolation for AGB estimation over Indian forest (Padalia et al., 2017; Thumaty et al., 2016; Suresh et al., 2014; Das et al., 2024). However, synergistic utilization of C and L-band for AGB estimation over Indian forests in relatively less explored. Considering the availability of the C and L-band data and their individual advantages, in this study we explored the synergistic utilization of the C and L-band data for AGB estimation in the low to medium AGB forest of the Madhya Pradesh.

Materials and Methods

The Study Area

The study is carried out in the forest of the state of Madhya Pradesh. Madhya Pradesh is the second largest state of India having large diverse forest reserves with enormous

biodiversity. It lies in between 74.03° east to 82.81° east longitude and 26.86° north to 21.07° north latitudes. The spatial extent of the state is 308,144 km^2 of which 77,493 km^2 (~25.14% of the TGA) is under forest cover. The state of Madhya Pradesh has the largest forest cover followed by Arunachal Pradesh and contributes 10.85% of the forest area of the country. The major forest types present in the state are Tropical Moist, Tropical Dry, Tropical Thorn and Subtropical broad leaved hill forest. Figure 1 shows the study area and distribution of the field plots.

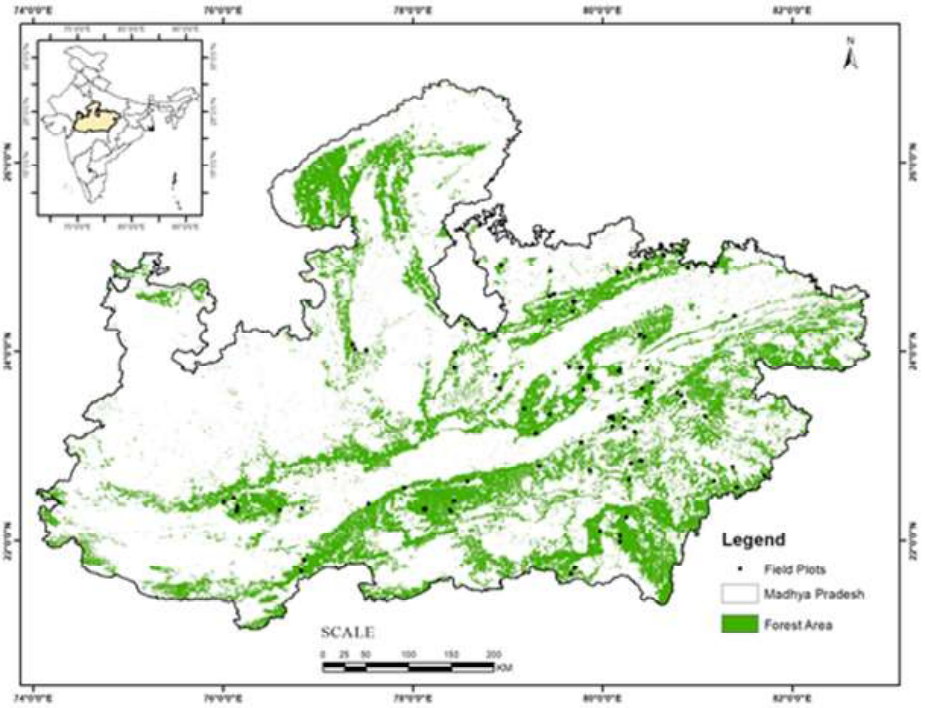

Fig. 1: Study area (Madhya Pradesh) and field plots overlaid on forest cover

Field Inventory

Ground inventory data from 215 plots of 0.1ha size were used for biomass estimation. Field measured variables such as diameter, tree height, and species scientific name were recorded for all trees with DBH> 10 cm during field inventory during 2018-19. Field Inventory data were collected as part of the National Field Inventory carried out under the National Carbon Project, Vegetation Carbon Pool Project phase-II during 2018-2019 (ISRO-Geosphere Biosphere Programme). Field measured variable such as diameter and species information were used to estimate the tree volume using species specific volumetric equations developed by Survey of India (FSI, 1996). Further, stem volume was converted to total tree biomass using wood ded biomass expansion factors.

$$AGB = Volume \times WD \times BEF \quad \text{(Brown and Lugo 1992)} \quad (1)$$

Where, volume is estimated through volumetric equations developed by FSI, WD is wood density and BEF is biomass expansion factor.

Species specific volume equations were used for volume equation database created by FSI (FSI, 1996), wood density data were used from Indian Woods database (FRI, 1996) and Biomass expansion factors were derived from Kaul et al. (2011). Plot AGB was obtained as sum of the all trees sampled within the 0.1ha size of the plot. Field measured biomass from these 215 sample field plots were correlated with HH and HV backscatter. Field measured biomass was regressed against HH and HV backscatter of C- and L-band SAR data.

SAR Data Processing

SAR data in the C and L-band were used for the AGB estimation. C-band data were used from the EOS-04 and Sentinel-1, while L-band data were sued from the ALOS-2 PALSAR-2 sensor. Level 2 orthorectified and radiometrically terrain-corrected ALOS-2 PALSAR-2 data were obtained from Google Earth Engine. Additionally, the Level 2 enhanced georeferenced product of EOS-04 was acquired through the Bhoonidhi web

portal (https://bhoonidhi.nrsc.gov.in), of National Remote Sensing Centre (NRSC), ISRO. EOS-04 is a follow-on mission to the earlier RISAT-1 mission with similar specifications that was operated during April 2012–September 2016 (Misra et al., 2013).SAR data were calibrated and processed for speckle filtering. The downloaded SAR data were converted to backscatter using the following calibration equations (equation 2 & 3 for EOS-04 and ALOS-1PALSAR-2, respectively):

$$\sigma^\circ = 10\log_{10}(DN^2) + 10\log_{10}(\sin i_p) - K_{dB} \quad \text{(SAC, 2023)} \quad (2)$$

Where, Sigma-Naught (dB), DN, i_p and K_{dB} arebackscattering coefficient, digital number, per pixel incidence angle and calibration constant, respectively.

$$\sigma^\circ = 10\log_{10}(DN^2) - 83 \quad (3)$$

Where, Sigma-Naught (dB) is the radar backscatter coefficient in dB, DN is a digital number of the input image, and "83 is the calibration constant (Motohka et al., 2018).

Level 1 Ground Range Detected (GRD) products of Sentinel-1A with two polarization images (VV and VH), were downloaded for the December of 2019 to match the time of field inventory. Sentinel Application Platform (SNAP toolbox) was used to process the Sentinel-1A GRD data for sigma naught.

AGB Modelling

Plot level AGB measured through field inventory were correlated with cross and co-polarized backscatter values from different sensors. Single and multiple non-linear regression models were considered for the AGB modeling. Total of 215 field plots were correlated with C-band data from EOS-04 and Sintinel-1 and L band data from the ALOS-2 PALSAR-2. Methodology flowchart is shown in the Fig. 2. The cross-polarization (HV & VH) data are more sensitive to the canopy structure and less susceptible to noise and interference (Sinha et al., 2020; Tian et al., 2023). Correlation between field measured biomass and different combination SAR sensors such as: (1) EOS-04 data (C-band) alone (2) Sentinel-1 data (C-band) alone (3) ALOS-2 PALSAR-2 data (L-band) alone (4) combination of ALOS-2 PALSAR-2 and EOS-04 and (5) combination of ALOS-2 PALSAR-2 and Sentinel-1, were explored for AGB modeling.

The model performance was assessed using the root mean squared error (RMSE) and the coefficient of determination (R^2). The model with the high R^2 value and the low RMSE was finally chosen for the spatial AGB mapping. Root mean square error (RMSE) was calculated by using field measured and modeled AGB as follows:

$$RMSE = \sqrt{\sum_{n=1}^{N} (AGB_{modelled\ (i)} - AGB_{measured\ (i)})^2 / N} \quad (4)$$

Where, N is the number of sample plots, $AGB_{modelled\,(i)}$ is the modelled AGB and $AGB_{measured(i)}$ is the field measured biomass.

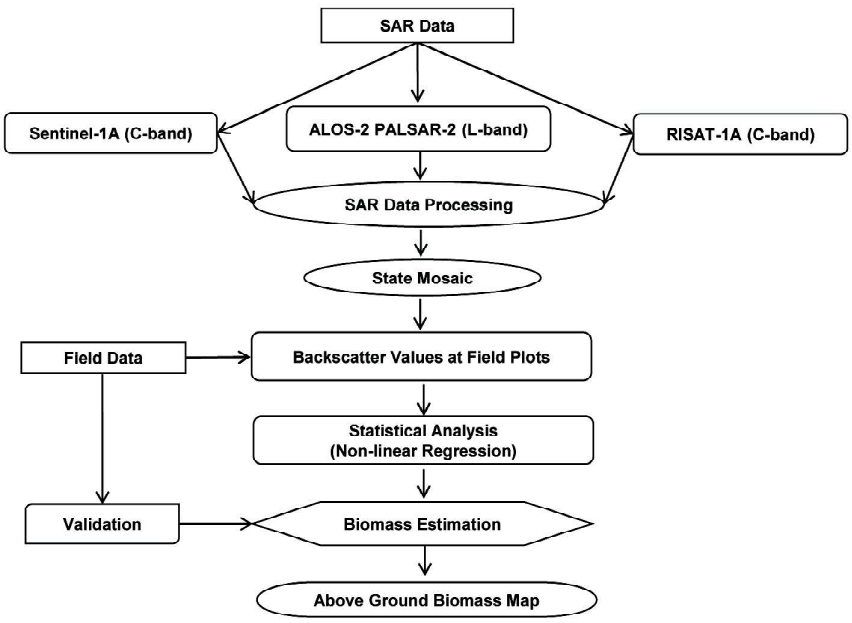

Fig. 2: Methodology Flowchart

Results

SAR images from the different sensors were radiometric calibrated and speckle filtered before generating the state level mosaic. Field measured biomass in the study area varies upto 262 Mg ha^{-1} with a mean AGB density of 83.61 Mg ha^{-1} with majority of the field plots falling below the saturation range of the L-band data. Since the study area falls in the low to medium biomass range, 85 % of the total plots have the biomass below the 150 Mg ha^{-1} while remaining 15 % plots have the biomass above 150 Mg ha^{-1}.

Non linear regression and multiple non-linear regression models were trained on field plots with C- & L-band and their combination. Cross-polarized backscatter was found to be strongly correlated with field biomass as compared to co-polarized backscatter at both the frequencies. EOS-04 HV backscatter gives a R^2 of 0.37 against the R^2 of 0.41 with the Sentinel-1 VH backscatter. ALOS-2 PALSAR-2 HV backscatter gives better R^2 of 0.59 with a RMSE of 33.7 Mg ha^{-1}. Better correlation with L-band is attributed to the deeper penetration into the forest canopies as compared to C-band. C-band found to be saturate faster under the forest canopies in the medium-high biomass ranges. Combined utilization of the C and L-band improved upon the individual bands in term of R^2 and RMSE. C-band data better discriminate in the low biomass regions while L-band data gives better description of the medium-high biomass region leading to better forest AGB estimation by combining C- and L-band data.

Multiple non-linear model using Sentinel-1 and L-band data predicts AGB with RMSE of 28.98 Mg ha^{-1} and R^2 of 0.64 while EOS-04 and L-band gives RMSE and R^2 of 30.17 and 0.61, respectively. Table 1 shows the comparison of different AGB models and their estimated AGB values. Finally the best model in terms of RMSE and R^2 is sued for spatial biomass mapping for the state of Madhya Pradesh and estimated the total AGB in the state as 612.35 million tons. Fig. 2 shows the correlation between the field measured AGB values and the combined backscatter values in the cross polarization from the ALOS-2 PALSAR-2 and Sentinel-1 data.

Table 1: Model parameters R^2, RMSE, model form and the model estimated AGB

Data Used	R^2	RMSE (Mg ha^{-1})	AGB Model	Estimated AGB (Millions Tons)
C-Band (Sentinel-1)	0.41	74.01	$AGB = EXP(\sigma_{s1VH} * 0.3027 + 9.4463)$	617.03
L-Band (ALOS-2 PALSAR-2)	0.59	33.70	$AGB = EXP(\sigma_{alosHV} * 0.2114 + 97.3124)$	585.47
C-Band (Risat-1a)	0.37	72.49	$AGB = EXP(\sigma_{eos\,04HV} * 0.2828 + 8.581)$	579.29
Sentinel-1 & ALOS-2 PALSAR-2	0.64	28.98	$AGB = EXP((\sigma_{s1VH} + \sigma_{alosHV}) * 0.1534 + 9.1254)$	612.34
Risat-1A & ALOS-2 PALSAR-2	0.61	30.17	$AGB = EXP((\sigma_{s1HV} + \sigma_{alosHV}) * 0.1496 + 8.7303)$	592.59

Best performing model using Sentinel-1 and ALOS-2 PALSAR-2 was finally used for AGB mapping..

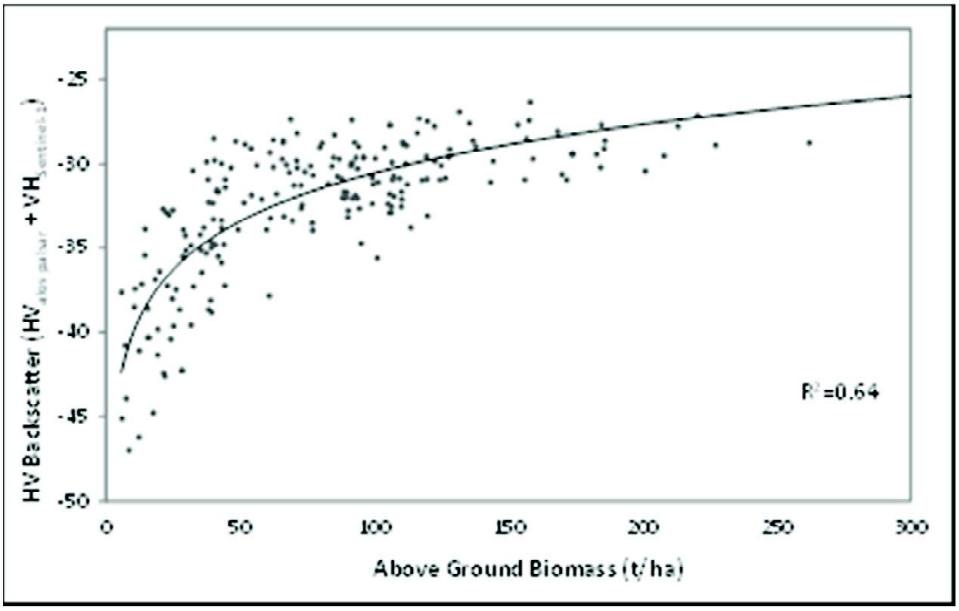

Fig. 3: Scatterplot showing the relation between SENTINEL-1 & ALOS-2 PALSAR-2 backscatter & Biomass

Fig. 4 shows the map of spatial distribution of the AGB in the forest of the Madhya Pradesh. Nearly 82 % of the area is mapped in the biomass below 150 Mg ha^{-1} while 18 % area is mapped with AGB>150 Mg ha^{-1}. Larger area with AGB<150 Mg ha^{-1} is also attributed to the SAR signal saturation beyond the AGB>150 Mg ha^{-1} leading to higher biomass regions getting mapped into AGB < 150 Mg ha^{-1}. Most of the high biomass regions are found the in the south-eastern part while north western par is covered in the low biomass range. Northern region of the state is dominated by the Open dry deciduous forest and host most of the low biomass forests. Moist deciduous forest in the south-eastern region hosts most of the high biomass forests of the state.

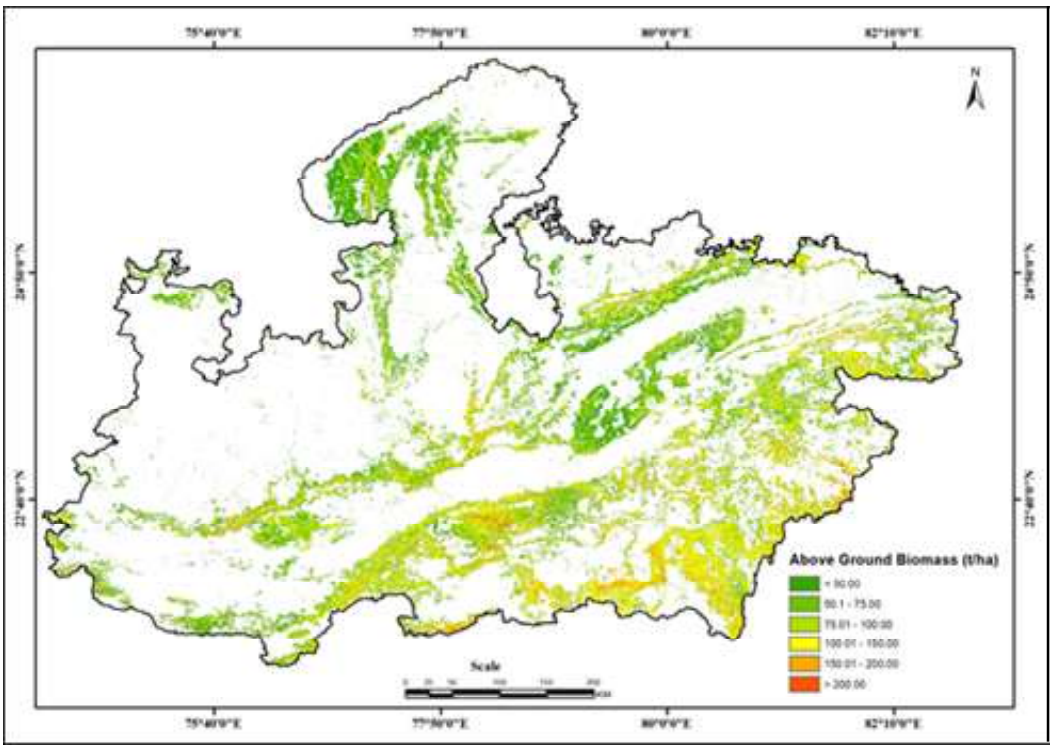

Fig. 4: Map showing the spatial distribution of the above ground biomass

Discussion

Backscatter from HV polarization is found to be more effective in characterizing forest biomass compared to other polarizations (Dobson et al. 1992) due to its better dynamic range of backscatter values over forest regionsas compared to other polarizations obtained in C-, L- and P-bands (Le Toan et al. 1992). Cross polarization backscatter is strongly correlated with biomass density due to volumetric scattering mechanism with tree canopies which is less prominent in the co-polarized data.

C-band operates in the small wavelength and interacts mostly with the leaves and small branches of the top canopies. C-band backscatter values saturates in the range of 70-80 tons as C-band data cannot penetrate deeper into the dense canopies. The linear regression model between AGB and cross-polarized backscatter has a R^2 value as 0.37 and 0.40 for EOS-04 and Sentinel-1 respectively. L-band is more sensitive to biomass as the penetration power of L-band is more than the C-band, and predicts the AGB with R^2 and RMSE of 0.59 and 33.70 Mg ha^{-1}, respectively. This shows that with the help of L-band the biomass can be estimated more accurately compared to the C-band.

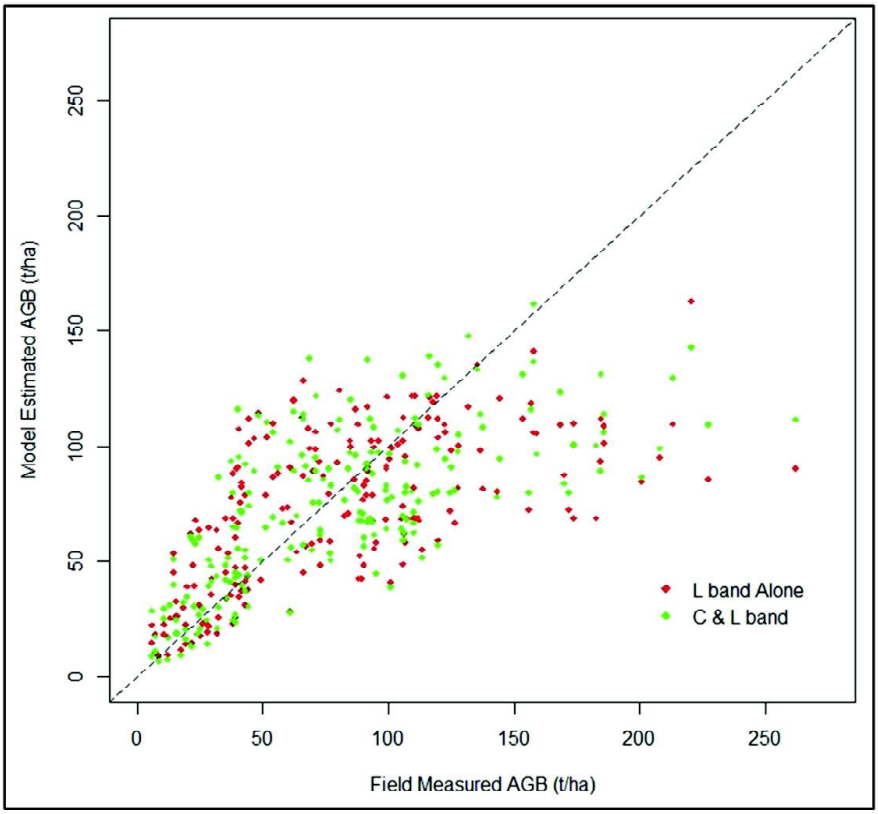

Fig. 5: Validation of measured AGB with model estimated AGB over different vegetation types

In this study, field Inventory data was collected during the 2018-19. Sentinel-1 and ALOS-2 PALSAR-2 data were used for the year 2019 while EOS-04 data was used from the year 2022. Temporal mismatch between the field measurement and Satellite data acquisition could be the reason for relatively poor correlation with the EOS-04 data as compared to the Sentinel-1 as both are operating at the similar frequencies. Concurrent use of the field inventory and EOS-04 data in the future will improve the estimation accuracy.

C- Band remains more sensitive to low biomass reason due to its interaction with the leave and small branches in the top canopies while L-band interact mostly with the branches and the stem. It has been reported in the literature that combination of the C- & L-band can improves the AGB estimation in the low-medium biomass range (Cartus et al., 2017; Musthafa & Singh, 2022) by utilizing their individual strengths. We use multiple regressions using C and L-band cross-polarization backscatter to predict the AGB. Combined utilization of C- and L-band improves the model accuracy upon individual bands and gives R^2 and RMSE of 0.61 and 30.17 Mg ha^{-1} for the combination of ALOS-2 PALSAR-2 and EOS-04 while R^2 and RMSE of 0.64 and 28.98 Mg ha^{-1} for the combination of ALOS-2 PALSAR-2 and Sentinel-1. Inclusion of C band data from the EOS-04 and Sentinel-1 along with the L-band data improves the model accuracy especially in the low biomass regions.

Fig. 5 shows the comparison of the field measured and model estimated AGB values at plot level. It is observed that the Model based on the C and L-band saturates in AGB>150 Mg ha^{-1} and gives poor AGB estimation in these areas. Model predicts lower AGB values in the all plots with AGB>150 Mg ha^{-1}. Comparison of field measured AGB over sample plots shows that 190 plots have AGB<150 Mg ha^{-1} while 25 plots are with AGB>150 Mg ha^{-1}. On the other hand, AGB model predicts the AGB<150 Mg ha^{-1} in the 211 plot while estimating AGB>150 Mg ha^{-1} in the only 4 plots (As shown in the Fig. 6).

This shows the clear saturation of the model in AGB>150 Mg ha^{-1}. Field measurements of the biomass shows 75 plot with AGB<50 Mg ha^{-1} whereas model estimated AGB shows 56 plots with AGB<50 Mg ha^{-1} indicating significant overestimation over-estimation in the lower biomass regions.

Past studies have reportedthe similar saturation of the radar backscatter in high biomass regions depending on the wavelength used, resulting in a logarithmic or sigmoidal relationship of AGB with backscatter (Saatchi et al., 2011, Le Toan et al., 2011). C–band data founds to saturate beyond 70 Mg ha^{-1}. Analysis on the airborne AIRSAR and E-SAR data reveals that SAR signal saturation for L-band (15–30 cm wavelength) may vary between 80 and 150 Mg ha^{-1}while for P-bands, at ~70 cm wavelength it is observed in the range of 200–350 Mg ha^{-1} (Le Toan et al., 2011, Mitchard et al., 2009, Bouvet et al., 2018, Mermoz et al., 2015; Fararoda et al., 2021). Mitchard et al. (2009) found co-polarized L-band data useful to map AGB upto 150 Mg ha^{-1}across several sites of woody vegetation.

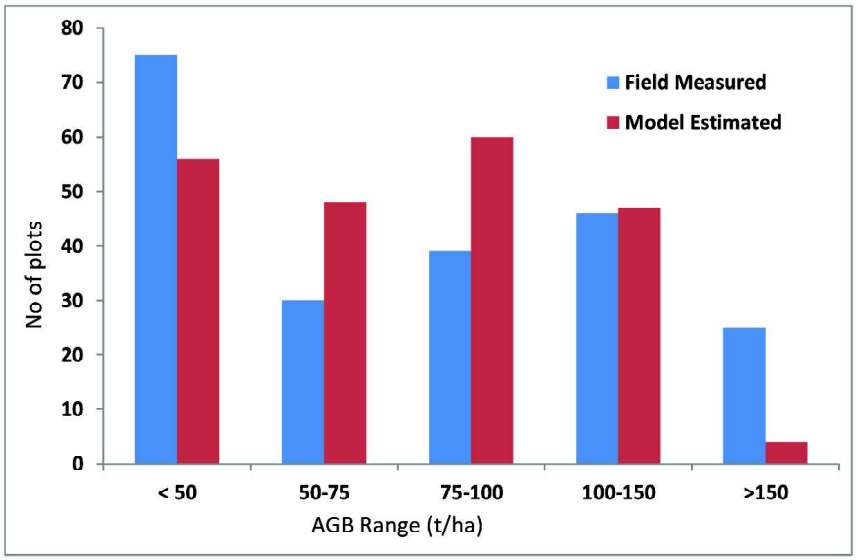

Fig. 6: Distribution of the measured and model estimated AGB at the sample plots.
Figure shows that some of the plot in very low and very high biomass range are mapped into the medium biomass range showing underestimation in the high and over-estimation in the low biomass regions

The study area is mainly covered by tropical moist and dry deciduous forests, followed by Teak (*Tectonagrandis*), mixed deciduous forests and Sal (*Shorearobusta*) forests (Thumaty et al., 2016). Spatial analysis of the model predicted AGB shows large difference in the predicted AGB over different forest regions. High-biomass regions are mapped in the central and south-eastern region while the northern region in dominated by the low biomass region. Low biomass northern and western part of the forests are dominated by open dry deciduous forest while dense sal forest in the south-eastern region host the highest biomass density in the state. Nearly 30 % of the area of the state with AGB < 50 Mg ha^{-1} contributes only 11.5 % to the states total AGB due to its low biomass density while only 7.5 % area with AGB > 150 Mg ha^{-1} contributes 18% to the states total AGB. 62 % forest area of the state falls in the medium biomass range of 50-150 Mg ha^{-1}. AGB range-wise comparison of area and their AGB contribution is given in the Table 2.

Table 2: AGB range wise distribution of the forest area and their contribution of the total AGB of the state

Class	Biomass Range	Area Contribution (%)	AGB contribution (%)
1	0-50	30.05	11.48
2	50-100	40.76	37.95
3	100-150	21.60	32.40
4	150-200	5.47	11.52
5	above 200	2.12	6.65

Conclusion

The study suggests that SAR data is suitable for estimating AGB in low to medium biomass forests up to the AGB of 150 Mg ha^{-1}. We explored the utilization of backscatter from C and L-band to enhance the AGB estimation in the low- medium AGB regions. Empirical models shows that C- and L-band based model gives of R^2 for 0.37, 0.41, and 0.59 for EOS-04, Sentinel-1 and ALOS-2 PALSAR-2, respectively. The results indicated that the combined use of C- and L-band data out-performed the models relying solely on either data source. The integrated model using ALOS-2 PALSAR-2 and Sentinel-1 predicts AGB with a RMSE of 28.98 Mg ha^{-1} and R^2 of 0.64. The present study highlights the potential of synergestic utilization of multi-frequency SAR data for enhanced AGB estimation at large spatial scale. C-band data alone give poor AGB estimates due to its saturation in high biomass regions, but significantly enhance the AGB estimation when used in conjunction with L-band data. Relatively poor correlation with EOS-04 data as compared to the Sentinel-1 is due to the temporal difference in the field data collection and the date of SAR data acquisition which can be minimized in the future studies. Methods presented here and the findings of the study are significant contribution in the context of the upcoming NISAR mission which will provide S and L-band. Further, the anticipated availability of SAR data in the P-band from the BIOMASS mission along with NISAR will enhance the SAR data utilization in the high biomass regions.

References

Balsamo, G., Agusti-Parareda, A., Albergel, C., Arduini, G., Beljaars, A., Bidlot, J., et al. (2018). Satellite and in situ observations for advancing global Earth surface modelling: A review. Remote Sensing, 10(12), 2038. https://doi.org/10.3390/rs10122038

Bouvet, A.; Mermoz, S.; Le Toan, T.; Villard, L.; Mathieu, R.; Naidoo, L.; Asner, G.P. (2018). An above-ground biomass map of African savannahs and woodlands at 25 m resolution derived from ALOS PALSAR. Remote Sens. Environ. , 206, 156–173.

Brown, S., and Lugo, A.E.(1992). Aboveground biomass estimates for tropical moist forests of the Brazilian Amazon. Interciencia. Caracas, 17(1), pp.8-18.

Cartus, O., Santoro, M., Wegmüller, U., & Rommen, B. (2017). Estimating total aboveground, stem and branch biomass using multi-frequency SAR. In 2017 9th International Workshop on the Analysis of Multitemporal Remote Sensing Images (MultiTemp) (pp. 1–3). IEEE. https://doi.org/10.1109/Multi-Temp.2017.8035231.

Chave, J., Réjou Méchain, M., Búrquez, A., Chidumayo, E., Colgan, M.S., Delitti, W.B., Duque, A., Eid, T., Fearnside, P.M., Goodman, R.C. and Henry, M.,(2014). Improved allometric models to estimate the aboveground biomass of tropical trees. Global change biology, 20(10), pp.3177-3190.

Das, A.K., Patnaik, C., Maity, S., Praveen, M.S.S., Reddy, R.S., Rajashekar, G., Chaube, N.R., Mahajan, S., Jain, Y., Bhavsar, D. and Chakraborty, K.(2024. Estimation of above-ground biomass and delineation of vegetation of tropical forests using EOS-04 data. Current Science (00113891), 126(9).

Dobson, M.C.; Pierce, L.; Sarabandi, K.; Ulaby, F.T.; Sharik, T. (1992).Preliminary analysis of ERS-1 SAR for forest ecosystem studies. IEEE Trans. Geosci. Remote Sens. 1992, 30, 203–211.

Fararoda, R., Reddy, R. S., Rajashekar, G., Chand, T. K., Jha, C. S., & Dadhwal, V. K. (2021). Improving forest above ground biomass estimates over Indian forests using multi source data sets with machine learning algorithm. Ecological Informatics, 65, 101392. https://doi.org/10.1016/j.ecoinf.2021.101392

FSI (1996). Volume Equations for Forests of India, Nepal and Bhutan Forest Survey of India. Ministry of Environment and Forests, Govt. of India, Dehradun.

FRI (1996). Indian Woods: Their Identification, Properties and Uses. Volume I-VI. ForestResearch Institute, Ministry of Environment and Forests, Dehra Dun, India.

Gibbs, H.K., Brown, S., Niles, J.O. and Foley, J.A. (2007). Monitoring and estimating tropical forest carbon stocks: making REDD a reality. Environmental research letters, 2(4), p.045023.

Gier, A. de. (2003). A new approach to woody biomass assessment in woodlands and shrublands. Geoinformatics Trop. Ecosyst., 161–198.

Hame, T.; Rauste, Y.; Antropov, O.; Ahola, H.A.; Kilpi, J. (2013). Improved mapping of tropical forests with optical and SAR imagery, Part II: Above ground biomass estimation. IEEE J. Sel. Top. Appl. Earth Obs. Remote Sens. , 6, 92–101.

Huang, X.; Ziniti, B.; Torbick, N.; Ducey, M.J. (2018). Assessment of forest above ground biomass estimation using multi-temporal C-band sentinel-1 and polarimetric L-band PALSAR-2 data. Remote Sens. 10, 1424.

Joshi, N.; Baumann, M.; Ehammer, A.; Fensholt, R.; Grogan, K.; Hostert, P.; Jepsen, M.R.; Kuemmerle, T.; Meyfroidt, P.; Mitchard, E.T.A.; et al. (2016). A review of the application of optical and radar remote sensing data fusion to land use mapping and monitoring. Remote Sens. 8, 70.

Kaul, M., Mohren, G.M.J., Dadhwal, V.K., (2011). Phytomass carbon pool of trees andforests in India. Clim. Change 108, 243–259

Kumar, L. and Mutanga, O., (2017). Remote sensing of above-ground biomass. Remote Sensing, 9(9), p.935.

Le Toan, T.; Beaudoin, A.; Riom, J.; Guyon, D. Relating forest biomass to SAR data. IEEE Trans. Geosci. Remote Sens. 1992, 30, 403–411.

Le Toan, T.; Quegan, S.; Davidson, M.W.J.; Balzter, H.; Paillou, P.; Papathanassiou, K.; Plummer, S.; Rocca, F.; Saatchi, S.; Shugart, H.; et al. (2011). The BIOMASS mission: Mapping global forest biomass to better understand the terrestrial carbon cycle. Remote Sens. Environ. 2011, 115, 2850–2860.

Lu, D. (2005). Aboveground biomass estimation using Landsat TM data in the Brazilian Amazon. Int. J. Remote Sens. 26, 2509–2525.

Misra, T., Rana, S.S., Desai, N.M., Dave, D.B., Rajeevjyoti, Arora, R.K., Rao, C.V.N., Bakori, B.V., Neelakantan, R. and Vachchani, J.G. (2013). Synthetic Aperture Radar payload on-board RISAT-1: configuration, technology and performance. Current Science, pp.446-461.

Mermoz, S.; Réjou-Méchain, M.; Villard, L.; Le Toan, T.; Rossi, V.; Gourlet-Fleury, S. (2015). Decrease of L-band SAR backscatter with biomass of dense forests. Remote Sens. Environ. , 159, 307–317.

Mitchard, E. T., Saatchi, S. S., Woodhouse, I. H., Nangendo, G., Ribeiro, N. S., Williams, M., et al. (2009). Using satellite radar backscatter to predict above-ground woody biomass: A consistent relationship across four different African landscapes. *Geophysical Research Letters, 36*(23), L23401. https://doi.org/10.1029/2009GL040692

Motohka, T., Isoguchi, O., Sakashita, M., & Shimada, M. (2018). Results of ALOS-2 PALSAR-2 calibration and validation after 3 years of operation. In IGARSS 2018–2018 IEEE International Geoscience and Remote Sensing Symposium (pp. 4169–4170). IEEE. https://doi.org/10.1109/IGARSS.2018.8519118.

Musthafa, M., & Singh, G. (2022). Improving forest above-ground biomass retrieval using multi-sensor L-and C-Band SAR data and multi-temporal spaceborne LiDAR data. Frontiers in Forests and Global Change, 5, 822704. https://doi.org/10.3389/ffgc.2022.822704

Muukkonen, P.; Heiskanen, J. (2007). Biomass estimation over a large area based on standwise forest inventory data and ASTER and MODIS satellite data: A possibility to verify carbon inventories. Remote Sens. Environ. 107, 617–624.

Nandy, S., Singh, R., Ghosh, S., Watham, T., Kushwaha, S. P. S., Kumar, A. S., & Dadhwal, V. K. (2017). Neural network-based modelling for forest biomass assessment. Carbon Management, 8(4), 305–317. https://doi.org/10.1080/17583004.2017.1357402

Padalia, H. and Yadav, S. (2017). Evaluation of RISAT-1 SAR data for tropical forestry applications. Advances in Space Research, 59(1), pp.2-11.

Padalia, H., Prakash, A., & Watham, T. (2023). Modelling aboveground biomass of a multistage managed forest through synergistic use of Landsat-OLI, ALOS-2 L-band SAR and GEDI metrics. Ecological Informatics, 77, 102234. https://doi.org/10.1016/j.ecoinf.2023.102234

Pan, Y., Birdsey, R. A., Fang, J., Houghton, R., Kauppi, P. E., Kurz, W. A., et al. (2011). A large and persistent carbon sink in the world's forests. Science, 333(6045), 988–993. https://doi.org/10.1126/science.1201609

Patenaude, G.; Milne, R.; Dawson, T.P. (2005). Synthesis of remote sensing approaches for forest carbon estimation: reporting to the Kyoto Protocol. Environ. Sci. Policy 8, 161–178.

Rajashekar, G.; Fararoda, R.; Reddy, R.S.; Jha, C.S.; Ganeshaiah, K.N.; Singh, J.S.; Dadhwal, V.K. (2018). Spatial distribution of forest biomass carbon (Above and below ground) in Indian forests. Ecol. Indic. 85, doi:10.1016/j.ecolind.2017.11.024.

Saatchi, S.S.; Harris, N.L.; Brown, S.; Lefsky, M.; Mitchard, E.T. a; Salas, W.; Zutta, B.R.; Buermann, W.; Lewis, S.L.; Hagen, S.; et al. (2011). Benchmark map of forest carbon stocks in tropical regions across three continents. Proc. Natl. Acad. Sci. U. S. A. 108, 9899–904, doi:10.1073/pnas.1019576108.

Shugart, H.H.; Saatchi, S.; Hall, F.G. (2010). Importance of structure and its measurement in quantifying function of forest ecosystems. J. Geophys. Res. Biogeosciences 115.

Sinha, S., Mohan, S., Das, A. K., Sharma, L. K., Jeganathan, C., Santra, A., Mitra, S. S., & Nathawat, M. S. (2020). Multi-sensor approach integrating optical and multi-frequency synthetic aperture radar for carbon stock estimation over a tropical deciduous forest in India. *Carbon Management, 11*(1), 39–55. https://doi.org/10.1080/17583004.2019.1686931.

Suresh, M.; Chand, T.R.K.; Fararoda, R.; Jha, C.S.; Dadhwal, V.K. (2014). Forest above ground biomass estimation and forest/non-forest classification for Odisha, India, using L-band Synthetic Aperture Radar (SAR) data. In Proceedings of the International Archives of the Photogrammetry, Remote Sensing and Spatial Information Sciences - ISPRS Archives; Vol. 40.

Tian, L., Wu, X., Tao, Y., Li, M., Qian, C., Liao, L., & Fu, W. (2023). Review of remote sensing-based methods for forest aboveground biomass estimation: Progress, challenges, and prospects. Forests, 14(6), 1086. https://doi.org/10.3390/f14061086

Thumaty, K.C.; Fararoda, R.; Middinti, S.; Gopalakrishnan, R.; Jha, C.S.; Dadhwal, V.K. (2016). Estimation of above ground biomass for central Indian deciduous forests using ALOS PALSAR L-band data. J. Indian Soc. Remote Sens. 44, doi:10.1007/s12524-015-0462-4.

Xiao, J., Chevallier, F., Gomez, C., Guanter, L., Hicke, J. A., Huete, A. R., et al. (2019). Remote sensing of the terrestrial carbon cycle: A review of advances over 50 years. Remote Sensing of Environment, 233, 111383. https://doi.org/10.1016/j.rse.2019.111383

Zhang, J.; Huang, S.; Hogg, E.H.; Lieffers, V.; Qin, Y.; He, F. (2014).Estimating spatial variation in Alberta forest biomass from a combination of forest inventory and remote sensing data. Biogeosciences, 11, 2793–2808, doi:10.5194/bg-11-2793-2014.

Zhang, L., Shao, Z. and Diao, C. (2015). Synergistic retrieval model of forest biomass using the integration of optical and microwave remote sensing. Journal of Applied Remote Sensing, 9(1), pp.096069-096069.

Acknowledgements

Field Data used in this study are collected as part of the National Carbon Project (NCP) funded by Indian Space Research Organization, Government of India under its ISRO-Geosphere Biosphere Program. We acknowledge the contribution of the PI's for conducting the field inventories under this project. Authors thank Director, NRSC for encouragement and support. The authors wish to thank NRSC, ISRO team for providing EOS-04 data, JAXA for ALOS-2 PALSAR-2 global mosaic data, and ESA for Sentinel-1 data.

Indian Cartographer, Vol. 44, No. 1 & 2, pp. 12-25
ISSN: 0972-8392 © INCA, 2024

Spatially Distributed CN Technique and Earth Observation Data Sets for Grid-Wise Runoff Assessment in Sarasvati River Catchment, India

Sagar Subhashrao Salunkhe*, Gaurav Kumar and **Apurba Kumar Bera**
Regional Remote Sensing Centre-West (ISRO), Jodhpur (India)
**Corresponding Author's email: sagar.swce@gmail.com*

Abstract

Spatio-temporal estimation of volume and quality of the water resources in semi-arid environments is the need of the moment. The most extensively used methodology for fast and precise estimation of surface runoff from an un-gauged catchment is the Curve Number (CN) technique. Coupling the CN method along with the geospatial technique is an efficient way of runoff estimation. Hence, the current study emphasizes on a grid-wise estimation of the daily runoff for un-gauged Sarasvati River catchment using the CN technique modified for Indian conditions utilising variables generated by remote sensing and other supplementary data. Satellite data, Cartosat DEM, land use/land cover (LULC), soil texture, gridded rainfall and other supplementary data were used for estimation of the daily surface runoff for 15 years (2002-2016). A program was developed in Interactive Data Language (IDL) for estimating runoff as a multiband raster. The mean yearly rainfall and runoff of the catchment were estimated at 732.07 mm and 176.25 mm respectively for the period 2002-2016 with a runoff coefficient of 0.24. The analysis supports Haryana Sarasvati Heritage Development Board (HSHDB) in the planning and development of the Sarasvati rejuvenation project. The precise delineation of the drainage network, catchment and watershed boundary in relatively flat terrain, use of large-scale geospatial inputs, fully distributed CN approach and development of the IDL program are the main research contributions of this study. The work carried out is only research presently available for the Sarasvati river catchment that provides spatial and temporal runoff potential. The current study emphasizes the application of digital cartography and geospatial technologies to sustainable ecosystems and water resource management in the Sarasvati river catchment.

Keywords: CN; runoff; hydrological soil group; Sarasvati river catchment; HSHDB.

Introduction

The most vital natural resource for existence is water. Due to extended dry seasons, worldwide environmental changes, and population development, water resources are under severe strain. Judicious usage of water resources needs spatio-temporal estimation of the volume and quality of the water (Shrestha & Jayaraj, 2018). Negligence and a lack of understanding of current water resources, as well as varying climatic circumstances, have resulted in inequality in water demand and supply. The issue is particularly acute in semi-arid zones, in which water resources are very scarce. The water cycle is incomplete without a surface runoff. It is a vital parameter for determining a watershed's water production potential, planning conservation measures, and lowering soil erosion and inundating risks downstream. In the subject of water resources engineering, the rainfall-runoff event

is widely acknowledged as amongst the most complicated and irregular real-world events. The necessity to assess water resource availability in the ungauged watershed/ catchment is a common subject of discussion. The use of physically-based hydrological models to assess the influence of climatic changes, LULC changes, and water usage on water resources, has been a focus of water resources development operations. In spite of the fact that several hydrological models for estimating runoff from event rainfall are available, the majority of them require vast input data, extensive calibration, and have location-specific applicability (Garg et al., 2013). In runoff modelling, the spatio-temporal variation of hydrological factors responsible for runoff estimation is crucial. The evaluation of land surface attributes at spatio-temporal scales using geospatial technology, and advanced computer skills are exceptionally valuable input information for hydrological modeling. Remote sensing technology is an excellent fit to optimize the usage of existing spatial data.

The Natural Resources Conservation Service Curve Number (NRCS-CN) method developed by the United States Department of Agriculture (USDA) is widely applied for the generation of surface runoff because of its flexibility and simplicity (Nagarajan & Poongothai, 2012). It is also called simply the CN approach. It is the most versatile and commonly adopted technique for estimating runoff quickly. It is also reasonably simple to use with little data and produces appropriate results. This technique integrates the watershed characteristics and climatic conditions into one parameter named as CN. The NRCS-CN method for generating surface runoff is widely acknowledged by experts, foresters, hydrologists, water resource developers, and engineers (Pandey & Stuti, 2017). Many researchers applied the CN approach for the generation of surface runoff from ungauged watersheds in India (Rao et al., 2010; Nagarajan & Poongothai, 2012; Pandey & Stuti, 2017; Rawat & Singh, 2017; Satheeshkumar et al., 2017; Shrestha & Jayaraj, 2018).

All the above investigations carried out for estimation of runoff at the watershed's outlet using the NRCS-CN technique used lumped or semi-distributed parameter approach. In this approach, they have calculated composite CN or weighted-CN for the entire catchment or watershed. In its initial phases of development, this averaging method was more popular due to the ease of manual computations. Given the existence of high-speed computers, the classic composite technique is still used to estimate runoff. However, Jena et al. (2012) found considerable deviations in runoff calculations utilizing single composite CN values rather than utilizing the distributed-CN approach. This could be owing to the NRCS-CN formula's nonlinear nature. Lantz & Hawkins (2002) have also noted the potential errors when a single composite CN is used. Mishra & Singh (2003) have also shown that when there is a large variation of CN in a watershed, runoff calculated using a lumped or semi-distributed technique will deviate significantly. The widespread accessibility of spatial data and usage of GIS favor the practice of a spatially distributed CN approach to runoff assessment currently. Also, a fully distributed modeling approach is more rational and it has certain advantages. First, it enables to divide any significant catchment into several grids and accordingly runoff can be generated over each grid. Runoff can be routed from each grid to the outlet of the whole basin for calibration and validation. However, there are just a few physically-based fully distributed hydrological models available which are suited for both study and real-world applications. In addition, these modelling methods need a large amount of input data, are complex, and require observed runoff data for calibration and validation. As the present study area is an ungauged catchment, the NRCS-CN method with the fully distributed approach is adopted for the estimation of the surface runoff.

HSHDB is working on the Rejuvenation of Sarasvati river. HSHDB has planned a dam at Adi Badri and a barrage near Rampur Gainda village on the Somb river (the Yamuna river's tributary) in the Yamunanagar district of Haryana to supplement the water in the Sarasvati river (Figure 1). Water from the dam and barrage will be diverted to the Sarasvati creek (originating point of present Sarasvati river near Rampur Harian village). Adi Badri is a forest region and archaeological place located in the Bhabar area of the Yamunanagar district, in the foothills of the Shivalik Hills. The Sarasvati river begins close to Rampur Harian village situated at 9 km southward direction of Adi Badri and flows southwest from there. The River Somb begins from the more northern direction in the upper portion of the Siwalik Hills. It flows east of the Sarasvati river in a north-south direction before joining the Yamuna river in the southeast. The Somb River passing through this area is considered as the originating point of the Vedic river Sarasvati (the point where the river leaves the mountains and enters plain land) (Bhadra et al., 2009). The Vedic Sarasvati was a massive and blessed river in northwest India that flowed

from the Har-ki-Doon glacier in the Garhwal Himalayas to the Gulf of Cambay on the Gujarat coast and vanished approximately 3000 B.C (Bhadra et al., 2009). Several fragments of this river exist as palaeo channels (Gupta, 1996; Valdiya, 2002).

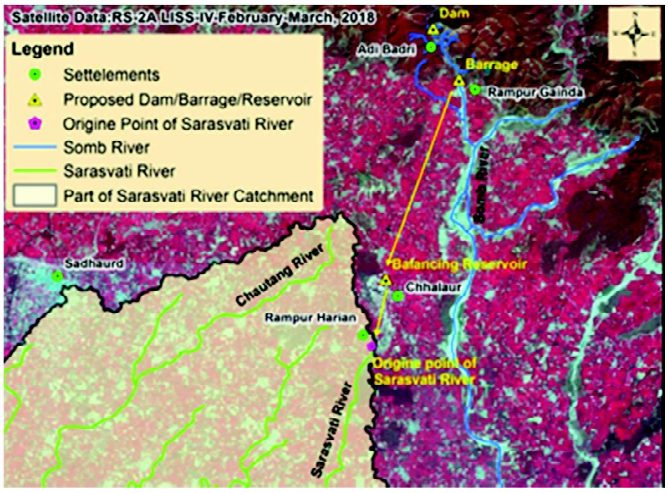

Fig. 1: Location of the proposed dam, barrage and balancing reservoir

HSHDB needs to assess the current water yield potential of the Sarasvati river catchment as it will support in planning and development of the Sarasvati Rejuvenation project. Therefore, HSHDB requested and funded for taking up the current study. Therefore, the current study focuses on grid-wise estimation of the daily runoff for ungauged Sarasvati river catchment using the NRCS-CN method modified for Indian conditions utilising variables generated by remote sensing and other supplementary data.

Study Area

The current study is carried out in the Sarasvati river catchment (delineated by considering the outlet point as the confluence with River Ghaggar) mostly in Haryana and some parts of Punjab (Fig. 2). It lies partly in Ambala, Kaithal, Karnal, Kurukshetra and Yamunanagar districts of Haryana and Patiala district of Punjab. The Sarasvati river started its course close to Rampur Harian village, in the southward direction of Adi Badri, and flowed over the places like Bilaspur, Mustafabad, Thanesar, Bibipur, and Pehowa in Haryana before joining the Ghaggar river close to Rasauli village in Punjab. Sarasvati river is currently in an obsolete state, largely seasonal and with intermittent discharge. The study area is estimated at 2140 km^2 and is bounded by latitude 29º 52/ 0.37// N to 30º 24/ 23.16// N and longitude 76º 10/ 10.27//E to 77º20/39.27// E.

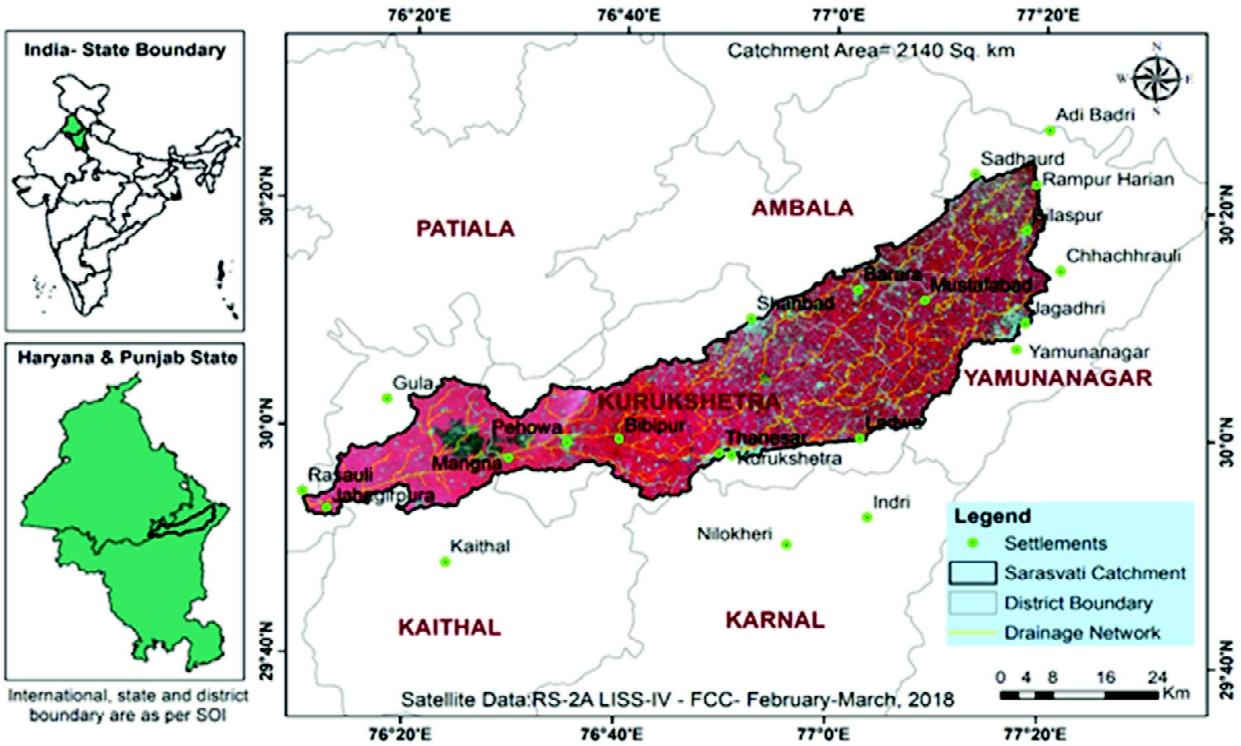

Fig. 2: Study area location: Sarasvati river catchment

Database Used

Different input data used in the study are presented in Table 1. The elevation in the study area varies from 182m to 296 m. Agricultural land covers 90.33% of the study area (Fig. 3). The remaining part is covered by built-up land (5.91%), forest land (2.47%), and a very small area by other categories (water bodies, wastelands, grass/ grazing land and wetlands). In the case of soil, 62.65% of the total geographical area is represented by clay loam soils (Fig. 4). The remaining part is covered by sandy loam (18.68%), loam (6.72%), silt loam (5.14%) soils, and a very small area by loamy sand, sandy clay loam, silty clay loam and silty clay soils. Non-soil categories like built-up land and water bodies occupy a 5.68% and 0.65% area respectively. The study area's average annual precipitation for the period 2002-2016 varies from 490 to 1444 mm (Fig. 5).

Table 1: Input data used in the study

Data	Description	Source	Reference
Satellite data	IRS Resorcesat-2 LISS-IV- February and March 2018	NRSC, ISRO, Hyderabad	--
DEM	Cartosat 30 m	NRSC, ISRO, Hyderabad	NRSC, 2014
LULC	1:50000 scale (2015-16)	NRSC, ISRO, Hyderabad	NRSC, 2011
Soil texture	1:50000 scale	SAC, ISRO, Ahmadabad	Dasgupta et al., 2000
Rainfall	0.25°×0.25° daily gridded (2002-2016)	IMD, Pune	Pai et al., 2014
Crop production	Season-wise data for different districts	Government of India	--
SOI toposheets	1:50000 scale	SOI	--
Existing maps	Sarasvati River	HSHDB, Panchkula	--

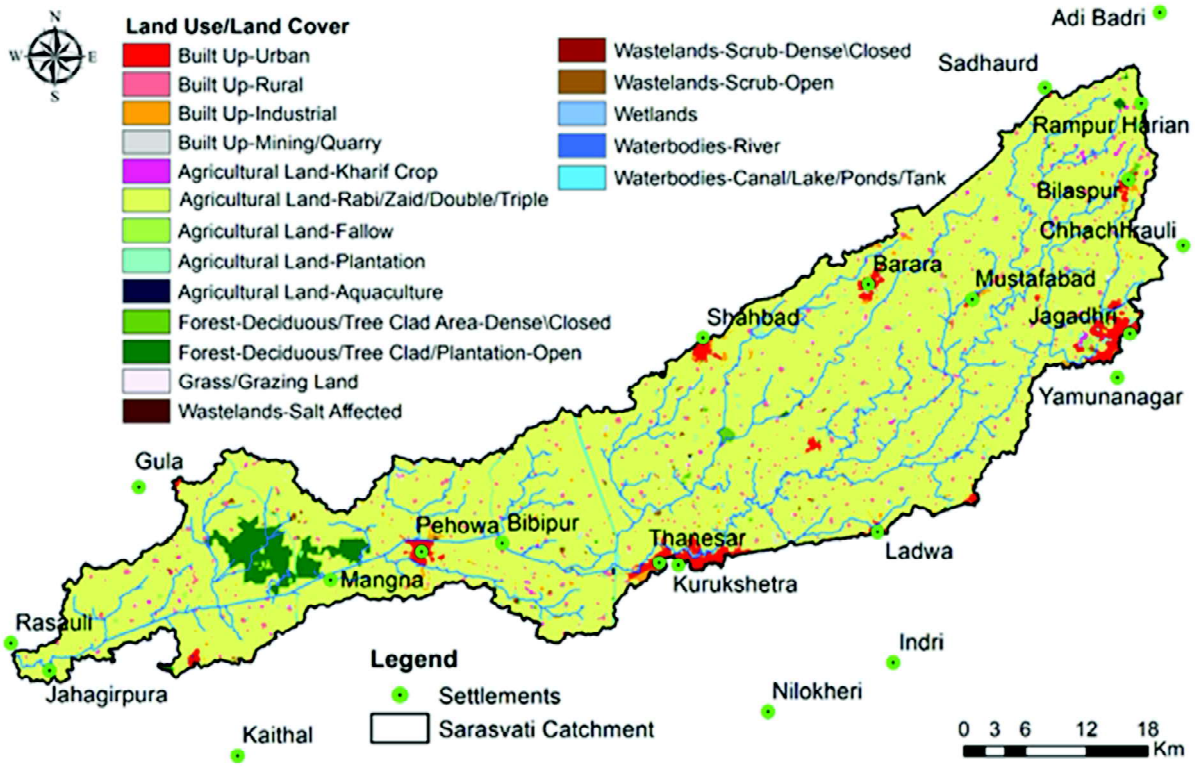

Fig. 3: LULC (1:50000 scale) of Sarasvati river catchment

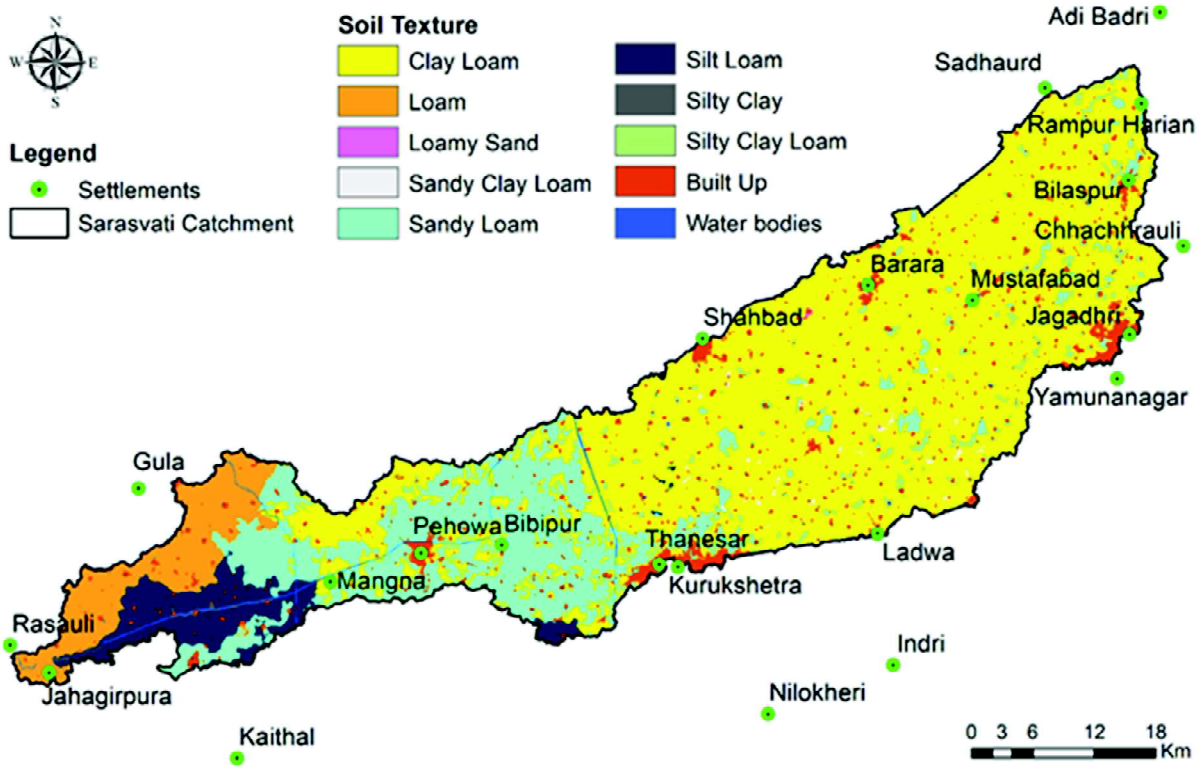

Fig. 4: Soil texture (1:50000 scale) of Sarasvati river catchment

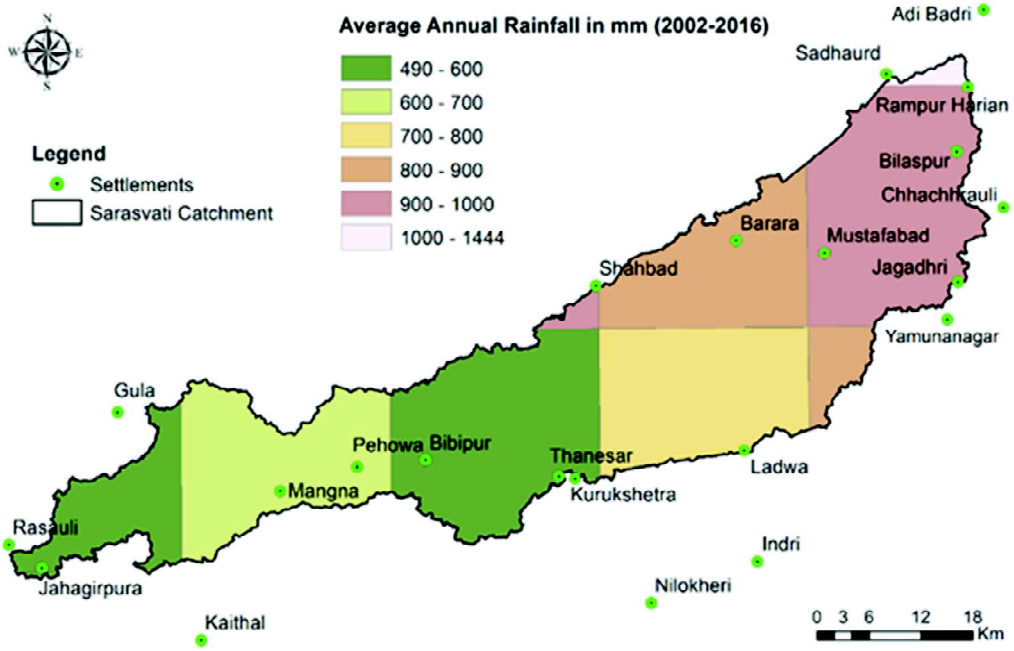

Fig. 5: Average annual rainfall (2002-2016) of Sarasvati river catchment

Methodology

Methodology flow chart for the study is presented in Fig. 6. Flow direction, flow accumulation and the slope have been prepared using DEM. As the study area is relatively flat terrain, the watershed delineator module in the Soil and Water Assessment Tool (SWAT) (Neitsch et al., 2011) were used for the delineation of catchment and watershed boundary. The drainage network was delineated by visual interpretation of satellite data and taking reference from

the SOI toposheet. The Sarasvati river catchment and watershed boundaries were then delineated by burning the drainage network over the DEM. A hybrid drainage network (satellite-derived drainage + potential drainage) has also been prepared for the study area. Hydrological Soil Group (HSG) was assigned based on Soil texture data. Grid-wise runoff CN (30m×30m) was prepared by integrating LULC and HSG for Antecedent Moisture Condition-II (AMC-II). Slope-adjusted CN for AMC-II was prepared using slope and CN for AMC-II. Later, slope-adjusted CN for AMC-II was converted to courser grid size (990m×990m) by averaging the CN values within each grid. The grid size 990m×990m was chosen for final output as it is computationally efficient and also available rainfall data is at much courser resolution (0.25°×0.25° - approx. 27 km). Slope-adjusted CN corresponding to AMC-I and AMC-II were prepared using slope-adjusted CN corresponding to AMC-II. AMC for each day (0.25°×0.25°) for 15 years (2002-2016) has been identified using previous 5-day antecedent rainfall. Potential maximum retention (S) has been estimated for each day (990m×990m) for 15 years (2002-2016) using CN of identified AMC condition. Finally, daily runoff depths for a grid size of 990m×990m approximately 1Km×1Km for 15 years (2002-2016) were estimated using the CN method and rainfall data. A program was developed in IDL for grid-wise daily runoff estimation using the NRCS-CN method. Daily runoff was obtained in the form of a multiband raster. The detailed methodology is described as follows:

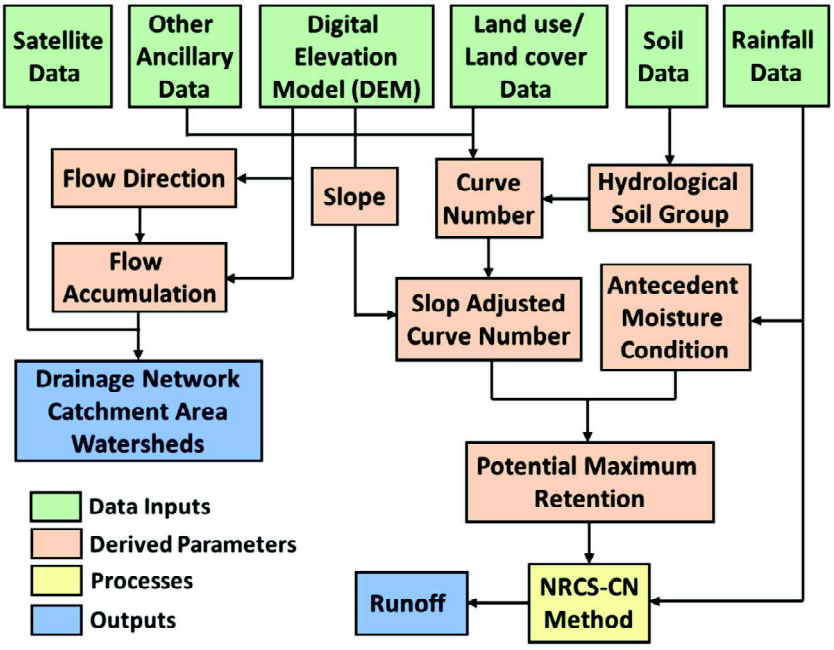

Fig. 6: Methodology flowchart

NRCS-CN Method

USDA NRCS established a technique to estimate the amount of direct runoff from rainfall in 1954 (Rallison, 1980). It is called the CN approach, and it was established empirically for small agricultural watersheds (USDA, 1972). In the present study, runoff is estimated using the NRCS CN technique as follows:

$$Q = \frac{(P - 0.3S)^2}{(P + 0.7S)} \quad (1)$$

Where Q = Runoff depth (mm); P= Rainfall depth (mm) and S = Potential maximum retention (mm). Narayana (1993) modified the original NRCS CN approach by conducting multiple experiments in India to develop equation (1) for Indian conditions. In India, equation (1) was also used by Rao et al. (2010) and Satheesh kumar et al. (2017) to estimate the runoff. If $P > 0.3S$, equation (1) holds; else, Q = 0. The S value in equation (1) is estimated as follows:

$$S = \left(\frac{25400}{CN}\right) - 254 \quad (2)$$

Where CN is known as the curve number, which varies from 0 (lowest runoff) to 100 (highest runoff).

Determination of AMC

AMC is an indication of watershed moistness which represents the quantity of water in the soil profile at any particular time. Based on soil properties and rainfall limits for rainy and non-rainy seasons, NRCS defined three antecedent soil-moisture conditions and named them I, II, and III. CN also varies with one of the three AMCs. The AMC is assigned based on the cumulative rainfall during the previous five days. Daily gridded AMC for 15 years (2002-2016) were determined using daily gridded rainfall data as given in Table 2 (Chow, 1988). The rainy season in the study area is considered from June to October.

Table 2: Classification of AMC

AMC	Soil characteristics	5-day antecedent precipitation (mm)	
		For non- rainy-season	For rainy-season
I	Dry	< 12.5	< 35
II	Normal or average	12.5 – 27.5	35 – 52.5
III	Wet	>27.5	>52.5

Preparation of Runoff CN

Grid-wise CN (30m×30m) was prepared by overlaying LULC and HSG for AMC-II (CN2) in a GIS environment. CN was designated to each combination of LULC and HSG based on works of literature (USDA, 1986; Tripathi, 1999; Rao et al., 2010; Sunder Kumar et al., 2010; Pancholi et al., 2015; Tailor & Shrimali 2016; Patel et al., 2017; Satheeshkumar et al., 2017; Kuanar & Nath, 2018 etc.). Season-wise crop production data for different districts were used to identify the dominant crops grown in Kharif and Rabi seasons. Rice and wheat were found to be the dominant crops in the Kharif and Rabi seasons, respectively, while sugarcane was the dominant annual crop. CN values for agricultural land were given based on identified crops.

HSG (Hydrologic Soil Group) Preparation

The rate of soil infiltration depends upon surface conditions and subsurface permeability. Based on the lowest infiltration rate measured for bare soil after extended wetness, soils are classified into four HSGs (A, B, C, and D). HSGs also show the transmission rate, or how quickly water travels through the soil. HSG was assigned based on soil texture data as given by USDA (1986). HSG-D was assigned to non-soil categories like water bodies and built-up areas (Rama Subramoniam et al., 2014).

Estimation of Slope Adjusted Runoff CN

In determining the flow of water, the land slope parameter is crucial. Previous research has demonstrated that when the slope increases, the surface runoff increases due to a reduction in initial abstraction, infiltration, and the recession time of overland flow (Chaplot & Bissonnais, 2003). The traditional NRCS-CN method is developed for field-scale with the assumption that the field will have a constant slope of around 5%. However, to account for the slope's spatial variance, the specified CN_2 values must be slope corrected. As a result, Sharpley & Williams (1990) provided the following equation for the calculation of slope adjusted CN_2 called $CN_{2\alpha}$:

$$CN_{2\propto} = \frac{1}{3}(CN_3 - CN_2)(1 - 2e^{-13.86\propto}) + CN_2 \quad (3)$$

Where α = Slope in (m/m). As, this procedure has not been thoroughly tested for ground conditions, Huang et al. (2006) took a more straightforward method and provided the following equation for $CN_{2\alpha}$:

$$CN_{2\propto} = CN_2\left[\frac{322.79 + (15.63 \times \propto)}{\propto + 323.52}\right] \quad (4)$$

In the present study, equation (4) is used for the calculation of slope-adjusted CN_2. Slope adjusted CN_1 and CN_3 are calculated as per Sobhani (1975) and Hawkins et al. (1985) respectively as follows:

$$CN_{1\propto} = \frac{CN_{2\propto}}{2.334 - (0.01334 \times CN_{2\propto})} \quad (5)$$

$$CN_{3\propto} = \frac{CN_{2\propto}}{0.427 + (0.00573 \times CN_{2\propto})} \quad (6)$$

Results and Discussions

Drainage Network and Watersheds

A drainage network and watersheds of the Sarasvati river catchment are given in Fig. 7. Chautang, Rakhsi, Bentan and Para are tributaries of Sarasvati river. The watershed

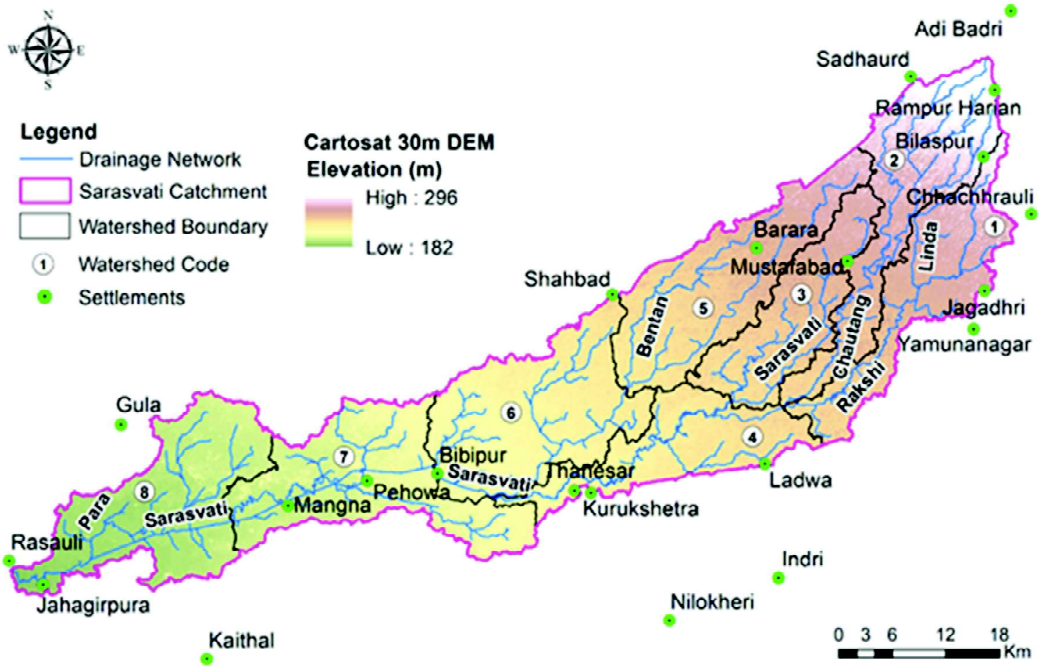

Fig. 7: Drainage network and watersheds of Sarasvati river catchment

boundary is essential for determining which areas contribute to runoff, silt, and pollution. The Sarasvati river catchment has been divided into eight watersheds, each covering 195km^2 to 331 km^2.

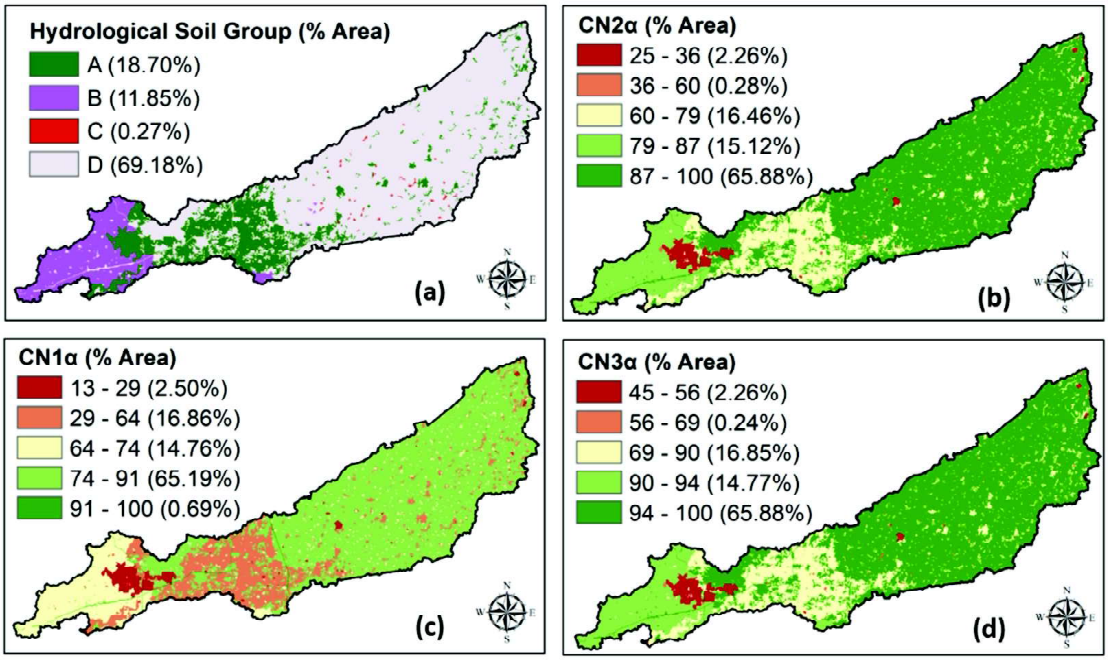

Fig. 8: (a) HSG of Sarasvati river catchment; **(b)** CN2α of Sarasvati river catchment; **(c)** CN1α of Sarasvati river catchment; **(d)** CN3α of Sarasvati river catchment

HSG and Slope Adjusted CN

HSG and slope adjusted CN of Sarasvati river catchment is given in Fig. 8. It has been observed that soils containing HSG-D cover the majority of the overall geographical area (69.18 %). This is because of the clay loam soil texture in these areas. The rest of the area was covered by HSG-A (18.70%), HSG-B (11.85%) and HSG-C

(0.27%). The slope of the catchment was ranging from 0-59%. It was observed that $CN_{2\alpha}$ was ranging from 25 to 100. 87-100 (65.88%) range of $CN_{2\alpha}$ covers the majority of the whole geographical area mostly in the catchment's upper parts followed by 60-79 (16.46%), 79-87 (15.12%), 25-36 (2.26%) and 36-60 (0.28%) in other parts. Similarly, $CN_{1\alpha}$ was ranging from 13 to 100. Also, 74-91 (65.19%) range of $CN_{1\alpha}$ covers the majority of the whole geographical area mostly in the catchment's upper parts followed by 29-64 (16.86%), 64-74 (14.76%), 13-29

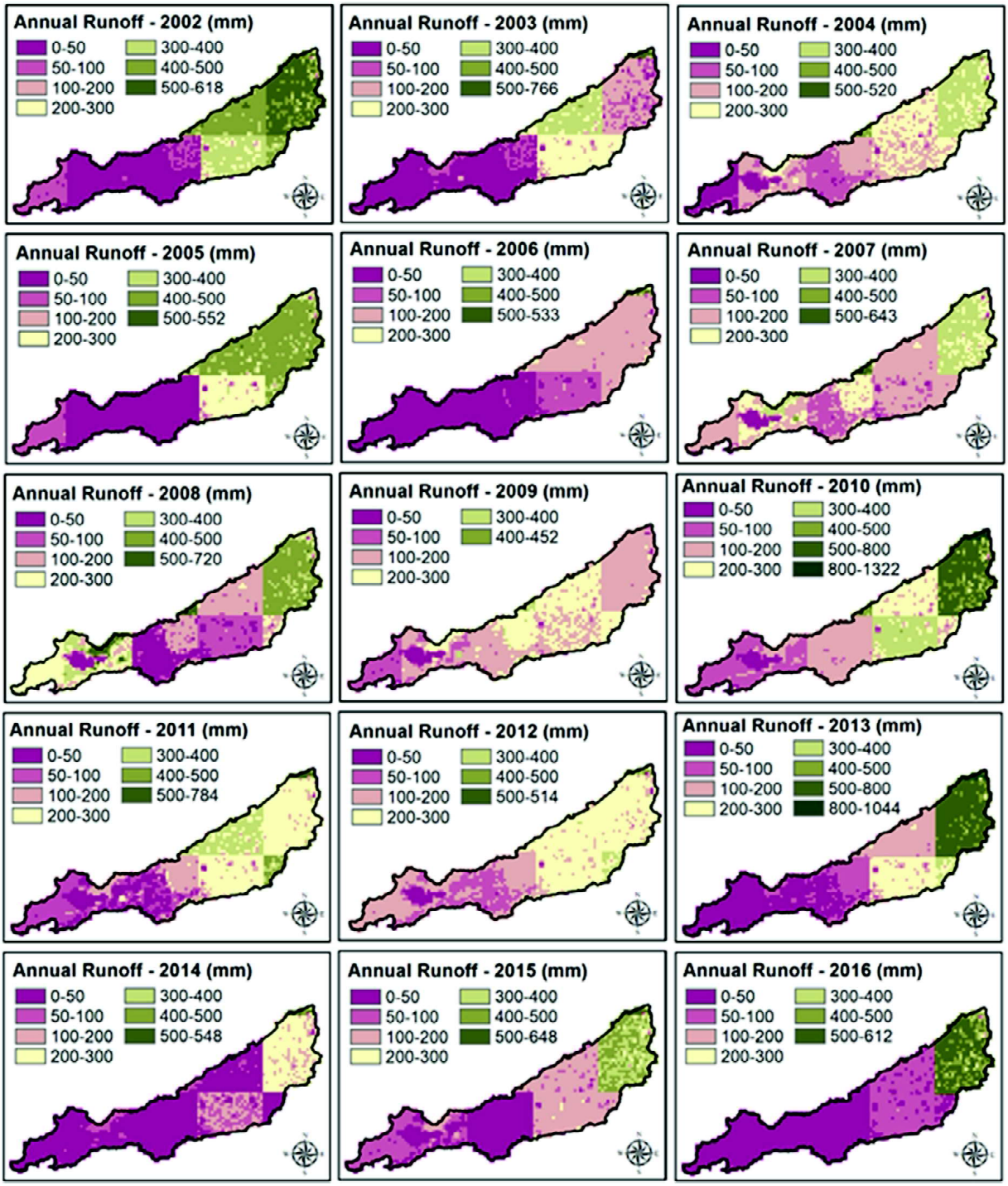

Fig. 9: Annual runoff from 2002 to 2016 in Sarasvati river catchment

(2.50%) and 91-100 (0.69%) in other parts. Similarly, $CN_{3\alpha}$ was ranging from 45 to 100. Also, 94-100 (65.88%) range of $CN_{3\alpha}$ covers the majority of the whole geographical area mostly in the catchment's upper parts followed by 69-90 (16.85%), 90-94 (14.77%), 45-56 (2.26%) and 56-69 (0.24%) in other parts.

Spatial Variability of Runoff

Monthly and annual runoff depths were estimated by aggregating daily runoff depths. The spatial variability of annual runoff in the catchment for the period 2002-2016 is presented in Fig. 9. The year 2010 recorded maximum runoff varying from 0mm to 1322mm, and the year 2009 recorded minimum runoff varying from 0mm to 452mm. The spatial variability of average annual runoff (2002-2016) in the catchment is presented in Fig. 10. The catchment's runoff varied from 0 to 603 mm. Higher runoff (above 300 mm) was observed in the upper part while lower runoff (below 100 mm) was observed in the lower part of the catchment. This is because of higher rainfall in the upper part and lower rainfall in the lower part of the catchment. The upper part of the catchment was having hydrological soil group "D" and higher values of the CN for all the three antecedent moisture conditions (AMC). This was another reason for having a higher runoff in the upper part of the catchment.

Area Weighted Rainfall and Runoff of The Catchment

Grid-wise rainfall and runoff were averaged for the total catchment by adopting the area-weighted average method. Annual rainfall and runoff of the catchment for the years 2002-2016 are presented in Figure 11. It was observed that the years 2006 and 2014 were recorded as minimum annual rainfall and runoff as 483.16 mm (and 84.92 mm runoff) and 509.84 mm (and 83.29 mm runoff) respectively. Maximum annual rainfall was recorded in the years 2008 (1040.92 mm) and 2007 (925.27 mm). Maximum annual runoff was recorded in the years 2002 (249.82 mm) and 2005 (219.57 mm). The mean yearly rainfall and runoff of the catchment were estimated at 732.07 mm and 176.25 mm respectively for the period 2002-2016 with a runoff coefficient of 0.24. The yearly rainfall trend line is concave, indicating that rainfall increased from 2002 to 2008, then declined till 2016 due to the recent abnormal climatic changes. The annual runoff trend line is also concave and follows a pattern that is similar to that of yearly rainfall. Therefore, from the trend line, it can be observed that rainfall and runoff have decreased in recent years.

Validation of Outputs

To validate the NRCS-CN model outputs, observed runoff data is required. Central Water Commission (CWC), New Delhi has its hydro observation sites which measure the river discharge at various locations in India (www.indiawris.gov.in). But there is no hydro observation site available in the study area or nearby study area. Therefore, to validate the NRCS-CN model outputs, monthly rainfall data for 15 years (2002-2016) was used. By comparing anticipated monthly runoff with monthly rainfall peaks, the applicability and validity of the NRCS-CN model were evaluated. A similar approach was also adopted by Rawat & Singh (2017). The series of monthly rainfall and runoff (2002-2016) in the catchment is presented in Fig. 12. Even though the model may have certain uncertainty owing to the absence of actual runoff, the anticipated runoff and rainfall peaks matched quite well. Results were further validated by correlation analysis of monthly rainfall and runoff (Fig. 13). A similar approach was also adopted by Rawat & Singh (2017) and Satheesh kumar et al. (2017). It can be observed that, at a 99% confidence interval ($p<0.01$), there is a significant positive correlation between monthly rainfall and runoff, with a higher correlation coefficient ($r=0.93$). A relationship between monthly rainfall and runoff was also developed by fitting a linear regression by considering runoff as the dependent variable and rainfall as an independent variable. It was observed that there exists a good linear association between monthly rainfall and runoff having a high coefficient of determination ($R^2=0.87$).

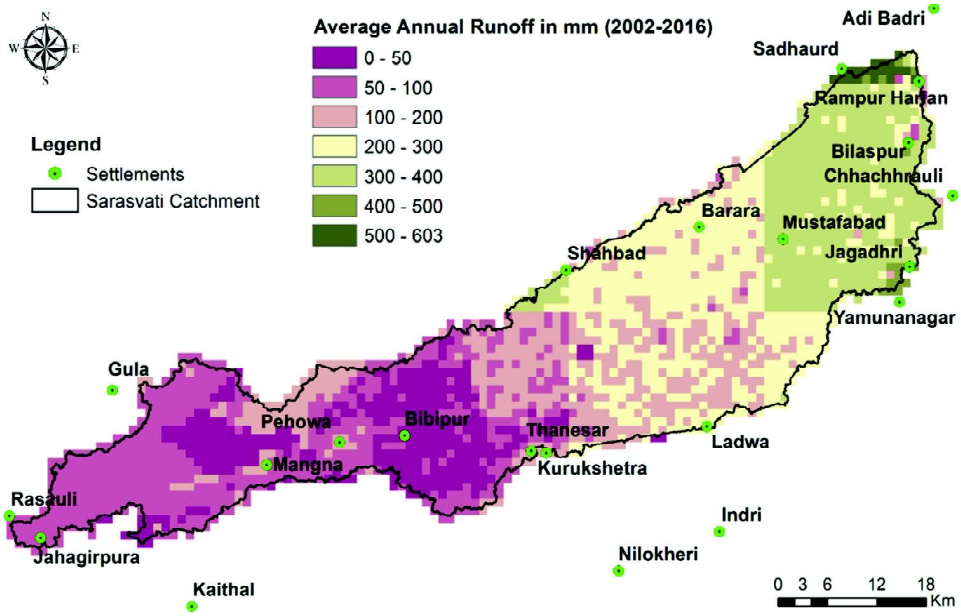

Fig. 10: Average annual runoff (2002-2016) of Sarasvati river catchment

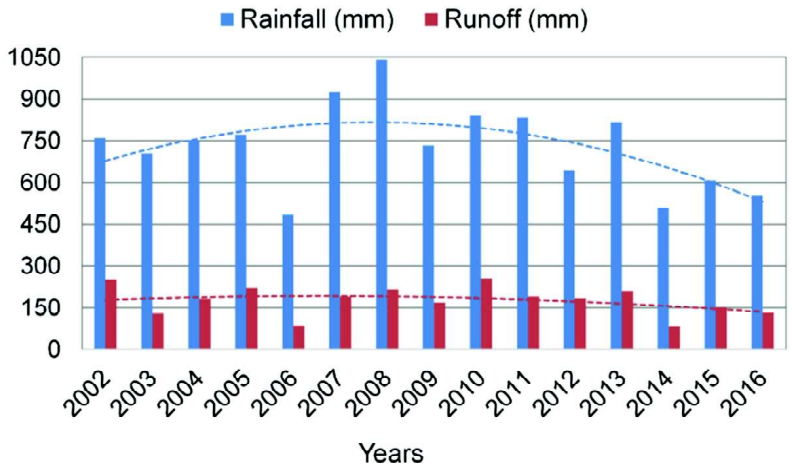

Fig. 11: Annual rainfall and runoff time series of the catchment from 2002-2016

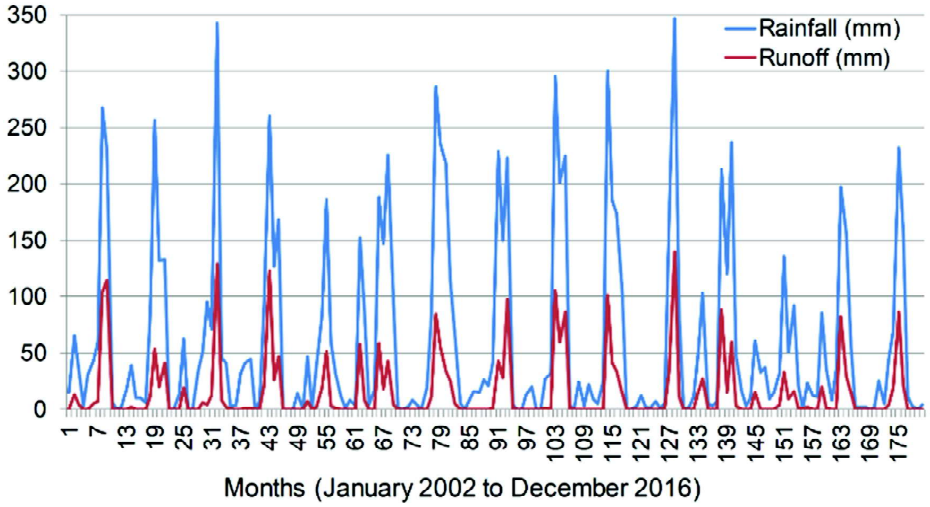

Fig. 12: The series of monthly rainfall and runoff (2002-2016) in the catchment

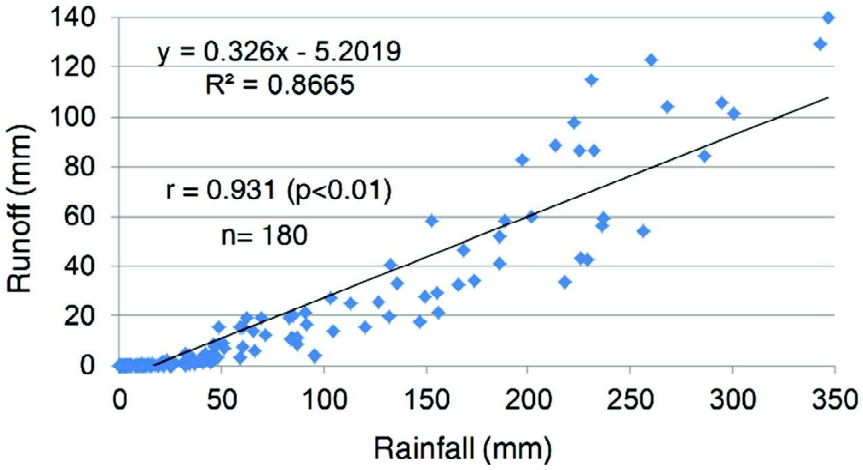

Fig. 13: Association between monthly rainfall and runoff in the catchment

Conclusion

This study demonstrates grid-wise estimation of the runoff for un-gauged Sarasvati river catchment using the NRCS-CN technique modified for Indian conditions utilising variables generated by remote sensing and other supplementary data. The CN which is the most important model parameter has been specified scientifically using available works of literature and season-wise crop production data for different districts. Comparison/ validation of estimated runoff with observed runoff was not attainable in the ungauged Sarasvati river catchment. However, a large-scale geospatial database (1:50000 scale) and other supplementary data made it possible to scientifically estimate grid-wise daily runoff in the catchment. The NRCS-CN technique was shown to be more efficient for estimating runoff since it takes less time and can handle a larger data set. For tiny catchments or watersheds, traditional hydrological data are generally unavailable for taking developmental activities. In such circumstances, remote sensing-derived variables, as well as other supplementary data, might be used to improve runoff estimation approaches. The analysis gives a reasonable estimate of the catchment's current runoff potential and it will support HSHDB in the planning and development of the Sarasvati rejuvenation project. Precise delineation of the drainage network, catchment and watershed boundary in relatively flat terrain, use of large-scale geospatial inputs, fully distributed CN approach and development of the IDL program are the main research contributions of this study. The work carried out is only research presently available for the Sarasvati River catchment that provides spatial and temporal runoff potential. The outcomes of this study could, however, be enhanced in the future by including some ground-based data and analysis. HSHDB is planning to establish gauge discharge sites at some of the locations in the catchment. Therefore, the grid-wise routing of runoff to the catchment outlet and comparison of the outputs with observed runoff data, if available, will be the study's future focus.

References

Bhadra, B.K., Gupta, A.K., & Sharma, J.R. (2009). Sarasvati Nadi in Haryana and its linkage with the Vedic Sarasvati River – integrated study based on satellite images and ground based information. Journal of the Geological Society of India, 73(2), 273-288.

Chaplot, V.A.M., & Bissonnais, Y.L. (2003). Runoff features for interrill erosion at different rainfall intensities, slope lengths, and gradients in an agricultural loessial hill slope. Soil Science Society of America Journal, 67, 844-851.

Chow, V.T., Maidment, D.R., & Mays, L.W. (1988). Applied hydrology. McGraw-Hill, New York.

Dasgupta, A.R., Mukund, R., & Gopalan, A.K.S. (2000). The national (natural) resources information system. International Archives of Photogrammetry and Remote Sensing, XXXIII (Part B2), 131-138.

Garg, V., Nikam, B.R., Thakur, P.K., & Aggarwal, S.P. (2013). Assessment of the effect of slope on runoff potential of a watershed using NRCS-CN method. International Journal of Hydrology Science and Technology, 3(2), 141-159.

Gupta, S.P. (1996). Indus-Sarasvati civilization: origins, problems and issues. Pratibha Prakashan, Delhi.

Hawkins, R.H., Hjelmfelt Jr, A.T., & Zevenbergen, A.W. (1985). Runoff probability, storm depth and curve numbers. Journal of Irrigation and Drainage Engineering, 111(4), 330-340.

Huang, H., Gallichand, J., Wang, Z., & Goulet, M. (2006). A modification to the soil conservation services curve number method for steep slopes in the Loess Plateau of China. Hydrological Processes, 20(3), 579–589.

Jena, S.K., Tiwari, K.N., Pandey, A., & Mishra, S.K. (2012). RS and Geographical Information System–based evaluation of distributed and composite curve number techniques. Journal of Hydrologic Engineering, 17(11), 1278-1286.

Kuanar, M., & Nath, S. (2018). Study of the impact of land use change on estimation of runoff using SCS-CN & GIS for Gangua-Jhumka watershed. International Journal of Emerging Research in Management & Technology, 7(1), 8-21.

Lantz, D.G., & Hawkins, R.H. (2002). Discussion of long-term hydrologic impact of urbanization: a tale of two models. Journal of Water Resources Planning and Management, 128(6), 462-463.

Mishra, S.K., & Singh, V.P. (2003). Soil conservation service curve number (SCS-CN) methodology. Kluwer Academic Publishers, Dordrecht, The Netherlands.

Nagarajan, N., & Poongothai, S. (2012). Spatial mapping of runoff from a watershed using SCS-CN method with remote sensing and GIS. Journal of Hydrologic Engineering, 17(11), 1268-1277.

Narayana, V.V.D. (1993). Soil and water conservation research in India. Indian Council of Agricultural Research, New Delhi.

Neitsch, S.L., Arnold, J.G., Kiniry, J.R., & Williams, J.R. (2011). Soil and Water Assessment Tool-theoretical documentation (version 2009). Texas Water Resources Institute, Technical Report No. 406, Texas A & M University System College Station, Texas, USA.

NRSC. (2011). Land use Land Cover Atlas of India (LULC 50K Atlas). National Remote Sensing Centre (NRSC), Indian Space Research Organisation, Department of Space, Government of India, Hyderabad.

NRSC. (2014). Evaluation of Indian National DEM (Version-2) from Cartosat-1 Data. National Remote Sensing Centre (NRSC), Indian Space Research Organisation, Department of Space, Government of India, Hyderabad.

Pai, D.S., Latha, S., Rajeevan, M., Sreejith, O.P., Satbhai, N.S., & Mukhopadhyay, B. (2014). Development of a new high spatial resolution (0.25° × 0.25°) long period (1901–2010) daily gridded rainfall data set over India and its comparison with existing data sets over the region. Mausam 65(1), 1-18.

Pancholi, V.H., Lodha, P.P., & Prakash, I. (2015). Estimation of runoff and soil erosion for Vishwamitri River watershed, western India using RS and GIS. American Journal of Water Science and Engineering, 1(2), 7-14.

Pandey, A.C., & Stuti. (2017). Geospatial technique for runoff estimation based on SCS-CN method in upper South Koel River basin of Jharkhand (India). International Journal of Hydrology, 1(7), 213-220.

Patel, J., Singh, N.P., Prakash, I., & Mehmood, K. (2017). Surface runoff estimation using SCSCN method- a case study on Bhadar watershed, Gujarat, India. International Journal of Interdisciplinary Research, 3(5), 1213-1218.

Rallison, RE (1980) Origin and evolution of the SCS runoff equation. In: Procedings of Symposium on Watershed Management, 912-924, 21-23 July, American Society of Civil Engineering, Boise, Idaho, New York.

Rama Subramoniam, S, Bhakta, D, Singh, A, Salunkhe, SS, Jeyaseelan, AT, & Sharma, JR (2014) Spatial variability of runoff in Cauvery basin using geo-spatial techniques. In: Procedings of International Symposium on Integrated Water Resources Management (IWRM–2014), 1228-1235, 19–21 February, CWRDM, Kozhikode, Kerala, India.

Rao, K.N., Narendra, K., & Latha, P.S. (2010). An integrated study of geospatial information technologies for surface runoff estimation in an agricultural watershed, Journal of the Indian Society of Remote Sensing, 38(2), 255-267.

Rawat, K.S., & Singh, S.K. (2017). Estimation of surface runoff from semi-arid ungauged agricultural watershed using SCS-CN method and earth observation data sets. Water Conservation Science and Engineering, 1(4), 233-247.

Satheeshkumar, S., Venkateswaran, S., & Kannan, R. (2017). Rainfall–runoff estimation using SCS–CN and GIS approach in the Pappiredipatti watershed of the Vaniyar sub basin, South India. Modeling Earth Systems and Environment, 3(1), 24.

Sharpley, A.N., & Williams, J.R. (1990). EPIC: Erosion/productivity impact calculator 1, Model Documentation, Technical Bulletin 1768. U.S. Department of Agriculture, USA.

Shrestha, P.M., & Jayaraj, G.K. (2018). Application of SCS-CN model in runoff estimation. International Journal for Research in Applied Science & Engineering Technology, 6(3), 2363-2369.

Sobhani, G. (1975). A review of selected small watershed design methods for possible adoption to Iranian conditions. MS Thesis. Utah State University, Logan, UT.

Sunder Kumar, P., Ratna Kanth Babu, M.J., Praveen, T.V., & Vagolu, V.K. (2010). Analysis of the runoff for watershed using SCS-CN method and Geographic Information Systems. International Journal of Engineering Science and Technology, 2(8), 3947-3654.

Tailor, D., & Shrimali, N.J. (2016). Surface runoff estimation by SCS curve number method using GIS for Rupen-Khan watershed, Mehsana district, Gujarat. Journal of Indian Water Resources Society, 6(4), 1-5.

Tripathi, M.P. (1999). Hydrological modeling of small watershed. Ph.D. Thesis. Department of Agriculture and Food Engineering, Indian Institute of Technology, Kharagpur.

USDA. (1972). National Engineering Handbook, Section 4: Hydrology. United States Department of Agriculture (USDA), Soil Conservation Service, Washington, D.C.

USDA. (1986). Urban Hydrology for Small Watersheds, Technical Release 55. United States Department of Agriculture (USDA), Soil Conservation Service, Washington, D.C.

Valdiya, K.S. (2002). Sarasvati-the river that disappeared. University Press (India), Hyderabad.

Acknowledgements

The authors acknowledge the Director, NRSC, ISRO, Hyderabad, and the CGM RCs, NRSC, ISRO, Hyderabad, for their keen interest, encouragement and support in the present study. They are grateful to Dr. S. S. Rao, Deputy Director, BG&WSA, NRSC, Hyderabad for useful suggestions, review and support for project activities. They are thankful to HSHDB, Panchkula, Haryana, for funding the above project. They are also grateful to all the organisations that supplied the various datasets that were used in this study. They further extend their thanks to the technical committee of HSHDB for fruitful discussions and suggestions. Sincere thanks are also due to all the members of the project quality evaluation team for their suggestions and recommendations. All the employees of the RRSC-W, Jodhpur, also deserve appreciation for their help throughout this endeavor.

Author Contributions

All authors of this manuscript have contributed to the study. Conceptualization, database preparation, analysis and original manuscript drafting were performed by Sagar Subhashrao Salunkhe. Development of IDL program for CN algorithm was performed by Gaurav Kumar. Quality evaluation, review, support and manuscript editing was performed by Apurba Kumar Bera. All authors read and approved the final version of the manuscript. All authors commented on previous versions of the manuscript for necessary improvement.

Indian Cartographer, Vol. 44, No. 1 & 2, pp. 26-33
ISSN: 0972-8392 © INCA, 2024

Quantifying the Impact of Higher-Order Branches on QSM-Based Volume Estimation of Trees Using Simulated Terrestrial LiDAR Data

Moonis Ali[1]*, Bharat Lohani[1], Markus Hollaus[2] and Norbert Pfeifer[2]
[1]Department of Civil Engineering, Indian Institute of Technology Kanpur, Kanpur (India)
[2]Department of Geodesy and Geoinformation, Technische Universitat Wien, Vienna (Austria)
**Corresponding Author's email: moonisali20@iitk.ac.in*

Abstract

Accurate forest biomass estimation is crucial for various applications, including carbon assessment and forest management. Terrestrial LiDAR scanners (TLS) are recognized for their precision in plot-level measurements. However, achieving precise volume estimation necessitates sophisticated reconstruction models, such as Quantitative Structure Model (QSM) techniques. This study delves into the impact of higher-order branches within QSM-based volume reconstruction. Using 10 artificially modelled trees, simulated in HELIOS++, we generate point clouds for various branch orders. Employing TreeQSM, we assess the impact of higher-order branches on volume estimation. Four models are created for each tree: trunk only, (trunk with 1st), (trunk with 1st and 2nd), and (trunk with 1st, 2nd and 3rd) order branches, resulting in 40 models. Simulated point clouds are generated using Riegl VZ-400 scanner within HELIOS++. Residuals are calculated as absolute differences between TreeQSM-generated volumes and reference volumes, expressed as percentages. Our findings unveil diminishing volume contributions as we include higher-order branches in a tree model. Trunk, Trunk with 1st, Trunk with 1st and 2nd order branches contribute 43%-60%, 79%-97%, and 92%-99%, respectively. In contrast, the 3rd order branches contribute a mere 5.17% on average. Higher order branches correspondingly intensified volume estimation uncertainty, with average residuals at 6.43%, 9.09%, 12.75%, and 16.96% for trunk, (trunk with 1st), (trunk with 1st and 2nd), and (trunk with 1st, 2nd, and 3rd) order branches, respectively. These findings show minimal volume contribution from the higher-order branches while they significantly increase the complexity and uncertainty in volume computation. Neglecting higher-order branches could enhance forest biomass estimation, crucial for leaf-filtering – a pre-processing task for QSM modelling. Manual or algorithmic leaf-filtering of small branches can be burdensome. This research offers comprehensive insights into QSM-based volume estimation, enhancing forest assessment practices. This finding is additionally important as higher-order branches are susceptible to wind-induced noise, more so than their lower-order counterparts.

Keywords: Volume extraction; TreeQSM; Quantitative Structure Models (QSM); Terrestrial LiDAR Scanners (TLS); Simulated Point Cloud; Higher order branches.

Introduction

Forests, the lifeblood of our planet, play a crucial role in maintaining ecological balance by sequestering carbon, preserving biodiversity, and regulating climate patterns. The accurate estimation of forest biomass is vital for making informed decisions in areas such as climate change mitigation, sustainable forest management, and carbon assessment. Technological innovations, particularly Terrestrial LiDAR Scanners (TLS), have significantly advanced our ability to capture detailed three-dimensional representations of forest structures at

the plot level, providing a wealth of data for scientific analysis.

To extract precise information about biomass from the intricate point clouds obtained through TLS, researchers commonly employ sophisticated methods such as meshing or Quantitative Structure Models (QSM). Meshing techniques, like Poisson Surface Reconstruction (PSR), face challenges in accurately capturing complex structures, particularly where multiple branches intersect closely, such as in the crown of a tree. Consequently, QSM approaches, especially the popular TreeQSM model developed by Raumonen et al. (2013), have become preferred due to their ability to remodel woody point clouds using basic geometric shapes like cylinders. This allows for efficient volume extraction, which can be converted into biomass or carbon content using appropriate conversion ratios.

However, the accuracy of QSM models is intricately linked to the inclusion of different orders of branches in the reconstruction process. This study delves into the nuanced impact of higher order branches on volume estimation, focusing specifically on the TreeQSM model. We aim to scrutinize the contributions of higher order branches to overall tree volume, determining whether their inclusion is warranted. By examining 10 artificially modelled trees, each with variations in branch orders, created using Arbaro tree modelling software (Arbaro, 2015), our objective is to delineate the distinctive contributions of different branch orders to overall volume reconstruction. The point clouds for our analysis are generated through simulations using the Riegl VZ-400 scanner within HELIOS++.

A critical step in QSM modelling is leaf-filtering pre-processing, especially under leaf-on conditions during TLS scanning. Accurate leaf-filtering for smaller-diameter higher-order branches poses a significant challenge, whether performed manually or through algorithms. This challenge arises due to the intricate nature of these branches, characterized by their dense foliage and susceptibility to the windy effect. Moreover, higher-order branches, characterized by dense foliage and susceptibility to wind, introduce noise in the scanned point cloud. This susceptibility further complicates the accurate representation of their geometry in the reconstructed models, impacting the overall precision of QSM-based volume estimation.

The significance of this research lies in its potential to refine existing forest assessment practices. Our findings, systematically exploring the impact of higher order branches on volume estimation, aim to provide practical insights for enhancing the accuracy of forest biomass assessments. Additionally, understanding the relationship between branch orders and estimation uncertainty is crucial for refining modelling techniques, directly impacting tasks such as leaf-filtering - a critical pre-processing step in QSM modelling.

As we navigate the intricacies of forest structure assessment, the subsequent sections of this paper will unfold a detailed analysis of materials and methodology, present results, engage in discussion, and draw conclusions. Through this exploration, we aim to contribute valuable knowledge accessible to diverse communities, dedicated to advancing the precision and reliability of forest biomass estimation methodologies.

Materials and Methods

Model Generation Using Arbaro Modelling Software

To evaluate Tree QSM's performance in volume extraction concerning different branch orders, we employed simulated data generated with Arbaro tree modelling software. The dataset comprised 10 artificial models, and various parameters were manipulated to introduce diversity into the models. These parameters included trunk length, branch size, tree shape, presence of lobes in the trunk, trunk tapering, branch splitting, and curvature, among others. Table 1 provides an overview of the diverse variations introduced in these parameters.

For robust testing of the contribution of each branch order, each tree model was generated in four variations: (1) Trunk only, (2) Trunk with 1st order branches, (3) Trunk with 1stand 2nd order branches, and (4) Trunk with 1st, 2nd and 3rdorder branches. Due to limitations in Arbaro software restricting the inclusion of branches beyond the 3rd order, the testing performance was confined to 3rd order branches. This approach resulted in the generation of four versions for each of the 10 trees, totalling 40 models. These models served as the basis for evaluating the volume contribution of different branches and investigating the impact of higher order branches on volume extraction using Tree QSM.

Table 1 illustrates the diverse characteristics of the generated tree models, with Tree 1 serving as the reference. Each subsequent tree model introduced specific variations, such as increased 1st order branches (Tree 2), varied tree shape with increased base size and lobes (Tree 3), and so forth. Notably, Tree7 represents an entirely

different tree, and its variations, observed in Tree 8 and Tree 9, can be further examined. All of these variabilities are summarized in the last column, 'Variations Introduced,' of Table 1.

Table 1 provides a comprehensive summary of artificial tree models and their variations. General parameters, branch parameters, and variations introduced are detailed for each tree, offering insights into the diverse characteristics introduced in the dataset. The extensive variability in tree characteristics aimed to ensure a comprehensive assessment of Tree QSM's performance in different scenarios, allowing for a more generalized interpretation of the results.

Table 1: Summary of Artificial Tree Models and Variations

Tree ID	General parameters				Branch parameters						Variations Introduced
	Tree shape	Base Size	Lobes parameters: No. of lobes	Lobes parameters: Lobe depth	Branch order	Length	Taper	Curvature	Splitting	Branches	
1	S	0.25	0	0	T	1.5	1.2	Yes	Yes	1	Reference Tree
					1st	0.5	1.2	Yes	Yes	6	
					2nd	0.7	1.2	Yes	No	10	
					3rd	0.6	1	No	No	10	
2					T						Increased 1st order branches compared to reference.
					1st					**10**	
					2nd						
					3rd						
3	**TF**	**0.4**	**2**	**0.3**	T	**3**					Altered tree shape, base, lobes, and increased branches.
					1st					10	
					2nd						
					3rd						
4	TF	**0.6**	2	**0.5**	T	3		**No**			Changed base, lobes, and removed trunk curvature w.r.t. Tree 3.
					1st					10	
					2nd						
					3rd						
5	TF	**0.5**			T	3		No	No		Removed lobes and trunk splitting w.r.t. Tree 3.
					1st					10	
					2nd						
					3rd						
6		**0.5**	**1**	**0.4**	T	3		No	No		Introduced lobes, altered shape, and reduced branches w.r.t. Tree 5.
					1st					**5**	
					2nd						
					3rd						
7	**C**	**0.6**	**1**	**0.5**	T	**3**	**1.5**	**No**	**No**		A very different tree with different shape w.r.t. Tree 1.
					1st		**1**			**10**	
					2nd	**0.5**	**1**				
					3rd	**0.5**	**1**				
8	C	0.6	1	0.5	T	3	**0.7**	No	No		Decreased trunk taper, increased 1st order branches w.r.t. Tree 7.
					1st		1			**15**	
					2nd	0.5	1				
					3rd	0.5	1				
9	C	0.6	1	0.5	T	3	**1**	No	No		Decreased trunk taper and 1st order branches w.r.t. Tree 7.
					1st		1			**5**	
					2nd	0.5	1				
					3rd	0.5	1				
10		0.5	1	0.2	T						Increased base size with lobes w.r.t. Tree 1.
					1st						
					2nd						
					3rd						

NOTE: S: Spherical; TF: Tend Flame; C: Cylindrical; T: Trunk; 1st: 1st order branches; 2nd: 2nd order branches; 3rd: 3rd order branches

Simulation through HELIOS++

Following the generation of diverse tree models, the next step involved simulating point clouds using HELIOS++ software, developed by (Winiwarter et al., 2022). The simulation process was conducted using the Riegl VZ-400 Terrestrial Laser Scanner (TLS) within the HELIOS++ environment. The TLS scanner was strategically positioned at four locations, each at a distance of 14.14 meters from the tree under consideration. Each tree model was scanned individually, ensuring uniform configurations for all simulations. The specifications for the Riegl VZ-400 scanner, integral to the simulation process, are detailed in Table 2.

The laser scanner's characteristics, such as beam divergence, pulse repetition frequency, scanning frequency, and scan angle range, play a crucial role in capturing detailed and accurate point clouds of the simulated tree models. These simulated point clouds serve as the foundational data for the subsequent volume extraction analysis using the Tree QSM model.

Table 2 : Riegl VZ-400 Scanner Parameters for HELIOS++ Simulation

Sensor	RIEGL VZ-400
Laser beam divergence	0.3 mrad
Pulse repetition frequency	300 kHz
Scanning frequency	120 Hz
Scan angle range	100° (-40° to 60° from the horizontal plane)

Volume extraction through Tree QSM

To extract the volume from the generated point cloud of woody structures, we utilized Tree QSM version 2.4.1 developed by (Raumonen et al., 2013). It is noteworthy that the version of TreeQSM plays a crucial role in volume extraction, and for this study, the latest version was employed. As Tree QSM is coded in MATLAB, it offers flexibility for manipulation based on specific requirements. The tool encompasses numerous parameters that can be tailored to the characteristics of the site and various factors, including tree height range.

Authors of Tree QSM suggested that three critical parameters, namely PatchDiam1, PatchDiam2Max, and PatchDiam2Min, play a pivotal role in the Tree QSM algorithm and need to be carefully chosen and optimized. It's important to highlight that, according to a study by (Calders et al., 2013), these parameters have no significant impact on the final reconstruction of the tree stem and main branches. Hence, default values were adopted for all trees in this study, ensuring consistency in the reconstruction and subsequent volume extraction process.

In addition to these parameters, all other settings were maintained at their default values during the reconstruction of QSM models. It is essential to acknowledge that, even with the same parameter settings, Tree QSM generates slightly different models with each run. Therefore, following the recommendation of the Tree QSM authors, we conducted five runs for each model with identical parameter settings and reported the average as the final volume. This approach provided a standardized baseline for the study, facilitating a comparative analysis of the volume contributions of different branches across the diverse tree models.

Results

Volume Contribution Analysis of Different Branch Orders

Fig. 1 illustrates the contribution of volume from various branch orders, providing insights into the distribution of volume within a tree. The analysis considered the volume contribution from the trunk only, trunk with 1st order branches, trunk with 1st and 2nd order branches, and trunk with 1st, 2nd, and 3rd order branches. The range of contributions is detailed in Table 3, indicating that trunk alone contributes 43% to 60% of the overall tree volume. When including the first-order branches, this contribution increases to 79%-97%, and further inclusion of 2nd order branches results in a range of 92%-99%. The average contributions from these categories are 57%, 85.5%, and 94.8%, respectively. Notably, the higher order branches (3rd order) contribute only 5.2% on average, emphasizing their minimal impact on the overall volume.

Fig. 1: Volume Contribution of Different Branch Orders.

Table 3: Volume Contribution Analysis for Different Branch

Branch Order	**% Volume Contribution Range (10 trees)**	**Average Volume Contribution (10 trees) in %**
Trunk only	43-60	57
Trunk with 1st order branches	79-97	85.5
Trunk with 1st and 2nd order branches	92-99	94.8

Uncertainty Analysis: Higher Order Branches in Tree QSM Volume Extraction

Fig. 2 illustrates the effect of including higher order branches on volume extraction through TreeQSM. The residual values in this study are calculated as the absolute differences between TreeQSM-generated volumes and reference volumes, expressed as a percentage of the reference volume. In general, the residual valuetends to increase with the inclusion of higher order branches. However, specific trees exhibit slightly different behaviours. For instance, Tree3 shows a minor decrement in residual value when adding 3rd order branches compared to when 2nd order branches are added. Still, the residual value increases with the inclusion of higher order branches. Similarly, Trees 8 and 9 show a slight decrement in residual value when including 1st order branches, but thereafter, a regular increment in volume uncertainty is observed with the inclusion of higher order branches. These variations in some trees are expected due to the high variability introduced in the artificial tree models listed in Table 1.

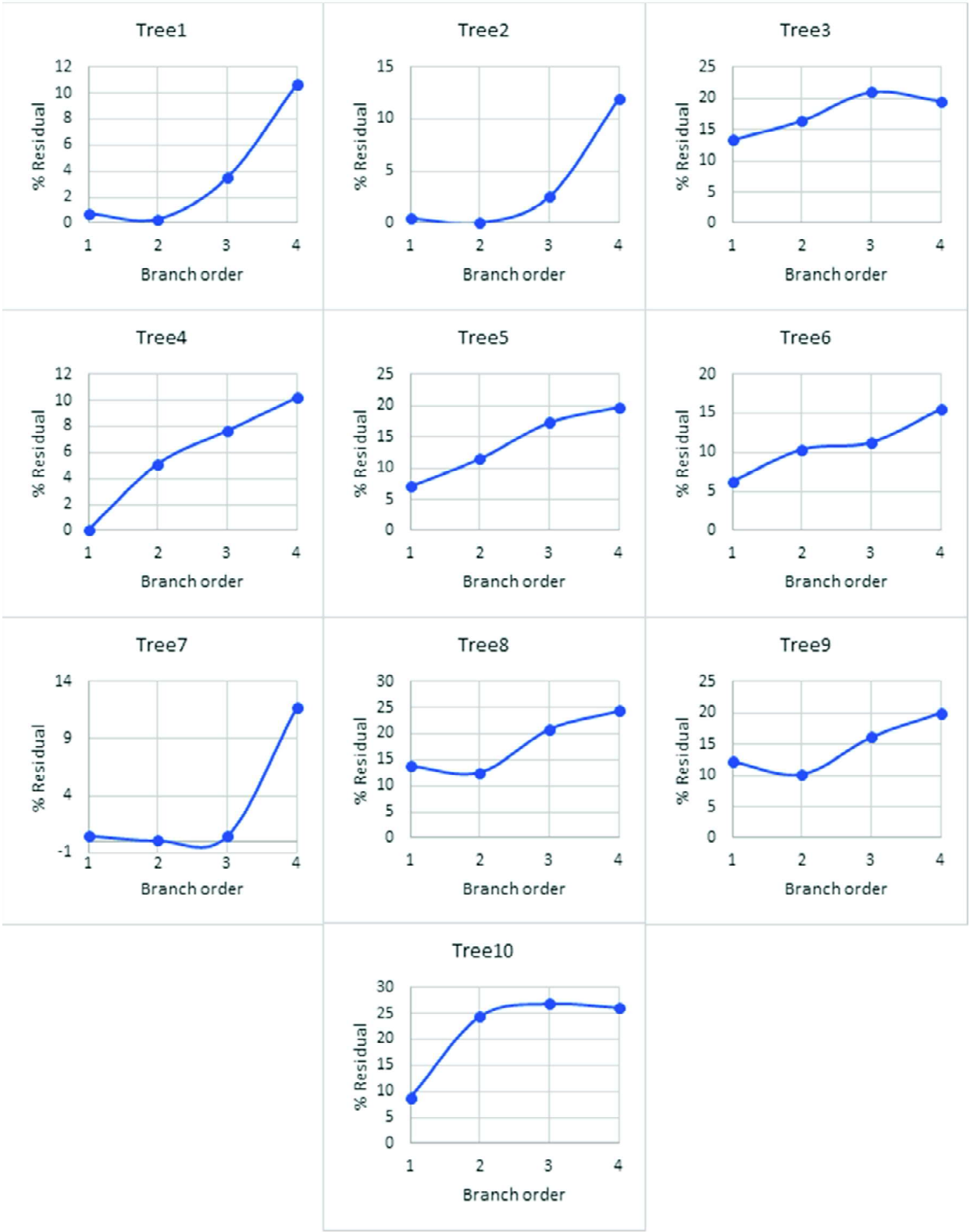

Fig. 2: A1 Residual Analysis of Higher Order Branch Inclusion in Volume Extraction. The horizontal axis corresponds to branch order, where 1 represents Trunk, 2 represents Trunk with 1st order branches, 3 represents Trunk with 1st and 2nd order branches, and 4 represents Trunk with 1st, 2nd, and 3rd order branches.

Discussion

Significance of Branch Orders in Tree Volume Distribution

The analysis of volume contributions from different branch orders provides valuable insights into the hierarchical structure of trees. The findings indicate that the majority of the tree volume is concentrated in the trunk, with contributions ranging from 43% to 60%. This dominance is expected, as the trunk serves as the primary structural support for the tree. As we incorporate first-order branches, the volume contribution significantly increases, reaching a range of 79% to 97%. This emphasizes the substantial role of the lower order branches in contributing to the overall tree volume. The subsequent addition of second-order branches further refines the distribution, with contributions ranging from 92% to 99%. Notably, the contribution of higher order branches (3rd order) averages at a mere 5.2%. This underscores their limited impact on the overall tree volume.

These findings have practical implications for forest biomass estimation and management. Focusing on the trunk and lower order branches may suffice for accurate volume estimation, streamlining measurement efforts and reducing complexity. This insight is particularly relevant for tasks such as leaf-filtering in pre-processing for Quantitative Structure Model (QSM) techniques (Ali et al., 2024).

Implications of Higher Order Branches in QSM-Based Volume Estimation

The examination of the impact of higher order branches on volume extraction through TreeQSM reveals nuanced patterns in volume uncertainty. In general, as higher order branches are included, the residual values tend to increase, indicating a higher level of uncertainty in volume estimation. However, specific trees exhibit diverse behaviours. For instance, Tree3 shows a minor decrement in residual value when adding 3rd order branches compared to the inclusion of 2nd order branches. This suggests a complex interaction between different branch orders, highlighting the intricacies of tree structure.

Trees 8 and 9, on the other hand, exhibit a slight decrement in residual value when including 1st order branches, followed by a consistent increment in uncertainty with the inclusion of higher order branches. These variations are expected due to the artificial tree models' high variability, as outlined in Table 1. The observed irregularities underscore the importance of considering tree-specific characteristics in QSM modelling.

These findings emphasize the need for careful consideration of higher order branches in QSM-based volume estimation. While their direct volume contribution is minimal, their influence on uncertainty highlights their indirect impact on accurate volume assessments. Understanding these dynamics contributes to the refinement of QSM techniques, guiding improved forest assessment practices.

Although this study focuses on analysing up to the 3rd order branches, the inclusion of higher-order branches (4th order and beyond) may further refine volume estimation. Due to the limitations of the Arbaro modelling software, we were unable to assess their contributions, but future work should explore their significance in real-world datasets, particularly in complex forest structures where these branches may play a more substantial role.

Conclusions

In conclusion, our comprehensive investigation aimed to enhance our understanding of the intricate relationship between branch orders and volume estimation in forest biomass assessments, particularly concerning the Tree QSM model. The significance of accurate forest biomass estimation cannot be overstated, given its pivotal role in climate change mitigation, sustainable forest management, and carbon assessment.

Insights from Volume Contribution Analysis

Through meticulous analysis of 10 artificially modelled trees, varying in branch orders and characteristics, we unveiled valuable insights into the distribution of volume across different branch orders. The dominance of the trunk in contributing to overall tree volume (43% to 60%) underscored its primary structural role. Notably, the substantial contributions of first-order (79% to 97%) and second-order branches (92% to 99%) indicated that focusing on these lower order branches may suffice for accurate volume estimation, streamlining measurement efforts.

Nuanced Understanding of Volume Uncertainty

The exploration of volume uncertainty associated with the inclusion of higher order branches in TreeQSM-based estimation revealed nuanced patterns. While, on average, higher order branches (3rd order) made minimal direct contributions (5.2%) to tree volume, their inclusion correlated with increased uncertainty in volume estimates. This understanding emphasizes the need to carefully consider the measurement of higher order branches and raises questions about their practical significance in forest assessments.

Implications for Forest Assessment Practices

These findings not only contribute to the academic understanding of tree structure but also hold practical significance for forest management strategies and climate change mitigation efforts. Prioritizing measurements on the trunk and lower order branches can enhance the efficiency of volume estimation techniques, especially in scenarios where detailed measurements of higher order branches might pose challenges. Moreover, understanding the dynamics of uncertainty associated with higher order branches contributes to the ongoing improvement of QSM techniques, guiding more accurate and reliable forest biomass assessments.

Overall, these findings have broader implications for forestry applications, particularly in forest management and biomass estimation workflows. By concentrating on the trunk and lower-order branches, forest managers can streamline efforts to measure tree volume and biomass, which are critical for carbon assessment and climate change mitigation strategies. Furthermore, this research supports the development of more efficient TLS-based forest monitoring systems, offering practical tools for sustainable forest management.

References

Arbaro (2015). Arbaro (v 1.9.9). Retrieved from https://sourceforge.net/projects/arbaro/.

Ali, M.; Lohani, B.; Hollaus, M.; Pfeifer, N. Benchmarking Geometry-Based Leaf-Filtering Algorithms for Tree Volume Estimation Using Terrestrial LiDAR Scanners. Remote Sens. 2024, 16, 1021. https://doi.org/10.3390/rs16061021.

Calders, K., Newnham, G., Herold, M., Murphy, S., Culvenor, D., Raumonen, P., Burt, A., Armston, J., Avitabile, V. and Disney, M. (2013). Estimating above ground biomass from terrestrial laser scanning in Australian Eucalypt Open Forest. In Proceedings SilviLaser 2013, 9-11 October, Beijing, China (pp. 90-97).

Raumonen, P., Kaasalainen, M.; Åkerblom, M., Kaasalainen, S., Kaartinen, H., Vastaranta, M., Holopainen, M., Disney, M., Lewis, P. Fast Automatic Precision Tree Models from Terrestrial Laser Scanner Data. Remote Sens. 2013, 5, 491-520. https://doi.org/10.3390/rs5020491.

Winiwarter, L., Esmorís Pena, A., Weiser, H., Anders, K., Martínez Sanchez, J., Searle, M., Höfle, B. (2022): Virtual laser scanning with HELIOS++: A novel take on ray tracing-based simulation of topographic full-waveform 3D laser scanning. Remote Sensing of Environment. Vol. 269. https://doi.org/10.1016/j.rse.2021.112772.

Acknowledgements

We extend our appreciation to the developers of Arbaro and HELIOS++ software. Their commitment to creating and maintaining these tools has been instrumental in our research. Arbaro's realistic tree models and HELIOS++'s advanced simulation environment provided the foundation for our analysis, enriching our understanding of forest structures. We acknowledge and value their contributions to open-access tools that foster collaboration in the research community.

Indian Cartographer, Vol. 44, No. 1 & 2, pp. 34-39
ISSN: 0972-8392 © INCA, 2024

Geospatial Blockchain: A Catalyst for Smart Governance and Sustainable Development

Mary Chingthianhoih
Department of Natural and Applied Sciences
TERI School of Advanced Studies, New Delhi (India)
Email: mary.chingthianhoih@gmail.com

Abstract

Driven by diverse data sources, the dynamic landscape of remote sensing is rapidly evolving along with technological advancements. Albeit, with the significant surge of geospatial data in veracity and volume, the conventional centralised data sharing and storage mechanisms encounter a multitude of challenges such as scalability, limited interoperability, vulnerabilities to single points of failure, and potential alterations consequently having adverse implications on governance. Thus, in times of expeditious developments, it becomes vital to recognise the need for transformative shifts in our methodology as we transition towards Web 3.0. Guided by this principle, the present research paper advocates for a decentralised approach underpinning a data-driven geospatial ecosystem, to develop a blockchain-based prototype using Ethereum and Inter Planetary File System (IPFS) via smart contracts written in Solidity with quantifiable indicators that operate on reward mechanism to incentivise users through Proof of Implementation (POI) in order to foster a collaborative and sustainable network. This synthesis not only catalyses a pivotal shift within the geospatial domain but also holds immense potential for governance as the decentralised framework enhances data security, transparency, and accessibility, aligning perfectly with its tenets; ushering a new era of smart governance that consequently, optimises resource management. By providing a robust and trustworthy framework, this study embarks on a quest toward unlocking new avenues of accessibility, credibility, and sustainability.

Keywords: Blockchain; Smart Contract; Decentralisation; Geospatial data sharing; Smart governance.

Introduction

Amidst the digital odyssey that shifted paradigms from binary machines to cognitive systems, the domain of remote sensing evolved into a cornerstone discipline, revolutionising our understanding of the Earth's intricate mechanism; enabling innovations across diverse sectors. Consequently, with the convergence of advanced sensors and sophisticated satellite capabilities, there is an unprecedented surge in the acquisition of geospatial data from an array of data sources, including Earth Observation (EO) satellites, Unmanned Aerial Vehicles (UAV), Light Detection and Ranging (LiDAR) sensors, Global Navigation Satellite Systems (GNSS), as well as Internet of Things (IoT) devices, catapulting into an era of information abundance (Wulder & Mask, 2018). The traditional centralised models, often employed to manage vast data repositories, are struggling to cope with the sheer

volume and diversity of data generated by remote sensing technologies (Li et al., 2018). Further, as the current global scenario reflects these intricate predicaments, disruptions in access to geospatial data and its dissemination across the internet have emerged as significant challenges, hindering the seamless flow of information critical for real-time decision-making and policy framework within governance and resource management. Ergo, it also raises concerns about data ownership and control along with security, underscoring the pressing need for a more efficient, innovative, and decentralised architecture within the realm of geospatial administration (Mavroudi, E. et al., 2020).

With the first implementation of blockchain technology through the creation of Bitcoin cryptocurrency by "Satoshi Nakamoto", decentralisation emerged as a transformative alternative that streamlines data acquisition, storage, and dissemination. As illustrated in Figure 1, a blockchain is a structured chain of data blocks, each containing transaction records that are cryptographically linked to the preceding block. Its characteristics of immutability, transparency, and consensus through a distributed network, coupled with its decentralised nature, establish an environment where data can be securely stored, verified, and shared among participants without intermediaries (Nakamoto, S., 2008). Further, blockchain transactions with smart contracts in user-to-provider interactions operate on a decentralised ledger system, ensuring secure and transparent exchanges.

Presently, while practical implementations remain limited due to their novel concept, proposals for a decentralised framework to store and share geospatial have been put forth in the existing literature. In a study by Molesky et al. (2008), blockchain is utilised as a database for monitoring satellite and debris orbits where it operates in distinct configurations but though it ensures the integrity of data and incorporates smart contracts, the study does not capitalise on other advantages of blockchain technology, such as enhancing trust and providing incentives. Another study by Leka et al. (2019), introduces a blockchain-based framework (D-GIS) for the storage and distribution of geospatial and though it leverages blockchain with an incentive mechanism to attract users, the data still resides in centralised storage which negates our objective. Howbeit, the research undertaken by Papantoniou, C. and Hilton, B. (2021) proposed a concept known as "Geoblockchain," which synthesised blockchain technology with Geographic Information Systems (GIS) which could potentially provide insights into the distribution, movement, and interactions of transactions in a spatial context, contributing to a deeper understanding of blockchain activities from a geographic perspective which is the catalyst to our engineering prototype.

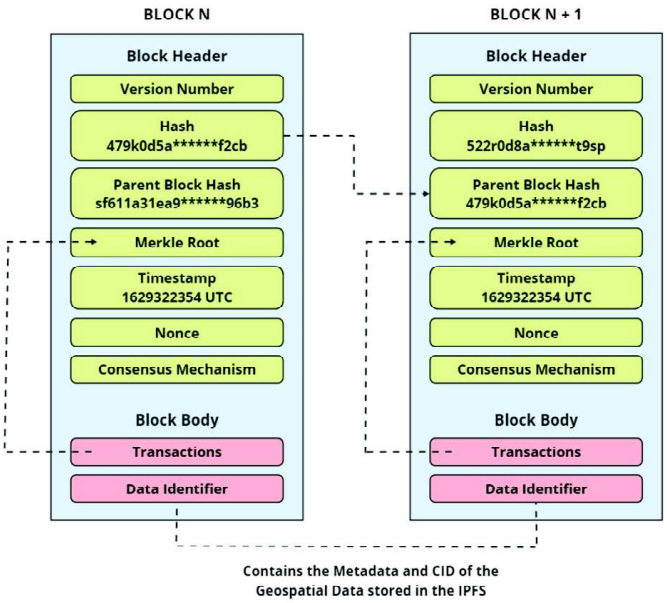

Fig. 1: Blockchain Structure for Geospatial Data

Thus, by exploring the interplay between the substantial generation of geospatial data and the transition towards decentralised Web3 platforms, we aim

i. To develop a geospatial blockchain model for a secure data-sharing mechanism to ensure data integrity, access control, and traceability for smart governance.

ii. To build a robust and decentralised geospatial data storage for the sustenance of the blockchain model.

Materials and Methods

Geospatial Application Architecture

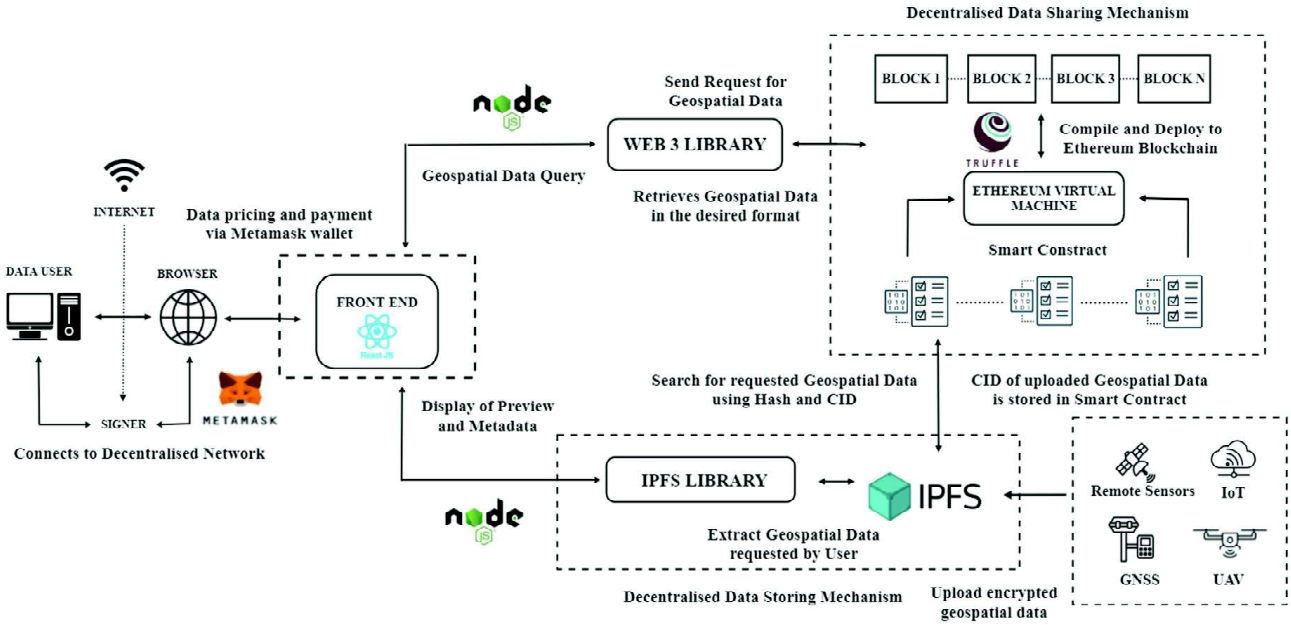

Fig. 2: Architecture and Design Implementation

As shown in Fig. 2, the entire system operates on a tripartite architecture which has a sequential operation when transactions are initiated from geospatial data users to providers. To begin with, the front-end was developed using React.js which is a JavaScript library used for building dynamic user interfaces (UIs) while minimising the need for direct manipulation of Document Object Model (DOM), which can be resource-intensive. The integration of Metamask, a browser extension, provides users with a secure gateway to access their Ethereum accounts, enabling them to sign smart contracts. At the core of the architecture lies the back-end, which processes the user requests, interacts with the Ethereum Virtual Machine, an open-sourced decentralised computing environment, and stores geospatial data on IPFS, which is a distributed P2P protocol designed for storing and sharing content in a resilient, permanent and decentralised manner. While Node.js acts as the bridge between the front end and the back end, Web3.js serves as the intermediary library that enables the system to deploy transactions and communicate with Ethereum nodes. The smart contracts, written in Solidity were developed in Remix IDE which defined the logic for access control, storage, and management of geospatial data. The Truffle framework was used to execute smart contracts, in conjunction with Ganache which streamlined the testing and deployment of smart contracts on a local Ethereum environment. This combination ensures efficient contract deployment and thorough testing which minimises potential vulnerabilities when executed on the Mainnet.

Design Implementation

Geospatial data is acquired and uploaded in all levels of processing (raw, georeferenced, orthorectified, geometrically and/or radiometrically corrected,) and data formats (CEOS, GeoTiFF, SAFE, HDF, NetCDF, KMZ/KML, GeoJSON, JPEG, ENVI, GRIB, LAS and LAZ) as well as GNSS formats (RINEX, SP3, NMEA, BINEX and IONEX) in the IPFS network through EVM. Though different data providers adhere to distinct naming conventions; upon storing in the IPFS, the geospatial data sheds its association with these conventions. Instead, it is linked to a generated CID (Content Identifier) which is stored within the Ethereum blockchain along with its metadata which is later used for retrieval when required. From the users, the system starts with user registration, where once successful, it is hashed and a new block is added after a consensus agreement by all the nodes. It is then broadcasted across the entire blockchain network thereby having the privilege and direct admittance into

the private network. When the users get access to the website through their unique account ID, they interact with a map carousel and define their search criteria such as type of geospatial data, level of processing, satellite sensor, data format, geographic area, time range, and other filters that suit their requirements. Upon submitting the criteria, the front end sends a request to the IPFS network to retrieve the content based on the CID that matches the search criteria. The retrieved geospatial data along with the metadata is displayed within the UI, allowing the user to preview the image before confirmation. After confirmation, the account submits a transaction that triggers the retrieval process. The smart contract receives the request retrieves the associated CID and provides access to the data on the IPFS through Web3.js where all the interactions and transactions related to the retrieval process are recorded on the Ethereum network, ensuring transparency and accountability.

Results and Discussions

For the purpose of initial operation on the Mainnet, we utilised a raster dataset sourced from Resourcesat 2 LISS-III. However, it is important to note that the designated data provider will upload the geospatial data in the ultimate operational execution over the main IPFS network.

Fig. 3: Uploaded Geospatial Data in IPFS Network

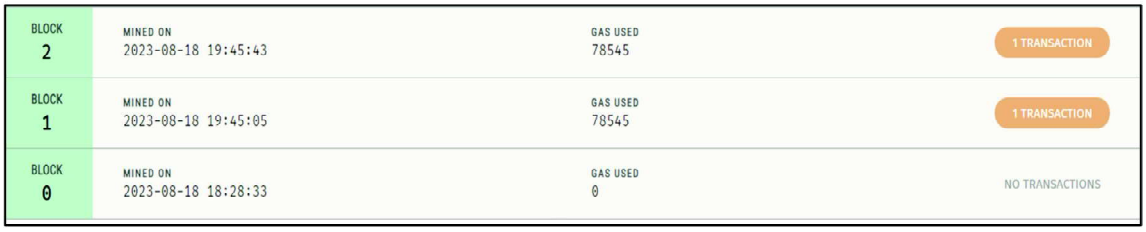

Fig. 4: Successful Transaction in Ganache

As depicted in Fig. 3 and Fig. 4, the geospatial data was effectively uploaded onto the IPFS network. In this process, the geospatial data was broken into smaller parcels as illustrated in Figure 5, each with a fixed size and a unique SHA-256 cryptographic hash for identification. Additionally, a root CID is generated for the entire dataset, representing the top-level hash of all the parcels combined was generated QmZXzw1Ly ECpGtQL8ujr8VTEDqaqCSSpGz3 pn2UCa9xF16. This value was compiled and subsequently stored within the smart contract situated in the EVM. Using my registered Meta Mask account, the front end seamlessly established communication with the decentralised backend which was evident as the frontend successfully displayed a preview of the desired data after applying the specified user criteria, as shown in Fig. 6.

Upon clicking the confirm button, the website underwent a brief loading phase as it retrieved the geospatial data from the IPFS via the blockchain. The request uses the root CID from various peers of IPFS nodes within the network. As each parcel is retrieved, the original image is reconstructed by reorganising them based on their order and relationships. Here, through the Ethereum that transfers the CID, IPFS employed a Merkle-DAG structure, where each node points to its parent nodes. Once retrieved, the data was automatically reconstructed and downloaded from the web browser to our local computer. Upon implementation of the framework, the integration of Ethereum heightened data confidentiality and its efficient retrieval mechanisms,

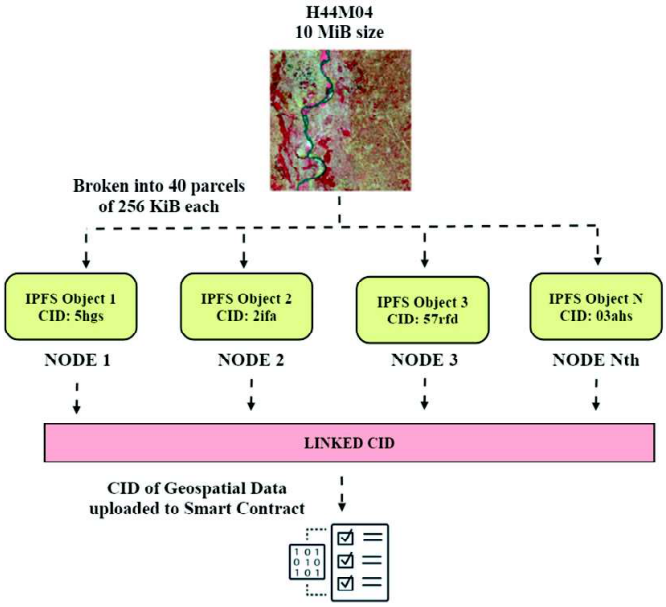

Fig. 5: Geospatial data breakdown in IPFS

Fig. 6: Preview of the requested Geospatial Data

significantly elevating the accessibility and expediency of geospatial image retrieval — a crucial aspect for informed decision-making and smart governance as it allows governments to handle sensitive and critical data with confidence in limited time. Operating as a P2P network, direct communication reduces dependence on intermediaries minimising the potential for delays caused by third-party involvement in governance, leading to accelerated data transfer and diminished overall energy consumption in transactions. The execution of smart contracts empowered data providers to exert precise control over access permissions for the management of geospatial data sharing environment. It ensures that only authorised individuals or entities can access specific geospatial data. In a smart governance context, this is vital for ensuring that sensitive information is only available to those with the appropriate permissions, safeguarding national security and privacy. Complemented by the storage infrastructure established on IPFS, only metadata and hash values were stored within the block, with the complete geospatial data residing in IPFS. This yielded a marked reduction in data redundancy and on-chain geospatial data volume, resulting in fewer transactions and reduced gas fees (ETH rate) required for data administration within the Ethereum network. This is particularly beneficial for governments with limited resources, as it allows them to allocate funds more efficiently.

Given the pre-existing possession of an Ethereum wallet by the user, each valid registration extends to them a complimentary free purchase during their first visit. Subsequently, upon re-engagement, the provision of a substantiated Proof of Implementation (PoI) pertaining to their application of the resources for fostering sustainable development and community empowerment warrants the issuance of a corresponding token. These tokens hold utility within the internal system, enabling transactions and participation incentives, thereby nurturing an engaged and collaborative ecosystem of geospatial data users that transcends data-sharing limitations. This, in turn, established a virtuous cycle of information exchange, wherein users are not only beneficiaries but also active contributors to the growth of the repository, fostering a self-sustaining ecosystem of geospatial information. Consequently, this decentralised architectural approach ensured unwavering data transaction traceability and immutability, thereby enhancing transparency and accountability—an imperative for upholding the integrity of geospatial data sharing initiatives.

Conclusion

The fusion of innovative systems, namely the Ethereum and IPFS within the domain of remote sensing, presents a robust framework that addresses challenges in geospatial data storage and sharing while paving the way for smart governance. With regards to its contribution to the UN Sustainable Development Goals (UNG, 2015), the proposed framework caters to all the goals; primarily aligning with Goal 9, i.e., Industry, Innovation, and Infrastructure, by advancing innovative solutions for efficient and decentralised storage, contributing to the

establishment of resilient infrastructure and sustainable energy consumption for geospatial data management. Further, the efficient storage and tamper-proof nature of the blockchain facilitated by the framework contribute to collaborative research efforts enhancing accountability and fostering collaborations among various institutions (Goal 16: Peace, Justice, and Strong Institutions). Thus, it can support developmental work and decision-making process that cover a wide range of social, economic, and environmental issues as they are all interconnected such as remote sensing data is indispensable for monitoring and mitigating poverty (Goal 1: No Poverty), hunger and food security (Goal 2: Zero Hunger) as well as climate-related challenges (Goal 13: Climate Action). In conclusion, this framework not only revolutionises geospatial data management but also provides a solid foundation for smart governance and sustainable development. It ensures that critical information is handled securely, accessed promptly, and utilized effectively for the betterment of communities and the environment. The transparency, accountability, and cost-effectiveness it brings to data management are indispensable in the pursuit of sustainable and efficient governance.

By expanding the framework to incorporate live data will transform the model into an adaptable repository, furnishing real-time insights into diverse variables like weather trends, occurrences of natural calamities, and alterations in land usage. Additionally, the following propositions can also be considered for future work:

i. Establishment of mechanisms for fault tolerance to ensure robustness in the face of unexpected scenarios
ii. Optimisation of the transaction verification time to ensure that the blockchain operations remain efficient, minimising delays in geospatial data sharing and retrieval processes
iii. Evaluate the storage space to manage the growth of geospatial data over time, preserving the scalability and sustainability of the system

Thus, in essence, the development of a functional model using Ethereum and IPFS for storing and disseminating geospatial data represents a significant stride toward achieving sustainable governance.

References

Li et al. (2018). Building a distributed space-based remote sensing data centre. Future Generation Computer Systems, 79, 631-639.

Leka, E. et al (2019). Design and Implementation of Smart Contract: A Use Case for Geo-Spatial Data Sharing. In 2019 42nd International Convention on Information and Communication Technology, Electronics and Microelectronics (MIPRO) (pp. 1565–1570). https://doi.org/10.23919/MIPRO.2019.8757159

Mavroudi, E. et al. (2020). Decentralized data management in remote sensing blockchain networks: The case of R-SENSE. Journal of Parallel and Distributed Computing, 136, 157-167.

Molesky, M. J. el at (2018). Blockchain network for space object location gathering. In 2018 IEEE 9th Annual Information Technology, Electronics and Mobile Communication Conference (pp. 1226–1232).

Nakamoto, S. (2008). Bitcoin: A Peer-to-Peer Electronic Cash System.

Papantoniou, C. and Hilton, B. (2021). Enterprise Solutions Criteria in the Age of GeoBlockchain: Land Ownership and Supply Chain. In Proceedings of the 54th Hawaii International Conference on System Sciences (p. 5307).

United Nations General Assembly. (2015). Transforming our world: The 2030 Agenda for Sustainable Development. A/RES/70/1.

Wulder, M.A. and Masek, J.G. (2018). Satellites: Make Earth observations open access. Nature, 555(7696), 30-32.

Acknowledgments

I would like to express my profound gratitude to Dr. V. Poompavai, Scientist/Engineer SF at RRSC South, for her exceptional guidance, insightful inputs, and unwavering support. Her expertise and willingness to share knowledge have greatly enriched this research paper along with my learning experience.'

Indian Cartographer, Vol. 44, No. 1 & 2, pp. 40-48
ISSN: 0972-8392 © INCA, 2024

Radiometric Correction of High-Resolution SAR Data in Presence of Pointing Error

Swati Upadhyay*, Sumit Pandey, Nidhi Chaubey, M.V. Srivally, B. Asha Rahi, Neeraj Mishra and **R. Chandrakanth**
Advanced Data Processing Research Institute, DOS, Hyderabad (India)
**Corresponding Author's email: swati@adrin.res.in*

Abstract

Synthetic Aperture Radar (SAR) is an active instrument where an area on ground is illuminated by the signal transmitted from the sensor in microwave spectrum and the convolved backscatter return from the ground is received by the polarized antenna to form an image. Sufficient guard band is provided in a Pulse Repetition Interval (PRI) cycle to switch the antenna from transmission to reception and vice versa. The 3dB signal of the main lobe is collected in receiver to form an image. Data Window at receiver decides the collection duration of signal and Start Window Start Time (SWST) determines the start location of collection of radar return from the ground. The pointing of beam signal generated by the sensor and the SWST plays a key role in making seamless radiometric product in elevation. A small pointing error at the antenna or change in the opening of SWST at the receiver lead to collection of signals other than 3dB range of main beam and hence results in radiometric misbalances in SAR data, prominently visible in high frequency low swath X band sensors. A radiometric correction method is developed in Data Processing Chain of SAR sensor which utilizes the generic beam profile of individual beams along with the data specific Start Window Start Time (SWST). This allows to effectively generate the seamless radiometric product, even in the presence of pointing error in the antenna. Peak estimation from the coarse resolution raw data along with sensor parameters is used for estimation of mismatch between the actual and expected centre of the signal. This study is done on X band SAR imaging system with parabolic antenna using mechanical steering to cover wide off-nadir range. This method of radiometric correction is found to be especially suited for multi-beam mode imaging technology.

Keywords: SAR, antenna, radiometry, window start time, data window, main lobe.

Introduction

Synthetic Aperture Radar (SAR) is an active instrument, used for day and night imaging in all-weather condition. Transmission and reception within the PRI cycle ensures the construction of a line at coarse resolution. Since SAR is a side looking ranging instrument, range measurement is taken into consideration to synchronously transmit and receive coherent signal leading to construction of raw data. The mechanical antenna using single or multiple feed elements or phased array antenna can be employed in monostatic fashion for acquisition of an image (Walter G. Carrara.). The antenna is pointed to the desired Area of Interest and signal is transmitted from the feed elements within the PRI cycle. The bandwidth of the transmitted signal determines the actual resolution achieved in the

data. The monostatic antenna is then switched to reception mode within the PRI cycle to receive the signal return from the previously transmitted signal determined by the Number of Pulses in Air (NPRI). Overall reception time of the data window determines the swath. Acquisition of multiple such PRI cycles enables construction of raw data of multiple lines. The reception of the antenna is switched on such that to acquire the 3dB return of the main lobe of the transmitted signal. This is done by considering the ranging of the signal of the side looking SAR. The switching on time of the antenna for reception is known by the term Start Window Start Time (SWST).

Single SAR system can image in multiple acquisition modes which allow for coverage of narrow to wide swath ranging from high to medium resolution respectively. To further enhance the capability of wide swath and short revisit time, multiple beams are employed in single acquisition. The selection of multiple beams can be done mechanically in parabolic antenna or can be managed electronically in phased array antenna, depending on the choice of antenna in SAR system specific to the sensor.

The beam profile of the antenna is used for antenna pattern correction in elevation (Jianjun Huang, Jie Chen, 2022). The beam profile can be estimated in controlled environment before the launch of satellite (SAND2006-2632 Unlimited Release Printed April 2006). It can also be estimated from the gamma product of the homogeneous region such as amazon rainforest after the launch of satellite (A. P. Luscombe and A. Thompson, 2001) (Manfred Zink, Betlem Rosich, 2002). This is a part of radiometric calibration procedure done from time to time to monitor the health of satellite in operational period. By default, the antenna pattern fall of the raw data in range can be used to observe the profile patterns for individual data. Necessary care should be taken to avoid the domination of coherent target while estimation of profile from the raw data (Maneesha Gupta, B. Kartikeyan, 2014).

Pointing error at the time of transmission or calculation of improper range for SWST at the time of reception lead to recording of region outside the 3dB width of the main lobe. Such signal suffer lack of radiometric information and radiometric misbalance is observed even after radiometric normalization using the antenna models. This kind of errors are more evident in high resolution sensors employed in X band. The antenna beam width of such high frequency systems is quite narrow, thereby leading to narrow swath of high resolution. Even a small error in pointing or calculation of SWST lead to quite presentable radiometric errors present in the data due to imaging outside the 3dB width of the main lobe of the narrow beam width signal.

The current paper presents an approach for determination of SWST error present in the data. The same can be calculated in term of pointing error in degree. The actual peak of the data within the swath is computed and compared with ideal peak location expected in the data in the ground plane. The difference of the two is converted to slant range plane to determine the error at reception. This is converted to timing error in SWST at the reception. It can also be converted to pointing error in terms of degrees at transmission. This information is useful for adjustments of feed elements in future acquisitions, Also, this information is used while radiometric normalization using the antenna models. It was found that incorporation of this information in radiometric normalization leads to balance radiometric products even when acquired outside the 3dB width of the main lobe.

Theory and Basic Operation Principles

Transmission of signal of pulse width duration within the PRI cycle from the antenna illuminates the area of interest on ground. In monostatic antenna, same antenna transmits the signal to the ground and receive the signal backscatter from the ground from previous PRI cycle as shown in Fig. 1 (left). This signal consists of the main lobe where 70 percent of the energy is accumulated within the 3dB width of the window. Although the signal does not only consist of main lobe, but also many side lobes and gradually diminishes away from the main lobe. Fig. 1 (right) shows the signal profile on the ground of the signal generated from the X band sensor. The backscattered signal from the ground returns towards the sensor after a specific PRI cycle is determined by the distance between the ground and the sensor, speed of the sensor and the PRI duration as given in equation 1.

$$nPRI = int(\frac{ct}{2xVs}) \quad \text{Eq. (1)}$$

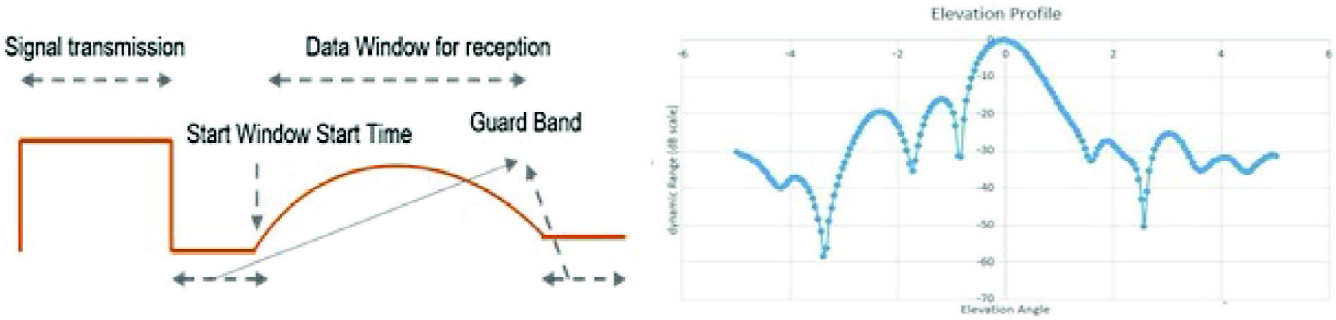

Fig. 1: Mono static antenna beam profile generation and data reception. (Left) PRI cycle (Right) Beam profile from X band SAR sensor

Where, c is the speed of light, t is the pulse width, Vs is the speed of the sensor and PRI is the pulse interval. The antenna is switched to reception mode and the signal is received at SWST for data window du- ration. The null to null and 3dB illumination of the transmitted signal is shown in figure 2(a) and figure 2(b) respectively. The SWST is calculated using the ranging equation within the PRI duration. Guard band need to be maintained properly while switching from transmission to reception and vice versa. Precise beam pointing at the time of transmission and determination of accurate SWST at reception is necessary to receive the signal return within the 3dB width of the signal. Any lead or lag in the estimation of SWST results in the shifting of data window outside the 3dB width region and collection of signals of less backscatter return from the target. The conceptualization of the shifting of data window in near and far range due to pointing bias or ambiguity in SWST calculation is shown in figure 2 (c). SWST window play a major role in capturing the 3dB region data. Any lead in opening of window result in early collection of data as shown in figure 4, thereby information content in near range go missing. Similarly, any delay in opening of data window result in lack of information content in far region of the data. The same effect is imposed on the data on improper pointing of the beam at the time of transmission.

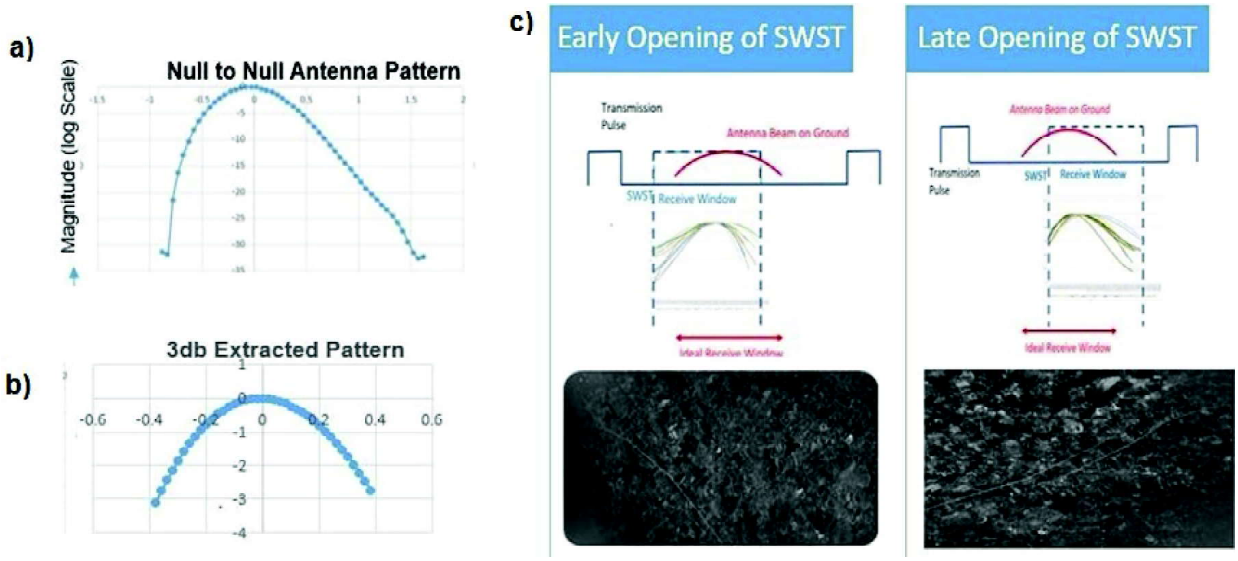

Fig. 2: a) Null to null beam pattern b) 3dB illumination profile of the transmitted signal c) Effect of Pointing Error and SWST bias on data window

Similarly, any delay in opening of data window result in lack of information content in far region of the data. The same effect is imposed on the data on improper pointing of the beam at the time of transmission. The actual peak of the data can be used for the estimation of SWST error, and can be converted to pointing error in degrees. The slant range at start is known for the data. The ideal slant range peak is expected to be at the centre of data as the peak of 3dB occur at the centre. Hence, the ideal peak range is calculated using equation (2) as

$$R_{peak\_ideal} = R_s + \partial_r \times \frac{N_p}{2} \text{Eq.} \quad (2)$$

Where, R_s is the slant range at start of the swath, ∂_r is the sampling distance, and N_p is total number of pixels in the swath. The actual peak of the data is estimated from the raw data at coarse resolution. This is done to avoid any ambiguities due to the presence of strong coherent scatterers within the swath. Also, the values are averaged over all azimuth lines to further avoid bias towards the presence of coherent dominant scatterers even at coarse resolution. The 3dB beam width of the signal is subtracted from the actual peak estimated from the data using equation (3) to provide the start slant range corresponding to this peak value.

$$R_{start\_actual\_peak} = R_{actual\_peak} - R_{start\_3dB\_width} \quad \text{Eq. (3)}$$

Where, $R_{start\_3dB\_width}$ is the slant range at the start of 3dB beam width of the antenna given by equation (4) as

$$\theta_{3dB\_width} = \frac{0.88 \times \lambda}{L} \quad \text{Eq. (4)}$$

Where, λ is the wavelength and L is the length of the antenna of the SAR system. To obtain the actual time difference termed as SWST bias, these starts slant ranges are converted into time as given in equation (5) and equation (6) respectively, as

$$t_{ideal\_start} = \frac{2 \times R_{ideal\_start}}{c} \quad \text{Eq. (5)}$$

$$t_{actual\_start} = \frac{2 \times R_{start\_actual\_peak}}{c} \quad \text{Eq. (6)}$$

NPRI and PRI are then used to determine the actual SWST as mentioned in equation (7) and equation (8) as,

$$SWST_{ideal} = t_{ideal\_start} - NPRI \times PRI \quad \text{Eq. (7)}$$

$$SWST_{actual} = t_{actual\_start} - NPRI \times PRI \quad \text{Eq. (8)}$$

The difference of $SWST_{ideal}$ and $SWST_{actual}$ gives an error in the calculation of the SWST time in reception chain using equation (9) as

$$SWST_{bias} = t_{ideal\_start} - t_{actual\_start} \quad \text{Eq. (9)}$$

The same can be converted into the pointing bias at the time of transmission by estimating the look angles at ideal and actual peak using equation (10) an equation (11), given as

$$\theta_{ideal\_peak} = cos^{-1}\{\frac{[(R_E + H)^2 + R^2_{peak\_ideal} - R_E^2]}{2 \times (R_E + H) \times R_{peak\_ideal}}\} \quad \text{Eq. (10)}$$

$$\theta_{actual\_peak} = cos^{-1}\{\frac{[(R_E + H)^2 + R^2_{actual\_peak} - R_E^2]}{2 \times (R_E + H) \times R_{actual\_peak}}\} \quad \text{Eq. (11)}$$

Where, RE is the Earth Radius and H is the height of the satellite. Pointing error is then estimated as given in equation 12 as,

$$\delta pointing\_error = \theta ideal\_peak - \theta actual\_peak \quad \text{Eq. (12)}$$

If $\delta pointing\_error$ is negative, the reception window starts before hand, and hence less signal strength is observed in near range data, while positive $\delta pointing\_error$ presents the delay in opening of data window, leading to losing signal strength at the far range signal. The overall flow of the algorithm for generation of precise radiometric product both in the presence and absence of SWST error in the data is represented in Fig. 3. The algorithm is dependent on individual data for the calculation of actual peak, extraction of 3 dB region from the antenna model and then correct the elevation pattern from the processed Slant Range Detected product at high resolution.

Fig. 3: Flow Chart for correction of radiometry in elevation in presence of SWST error

Results and Discussion

Pointing error and SWST errors computation in Initial Phase Operations of the sensor help in establishing a feedback mechanism to ensure adjustments in future data acquisitions to avoid inconsistencies and generate proper radiometric normalized products. It also helps in radiometric correction of biased data using antenna model or statistical approach. Figure 4 represent image which do not contain any SWST or pointing bias. The image is acquired in right look mode at an off-nadir distance of 375 km with a look angle of 32.51 degree. The Start Slant range, ideal and actual peak range values along with SWST error and pointing bias calculated using the current algorithm for the image is present in table 1. Since the image do not suffer from any SWST or pointing error, the actual peak of low-resolution data matches closely with the expected location at the centre as can be seen from row 1 of column 3 and column 4 in Table 1.

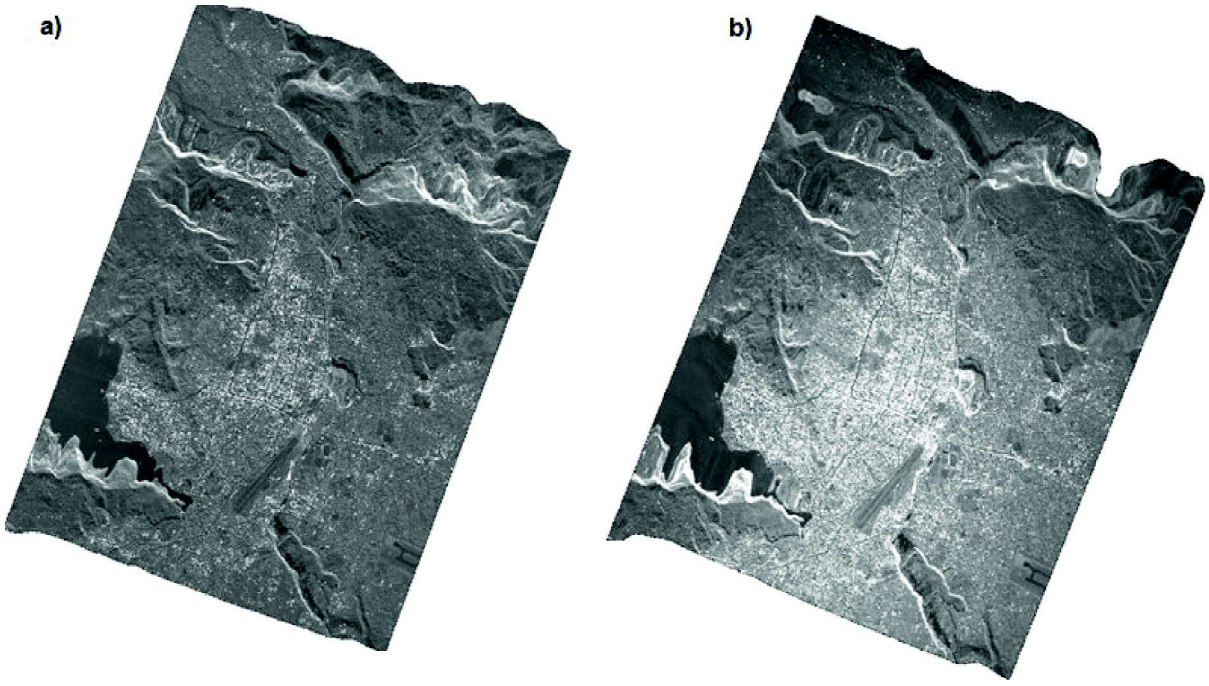

Fig. 4: (a) X band image at 1 m resolution within 3dB illumination.
(b) X band image at 1 m with late opening of SWST

Table 1: SWST and Pointing Error calculated from data in Fig. 6 (a) and 6 (b) respectively

Start Slant Range	Ideal Slant Range Peak	Actual Slant Range Peak	SWST error (microseconds)	Pointing Bias (degree)
697603	704070	704098	2.5	0.009
683814	689714	688835	8.1	0.10

Fig. 6 (b) represent the image of the same area. To verify the effect of SWST error and pointing bias on image, other acquisition parameters were kept similar. Image mode is right and off nadir distance is 362 km. The image suffers pointing bias of 0. 10 degrees. Presence of SWST time error impacts the peak shift in the expected and ideal scenario as observed in row2 of column 3 and 4 in Table 1 respectively.

Since actual slant range peak occur before the ideal slant range peak, data suffer degradation in radiometry at far range. This pointing error need to be taken into consideration while antenna pattern correction for radiometric normalization. Similar evaluation of presence of SWST time bias or pointing bias is done for other images to qualify the need for accurate antenna pattern correction especially in presence of pointing bias. Table 2 represents the data acquired from X band sensor at 1 m resolution at an off- nadir distance of 197 km. The 3dB swath for the data is estimated to be 10km. The pointing bias present in data is not taken into consideration while

doing antenna pattern correction and the correction is done using traditional approach from the centre of the data. The image thus suffers radiometric degradation at far range as presented in Fig. 5(a). The same image is now accounted for presence of pointing bias at the time of antenna pattern correction using the current approach and presented in Fig. 5(b). Pointing error of 0.29 degree is noted as presented in Table 2.

Since image suffer considerable pointing error, product suffer degradation in radiometry using traditional

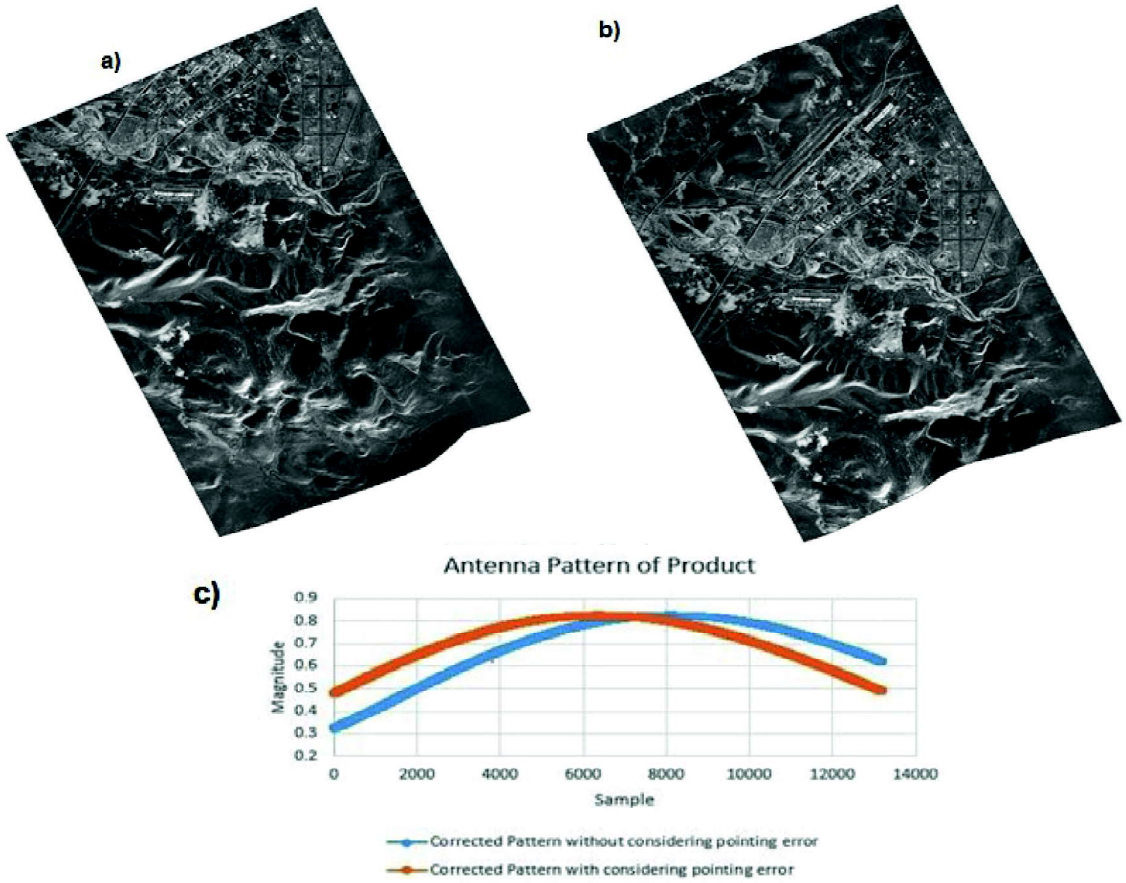

Fig. 5: (a) Product of X band sensor at 1 m resolution without pointing error consideration in radiometric correction (b) Product of X band sensor at 1 m resolution with pointing error consideration in radiometric correction using the proposed approach. (c) Antenna Pattern of 5(a) [blue] and 5(b) [orange] after correction

Table 2: SWST and Pointing Error calculated from data in Fig. 5

Start Slant Range	Ideal Slant Range Peak	Actual Slant Range Peak	Pointing Bias (degree)
607144	612853	611569	0.29

approach where this error is not taken into consideration as evident from the antenna pattern of the corrected product presented in figure 5 (c). when the proposed technique is used for radiometric correction, balanced radiometric product is obtained. The same is proved by the antenna pattern of the corrected product presented by orange line in graph of figure 5 c). The validation of the algorithm is also done for data sets which do not suffer from pointing error to establish the robustness of the current approach. The data which do not suffer pointing error at transmission is radio metrically balanced from the centre of the swath for valid region of 3dB. The peak of the data in such case match approximately with the product generated using the current approach. Fig. 6 represents an image from X band sensor at 1 m resolution where the pointing error is almost negligible as shown in Table 3. The proves that the current approach works in generic fashion for all cases in the presence and absence of pointing error in the data.

When multiple beams are operated together in

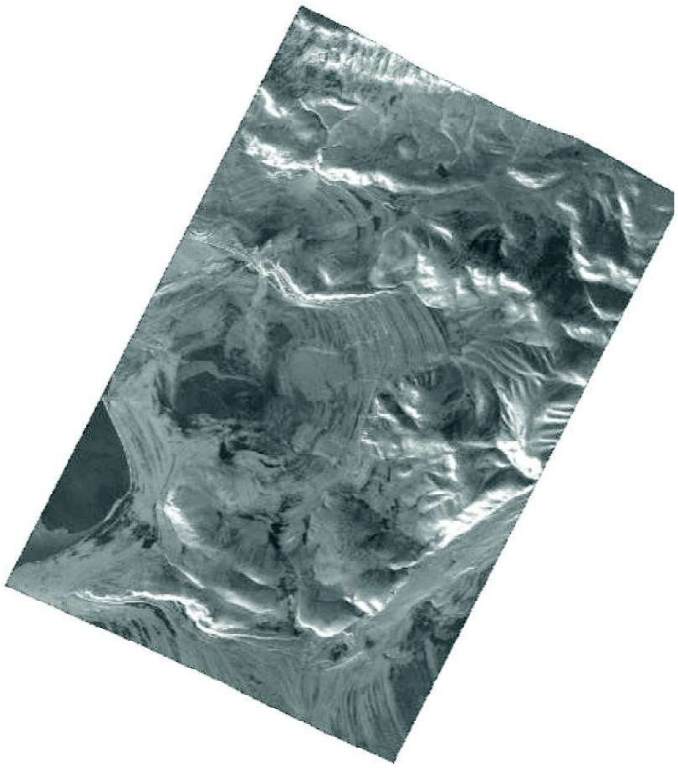

Fig. 6: X band image at 1 m resolution with pointing bias correction using the proposed method for image where pointing error is negligible

Table 3: SWST and Pointing Error calculated from data in Fig. 6

Start Slant Range	Ideal Slant Range Peak	Actual Slant Range Peak	Pointing Bias (degree)
837794	845270	844891	0.02

multiple iterations to increase the coverage in case of mosaic mode acquisitions, radiometric correction to ensure seamless mosaic across range in presence of pointing error becomes a challenging task. Radiometric correction using current approach ensure seamless radiometry across beams since, corrections are performed across the peak in individual beams. This ensures accommodation of varying pointing error in individual beams at multiple iterations. To acquire the wide swath of 25km x 25km from X band of narrow beam width, 4 beams are operated simultaneously one after the other for 6 iterations to acquire the swath of 25 km x 25 km. Each iterations of different beams suffer from different pointing error as shown in figure 10. This method of radiometric correction could successfully estimate the pointing bias of each iteration and correct the radiometry accordingly. As a result, seamless radiometry could be achieved across the full swath as shown for multiple iteration of one beam in Fig. 7(a).

Estimation of pointing error and application of antenna pattern correction while accommodating this error is necessary either in statistical correction or model-based correction approach for achieving high quality radiometric products in active instrument like SAR. IT becomes especially necessary in multi beam acquisition to ensure seamless radiometry across beams.

Conclusion

SAR is an active instrument where signal is transmitted and then received back at the sensor which is backscattered from the area illuminated within the beam width of the signal. To properly receive the backscatter information from the region, it is necessary to coordinate the antenna in a manner to capture within the 3dB beam width of the backscattered signal. Since 3dB signal

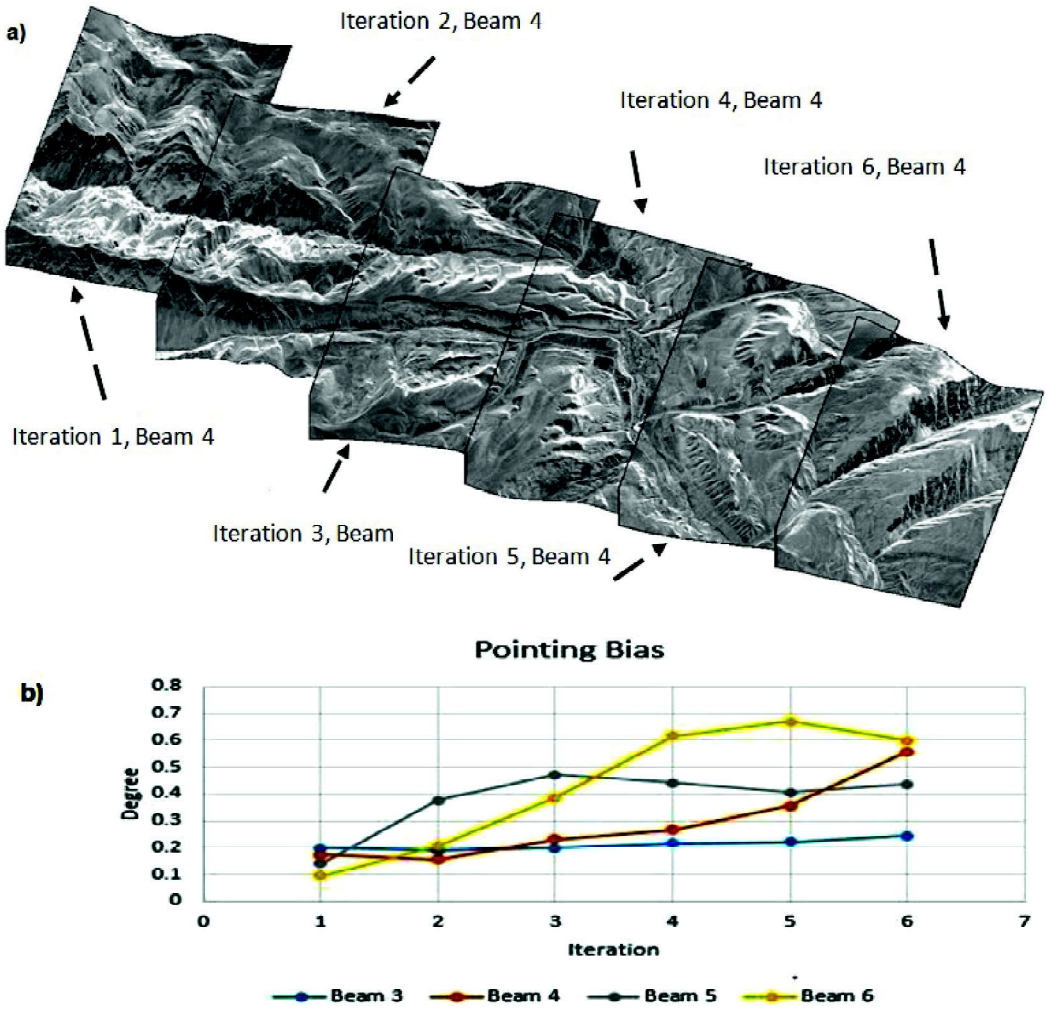

Fig. 7: (a) Multiple Iteration in multi beam imaging mode.
(b) Pointing Bias present in individual iteration of different beams (4) in multi beam acquisition

contains 70 percent of the power of the signal, it ensures the proper strength of the region. If the feeder element of the antenna suffers pointing bias due to system error or due to inaccurate calculation of SWST time for switching on the reception of signal, image may suffer radiometric degradation, due to imaging outside the 3db beam width of the signal. It is necessary to correct such errors in the system in the Initial Phase Operations for smooth functioning of the sensor. Also, it is mandatory to consider these values while extraction of elevation antenna patterns from the antenna model to provide seamless radiometry throughout the swath after radiometric normalization.

References

Alvarez-Pérez, J.L., Schwerdt, M., Bachmann, M. (2006). Terra SAR-X Antenna Pattern Estimation by Complex Treatment of Rain- forest Measurements. In Proceedings of the 26th International Geoscience and Remote Sensing Symposium, Denver, CO, USA.

Bachmann, M., Schwerdt, M. and Brautigam, B. (2010). TerraSAR-X Antenna Calibration and Monitoring Based on a Precise Antenna Model. IEEE Trans. Geosci. Remote Sens., 48, 690–701.

Doerry, A.W. (2006). Automatic Compensation of Antenna Beam Roll-off in SAR Images, Prepared by Sandia National Laboratories, SAND2006-2632.

Guarnieri, A.M. and D'Aria, D. (2003). Wide-angle azimuth antenna pattern estimation in SAR images. In *Proceedings of 2003 IEEE International Geoscience and Remote Sensing Symposium*, Toulouse, France, pp. 3105–3107.

Guarnieri, A.M. and Giudici, D. (2006). Accurate Estimate of the Azimuth Antenna Pattern from SAR Images. *In Proceedings of the 6th European Conference on Synthetic Aperture Radar* (EUSAR 2006), Dresden, Germany.

Gupta, M., Kartikeyan, B. and Chowdhary, S. (2014). An Approach to evaluate and monitor RISAT-1 SAR from level -0 raw data, *International Journal of Remote Sensing*, Vol. 35, No.16, 6043-6059, http://dx.doi.org/10.1080/01431161.2014.943323.

Huang, J., Chen J., Guo, Y. and Wang, P. (2022). Analysis and Correction of Antenna Pattern Effects in AMAO Spaceborne SAR Images" in Remote Sens, 14, 2141,https://doi.ord/10.3390/rs14092141.

Luscombe, A.P. and Thompson, A. (2001). "RADARSAT-2 calibration: proposed targets and techniques," in *Proceedings of IEEE International Geoscience and Remote Sensing Symposium* (IGARSS '01), Vol. 1, pp. 496–498, Sydney, Australia.

Schwerdt, M., Bräutigam, B., Bachmann, M., Döring, B., Schrank, D. and Gonzalez, J.H. (2010). Final TerraSAR-X Calibration Results Based on Novel Efficient Calibration Methods. IEEE IEEE Trans. Geosci. Remote Sens., 48, 677–689.

Shimada, M. (2011). Model-based polarimetric SAR calibration method using forest and surface scattering targets. In Proceedings of the 2011 IEEE International Geoscience and Remote Sensing Symposium, Vancouver, BC, Canada, pp. 3736–3739.

Walter, G. C. *Spotlight Synthetic Aperture Radar: Signal Processing Algorithms*. Arctech House Remote Sensing Library.

Zink, M. and Rosich, B. (2002). Antenna Elevation Pattern Estimation from Rain Forest Acquisitions, ENVISAT/ASAR Calibration Review (ECR) of ESTEC, European Space Agency (ESA), Noordwijk, Netherlands.

Indian Cartographer, Vol. 44, No. 1 & 2, pp. 49-54
ISSN: 0972-8392 © INCA, 2024

A Framework for Geo-spatial Analytics using Deep Learning

Vijender Busi Reddy*, **D. Sree Kiran, K. Raghavendra** and **D. Mallikarjuna Rao**
Advanced Data Processing Research Institute (ADRIN)
Department of Space, Govt. of India, Secunderabad (India)
*Corresponding Author's Email: vijender@adrin.res.in

Abstract

Speech recognition system and natural language processing technologies have gained significant importance in recent developments, leading to development of powerful voice-based interfaces, often called as Human Computer Interface (HCI). Voice is one among the top most multimedia element in HCI. Deep learning technology is popularly known for Speech Recognition and Target detection. With vast number of Earth observation satellites/payloads, huge volume of geo-spatial data is generated, and there is a need/surge for developing highly efficient HCI techniques towards automated target detections. Spatial data analytics require past and present information which will be stored in the database. Extraction of information from database without knowing the structure and query language is very difficult. In this paper, a framework for target analytics on remote sensing imagery is proposed. The framework is divided into five modules, viz. Target detection, Keyword detection in speech, Speech-to-text, text-to-query and Analytics. The proposed framework gives an end-to-end solution for extracting the information from the temporal geo-spatial data with 88% accuracy in keyword detection.

Keywords: Deep learning, satellite data, remote sensing, neural networks, speech recognition, analytics.

Introduction

Now-a-days Deep Learning technology has reached in to all domains such as Speech, medical, agriculture, etc. Many deep learning based target detection models are developed and evolved to improve the accuracy (Zhang et. al.). In general, geo-spatial data is vast in dimensions and volume, and with lots of temporal data. Since, the data is in large volumes, analysis on temporal data takes huge efforts and man power. Deep Learning models are giving the benefits of detecting the targets with higher accuracies on Geo-spatial data (Chen et. al., Geng et. al., Chen et. al., Liang et. al., Lyu et. al.). Region-based deep learning models (Zhao et. al.) are giving better performances on remote sensing data. Ren et. al.(2016) improved the region based technique by using CNN (Faster-RCNN). It is tested on MS COCO, PASCAL VOC 2007 and 2012 dataset and shown good accuracy. Some of the DL architectures such as Recurrent NN, convolutional NNs (CNNs), long short-term memory model, deep belief networks and deep auto-encoders have already been explored for Remote Sensing tasks. Remote sensing image covers large amount of area compare to still camera. Hence, Lots of targets may be detected. Analyzing large number of target detection results of all temporal data is very difficult even though a database is used to store all the targets.

Another main issue is to get the useful information from the database and query processing. Information extraction from the database requires proper query which will have standard syntax and semantics. User who has knowledge in the database and query languages can only extract the information from the database.

Speech recognition has become an essential part of a Human-Computer Interaction system with fast-growing technology (Bell et. al.). Speech based interactive applications should be able to process the human languages (Ochiai et. al.). Natural Language Processing (NLP) is the branch of AI that focuses on understanding the human computer interactions of human language. NLP combines computational, statistical, machine learning, rule-based modeling of human language and deep learning models. Speech recognition systems are providing better accuracies due to deep learning models. Speech systems recognize the speech and converts in to text. (Smali et al.) used Bayesian network for resolving the speech understanding problem. Authors used Bayesian network for classification with unsupervised learning.

Text to query generator is another technique to convert text to database understandable query. Database understand able query should follow systematic rules like syntax and semantics. This technique is very useful when user do not have knowledge on query languages. Xuanfeng et. al. designed a speech to SQL tool which converts human speech to a SQL query statement. It has an Automatic Speech Recognition (ASR) and text-to-SQL component. However, due to performance degradation in ASR, a new Network named Speech SQL Net (Xuanfeng et. al.) is proposed to directly translate human speech into SQL queries without an external ASR step. Speech SQL Net has tested on dataset named Speech SQL, by piggybacking the widely-used text-to-SQL datasets. Jose et.al. proposed transformer based language models to handle the sequences of text. However, Transformers give better accuracy for limited size of text and Training time is more.

In this paper, we propose a framework for extracting the information from the remote sensing data. The proposed methodology extracts the information from the geo-spatial data even though the user does not have any knowledge on database and query languages. A speech based method is proposed to extract the information and it is not limited to length of the input text. The image is very big such as 14000X64000 pixels. Targets are detected by applying the trained deep learning models and target information is stored in shape file and database. The data in the database is not only huge but also diversified. Extracting information from the diversified data is very complex task as user does not know about the data. So, queries should be generated for the specific database. The model used for inference is trained based on (Vijender et. al.). Since, remote sensing image is big, authors have divided the image into equal dimension of length before training and inference. Modified Faster-RCNN model is used for airplane detection. Authors have tested the model (Vijender et.al.) on different dimensions of images and shown the precision, recall and accuracy parameters as 0.93, 0.85 and 0.79 respectively and authors also shown that, model will work on multiple objects.

Deep Learning model inferences require lot of computational power. However, recent advancements in fabrication and hardware technology, many Edge devices are available with CPU+GPU capable of deploying Edge GPU clusters. This shift to Edge AI from high end servers/ cloud brings several key benefits including low power, latency, bandwidth and cost. Proposed method is a lightweight solution, can run on edge devices.

Methodological Framework

The aim of the methodological framework is to get the information from the database with minimal knowledge or no knowledge of DBMS (Database Management Systems). Proposed Framework uses Speech Recognition system which will take the input of a human voice and convert the speech into text then to query the database. By this, anyone can just obtain the results by just asking some question to the machine and the whole speech is converted into text and displayed the results.

Fig. 1 depicts the End-to-End framework which contain Ortho image generation to Result for Analysis. Proposed Framework is divided into Five modules, viz. Target detection, Keyword detection in speech, Speech-to-text, text-to-query and Query processing. It uses Deep learning techniques for target detection and speech recognition. This Framework works on embedded systems for geo-spatial analytics. Data Processing Server is not part of the proposed framework. However, It expects ortho images from the data processing server.

The following sections contain detailed explanation of each module.

Target detection using Deep Learning

Satellite data is processed in Data Processing server, which performs image processing operations and finally creates a geo-tagged ortho image. These ortho images are sent to AGX Xavier board for inference. The trained models, which are trained for the targets as per the details provided in Vijender et. al., are used to infer the geo-tagged ortho-images. The detected targets are stored in a shape file format. Since the data is very huge and the quantity information of the detections is also very high, inferred data will also be stored in the data base for further analysis. All the target detections are stored in a particular format defined by the database and this huge data increases from time to time due to day-to-day satellite data acquisitions. Extraction of the information from this huge amount of data is very challenging. The advantage of independent inference engine is that it does not use the data processing server resources.

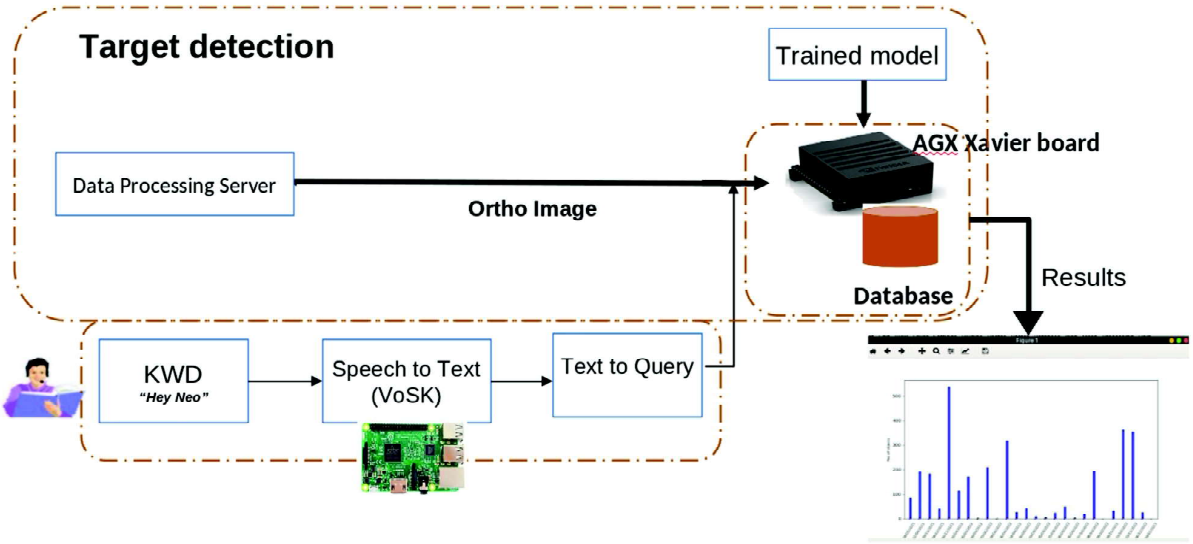

Fig. 1: End-End Framework

Speech to Text

In the digital world using voice command to operate a device is more appreciated and convenient compared to using mouse and keyboard. Speech recognition is a complex task as the accent depends on geo-graphical regions. Audio from the microphone is taken with the environmental noise. The model is trained with various noises so that model can recognize the voice even in presence of noise. The trained two models for this module Key do word detection and convert speech to Text. The system searches for the keyword in the voice such as "ok google" in the google speech recognition system. Proposed Keyword detection searches for "Hey neo" in the speech. Once the keyword is detected, the voice is captured up to 5 seconds pause. The captured voice is converted into text.

Text to Query

Querying a database is a difficult task, and can only be written by a person who has a background knowledge of the database. A person who does not have background knowledge of the database, it will be difficult to formulate a query and fetch results from the database. After converting the speech to text, text will be in natural language form. The text will be converted into a valid query form by using a sequence model so that the database can be queried. This task converts text into a structured representation form understandable by data base.

Query Processing

This module applies the query on database to get the formated results which will be used for analysis. The results shown in in pictorial and text form so that the user can perform better analysis.

Implementation

The developed and trained target detection models (Vijender et. al.) are loaded into an embedded board such as Tegra AGX xavier board (Fig. 2) (nvidia), which works

as an inference engine to identify the targets on temporal data. The embedded board is connected to satellite data processing (DP) system through network interface and the commands are triggered from DP system whenever the geo tagged ortho image is formed. The inference engine infers the image based on the parameters mentioned in the DP systems trigger. The inference results such as shape files and database are stored in the storage due to less storage in the embedded board.

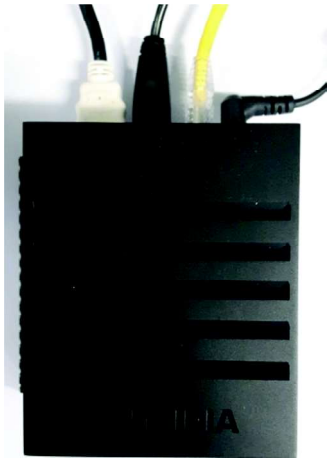

Fig. 2: Nvidia AGX xavier board

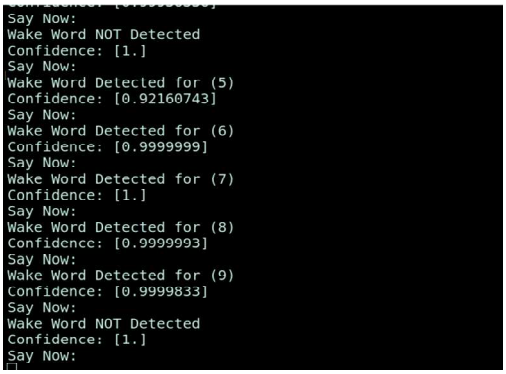

Fig. 3: Keyword detection

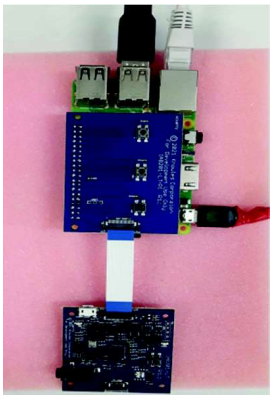

Fig. 4: Knowles board for Speech recognition

The key word detection submodule searches for 'Hey neo' word in the speech to activate the speech to Text module. The Keyword detection model works like a classifier and has 2 different classes, the class which has the wakeup word is labeled as 1 and the background sound with all the words other than the wakeup word is labeled as 0. The audio samples are recorded with both wakeup word and also for the background data. The audio samples are pre-processed for training. In pre-processing step, we read the audio data using librosa library (librosa) and calculates the Mel-frequency cepstral coefficients (MFCCs) of the audio data, then it is converted into data frame. A vanilla neural network model with three dense layers with 256 units, two drop out layers with 0.5 drop rate. RELU activation is used for intermediate layer and softmax for the output layer. The goal is to predict whether the input has wake up word or not. The prediction runs on audio samples collected from Micro phone with frequency 44100Hz. Trained model infer the audio samples and produces the binary output of the audio clip being a wakeup word or not. The sample testing of keyword "Hey Neo" detection is shown in Fig. 3.

The performance of wake up word accuracy is computed with number of correct predictions on total predictions. The experiment with 100 test samples of 'Hey Neo' word is repeated ten times and average is taken. The accuracy of wakeup word detection is computed as 88% which is quite good compared to (T. Ochiai et. al.). We tested other than the wakeup word but none of them are detected as wake up word. That means no false alarms.

After wake up word is detected Speech-to-Text module will be activated. It record the audio up to 5 seconds pause comes. Since, lots of training data is required for speech recognition model training, proposed method uses Vosk toolkit (Alpha Cephei) developed by Kaldi. It is a light weight, portable and popular speech recognition software with Word Error Rate 70% (Alpha Cephei). It provides pre-trained acoustic models that are trained on large amounts of speech data for different languages. These models serve as a starting point for speech recognition tasks and can be fine-tuned or adapted to specific domains or requirements. In this architecture, we have used Indian english models. Keyword detection and speech recognition softwares loaded into knowles board (Fig.4) which contain raspberry pi3 and some audio boards for collecting audio samples.

The Text to SQL query generation module includes several preprocessing steps. First, it converts natural language keywords into SQL-compatible terms. It also

removes stop words based on a configuration file, which includes common words like "about," "am," "in," and "on." Next, the module identifies entities and nouns, aligning the input sentence with existing columns and tables in the database. An entity-column dictionary is then created, which is essential for generating the SQL query. This lightweight module can operate on a Knowles board and generates standard SQL queries, eliminating the need for continuous training. The resulting SQL query is executed on the database, returning results in both visual and file formats.

The target detection database comprises data on airplanes, stored in JSON format, with fields including Name, Date, Airport, Location, and Airplane. Each row corresponds to a single Remote Sensing Image, built from approximately 30,000 images of Cartosat 2 series data using a target detection model. The database is populated solely through the framework; manual insert commands are not permitted. For example, when the input speech is "Hey Neo, how many airplanes present at Hyderabad Airport," Text to SQL module preprocesses the input to standardize terms - changing "Airplanes" to "Airplane" and identifying "Name" as the image name with the date. The intermediate output is transformed into: "Select Name and Airplane from DL in Hyderabad Airport". The final SQL query generated is:

SELECT Name, Airplane FROM DL WHERE Airport = 'Hyderabad';

Some standard inputs and corresponding outputs are:

(i) *Input:* "Hey Neo, how many airplanes are present at Hyderabad Airport from November 2019 to August 2020"

Output SQL query: SELECT Name, Airplane FROM DL WHERE Airport = 'Hyderabad';

The 'From' and 'To' dates will be used to filter the results of the SQL query.

(ii) *Input:* "Hey Neo, how many airplanes are present at Hyderabad Airport in January 2021"

Output SQL query: SELECT Name, Airplane FROM DL WHERE Airport = 'Hyderabad';

Month will be used to filter the results of the SQL query.

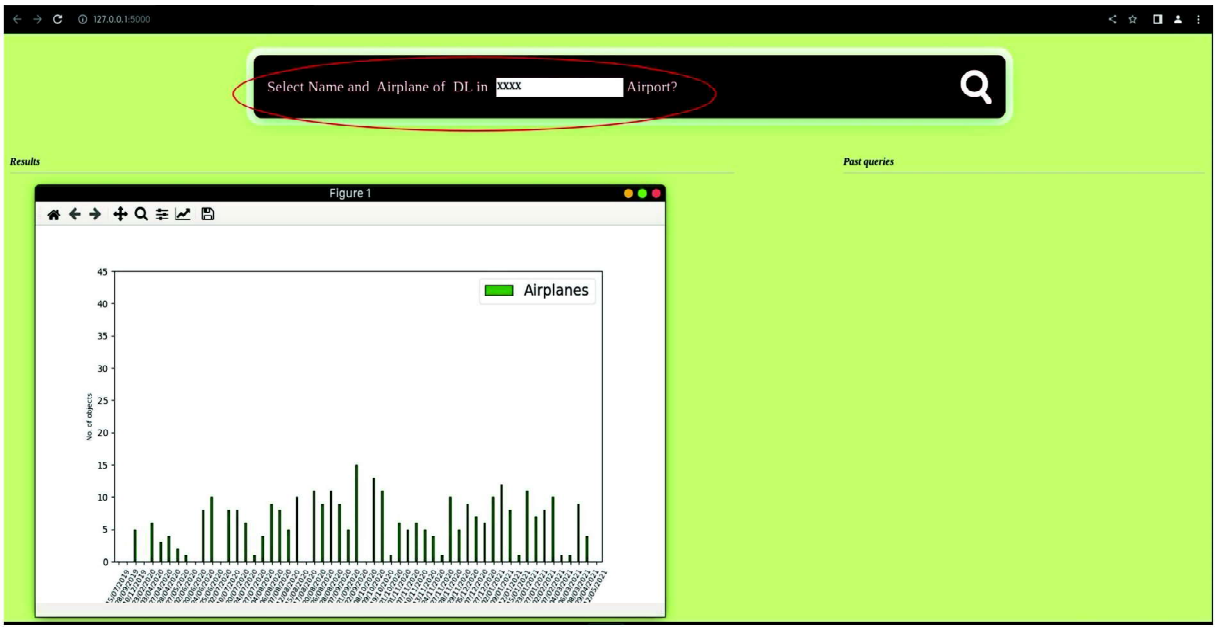

Fig. 5 : Output result screen

There are situations where the text-to-SQL module cannot generate a query due to missing keywords or incomplete input. For example, the input "Hey Neo, how many airplanes are present at Hyderabad" lacks the keyword "Airport", so the module is unable to create a corresponding SQL query.

Conclusion

In this paper, geo-spatial analytics architecture is presented. Spatial data is huge and diversified. So, it will be very difficult to extract information. The proposed solution is a voice and text based query mechanism for

users who do not have any knowledge on database queries. The testing and accuracies show that the proposed solution is performing well.

In future work, the models will be tested on Edge-based GPU cluster to improve the performance and reliability of the framework. The Edge-based GPU cluster contains multiple GPUs connected in master and slave configuration. Each module in the framework can be assigned as a job to a node in the GPU cluster.

References

Alpha Cephei, Vosk speech recognition library "https://alphacephei.com/vosk/".

Bell, P., Fainberg, J., Klejch, O., Li, J., Renals, S. and Swietojanski, P. (2021). Adaptation algorithms for neural network-based speech recognition: An overview. IEEE Open Journal of Signal Processing, 2:33–66.

Chen, Y., Lin, Z., Zhao, X., Wang, G. and Gu, Y. (2014). Deep learning-based classification of hyperspectral data. IEEE Jornal on Selected Topics in Appllied Earth Observation Remote Sensing, 7(6):2094–2107.

Chen, Y., Zhao, X. and Jia, X. (2015). Spectralspatial classification of hyperspectral data based on deep belief network. IEEE Jornal on Selected Topics Appllied Earth Observation and Remote Sensing, 8 No. 6:2381–2392.

Geng, J., Fan, J., Wang, H., Ma, X., Li, B. and Chen, F. (2015). High-resolution sar image classification via deep convolutional autoencoders. IEEE Trans. Geoscience Remote Sensing, 12 No.11:2351–2355.

Jetson, N. (2020). agxxavier developer kit, https://www.nvidia.com/en-in/autonomousmachines/embedded-systems/jetson-agx-xavier.

Jose, M.A. and Cozman, F.G. (2023). A multilingual translator to sql with database schema pruning to improve self-attention. In Int. j. inf. Tecnol.

Liang, H. and Li, Q. (2016). Hyperspectral imagery classification using sparse representations of convolutional neural network features. Remote sensing, 8(2):99.

Librosa. Librosa library, "https://librosa.org/doc/latest/index.html".

Lyu, H, Lu, H. and Mou, L. (2016). Learning a transferable change rule from a recurrent neural network for land cover change detection. Remote Sensing, 8(6):506.

Ochiai, T., Delcroix, M., Moriya, T., Sato, H. and Shinozaki, T. (2023). Streaming end-to-end target-speaker automatic speech recognition and activity detection. IEEE Access, 11:13906–13917.

Reddy, V.B., Kumar, P.K., Venkataraman, S. and Venkataraman, V.R. (2020). Real-time object detection in remote sensing images using deep learning. In International Conference on Advanced Machine Learning Technologies and Applications.

Ren, S., He, K., Girshick, R. and Sun, J. (2016). Faster r-cnn: Towards real-time object detection with region proposal networks. ariv:1506.01497v3 [cs.CV].

Smali, K., Jamoussi. S. and Haton. J.P. (2005). ROM speech to sql queries: A speech understanding system. In The Twentieth National Conference on Artificial Intelligence Workshop on Spoken Language Understanding,Pittsburg, United States.

Zhao, X., Jiang, D., Song, Y., Chi R. and Wong, W. (2022). Voicequerysystem: A voice-driven database querying system using natural language questions. SIGMOD '22: Proceedings of the 2022 International Conference on Management of Data, Philadelphia PA USA, pages 2385–2388.

Zhao, A., Fu, K., Sun, H., Sun, F., Li, Zhang, D. and Wang, H. (2017). An effective method based on acf for aircraft detection in remote sensing images. IEEE Geoscience Remote Sensing Letters, 14(5):744–748.

Zhang, F., Du, B. and Zhang, L. (2016). Scene classification via a gradient boosting random convolutional network framework. IEEE Trans on Geoscience and Remote Sensing, 54 No. 3:1793–1802.

Indian Cartographer, Vol. 44, No. 1 & 2, pp. 55-62
ISSN: 0972-8392 © INCA, 2024

Study of High-Resolution Satellite Data and 2D/3D Resistivity Tomograms for Investigating Buried Archaeological Sites in parts of Rajasthan

Ashish Kumar Jain* and **Hansraj Meena**
Regional Remote Sensing Centre-West, NRSC (ISRO), Jodhpur (India)
** Corresponding Author's email: ashish.jain@nrsc.gov.in*

Abstract

Archaeological mounds represent the architecture of any civilized society of the ancient history. These mounds are mostly composed of earthen materials such as mud bricks and pottery shreds that give a significant color and surface texture to the soil. However, they are generally found to be buried under the cover of recent sediments. Systemic excavation of archaeological sites helps us to know the progressive evolution of human development and cultural civilization. Geospatial technology plays a significant role for detection of these mound sites over a large area. This study illustrates a unique and innovative approach to detect the archaeological mounds in Hanumangarh and Sri Ganganagar districts of Rajasthan by using remote sensing data and GIS approach. As these mounds have close association with various available thematic datasets such as, Land Use Land Cover (LULC), Settlement, Palaeo channel, etc., Archaeological Survey of India (ASI) known sites such as Kalibanga, Munda, etc. have been investigated to characterize a mound feature in the context of these thematic datasets. A GIS model has been developed to incorporate these characteristics of mound on input LULC layer. The model has been used to identify probable archaeological mound features in the study area. Further, these mounds have been filtered by making visualization on high resolution satellite images. A ground survey has also been conducted to validate some of the discovered sites in Hanumangarh district. Electrical resistivity tomography (ERT) is a geophysical technique for imaging sub-surface structures from electrical resistivity measurements made at the surface, or by electrodes in one or more boreholes. Archaeological features can be mapped when they are of higher or lower resistivity than their surroundings. High-Resolution Electrical Resistivity Tomography (HERT) survey has been conducted at ASI known sites of Kalibangan for depiction of subsurface structures and features in terms of variation of resistivity. The results are the tomograms showing exact locations of the buried well, wall and kiln at 1-5m depth.

Keywords: Archaeological Mounds, DEM, High-Resolution Electrical Resistivity Tomography.

Introduction

A tell or mound is an artificial topographical feature consisting of the accumulated and stratified debris indicating remains of a city or village, built and rebuilt at the same site for thousands of years. Archaeological remnants represent the architecture of any civilized society of the ancient India. Archaeological mounds are generally prominent or bold traces of past human settlements on sedimentary terrains or arid, semi-arid regions inhabited by once-lived ancient civilizations. These mounds are mostly composed of earthen materials such as mud bricks and pottery shreds that give a significant color and surface texture to the soil. However,

they are generally found to be buried under the cover of recent sediments. Systemic excavation of archaeological sites helps us to know the progressive evolution of human development and cultural civilization. Archaeological Society of India (ASI) is mainly responsible for excavation and protection of archaeological sites. But, still many of the sites remained unexplored in different parts of the country due to lack of scientific investigation. Hence, there is a need to unearth the archaeological mounds along with their fortified sub-surface structures of walls using high-resolution satellite images and geophysical measurements.

Geospatial technology has been implemented on remote sensing images to detect and map archaeological mounds by many researchers. The use of remote sensing images and geographic information system (GIS) platform to identify archaeological features has been demonstrated (Praveen G. Deshbhandari et al., 2023). An innovative multisensory, multi-temporal and machine-learning approach using remote sensing big data has been used for the detection of archaeological mounds in the Cholistan desert (Orengo et al., 2020). A virtual survey of archaeological sites has been carried out by means of detecting and mapping the ancient settlement mounds (tells) by using the SRTM three-arc second terrain model (Menze et al., 2006). Deep convolutional neural network (CNN) technique has been ued for the automatic detection of stone mounds from high-resolution satellite images in four regions in the Altai Mountains (Chen et al., 2021).A deep learning model is presented for detection of mounded archaeological sites in Mesopotamian flood-plain (Luca Casini et al., 2023). They illustrated the results obtained by using pre-trained semantic segmentation deep learning models. Marco Fiorucci et al. (2022) introduced two novel automatic evaluation measures, designed to encode the salient aspects of the archaeologists' thinking process. Abraham Resler et al (2021) presented an account of a metric learning-based convolution neural network (CNN) applied to an archaeological dataset. They used several thousand artifact images, ranging from the Lower Palaeolithic period to the late Islamic period to train the model. The method presented by Kelsey M. Reese (2021) offers an introduction to the application of deep learning artificial neural networks to archaeological site assemblages. Artificial neural network has been introduced as a computational tool to utilize legacy archaeological data for precisely and accurately estimating dates of residential site occupation. Tapete et al. (2021) used high resolution imaging capability Synthetic Aperture Radar (SAR) constellation in his study to generate DEM products of enhanced resolution to undertake a systematic mapping of tells and archaeological deposits. Trier et al. (2015) worked in describing a processing chain for the semiautomatic mapping of grave mounds from airborne laser scanning (ALS) data. Davis et al.(2019) demonstrated semi-automatic Object-based image analysis using lidar data can provide a significant source of information about pre-contact landscapes in heavily vegetated areas.

High resolution Electrical Resistivity Tomography (HERT) is one of the non-destructive techniques to get subsurface ground data at deep levels. The purpose of electrical surveys is to determine the subsurface resistivity distribution by making measurements on the ground surface. Various electrical array configurations like Wenner-Schlumberer (WS), Pole-Dipole, Pole-Pole etc. may be applied in field for making observations. These array configurations show different sensitivity to various geological features and materials. Based on the geological features, shape and material, different electrical arrays are implemented which provide different depth of investigation also. The distance between two electrodes may also be varied to get different resolution of 2D tomograms. HERT measurement is one the most suitable method for exploration of subsurface archaeological features because of its non-invasive approach to ground objects. Zhao Wenke et al. (2018) carried out both the 2-D and 3-D resistivity imaging to get a clear evidence of structural details of the burial mounds.

Study Area

Hanumangarh district is positioned in the northernmost part of Rajasthan (Fig. 1). It is surrounded by the state of Punjab in the north, the state of Haryana in the east, the districts of Bikaner and Sri Ganganagar in the west, and Churu district in the South. It extends between $28^0 46' 25.07''$ to $29^0 57' 26.90''$ north latitude and $73^0 47' 41.74''$ to $75^0 31' 58.70''$ east longitude. It covers an area of about 9,656 square kilometer. The district is a part of Thar desert and is covered by thick layer of alluvium and aeolian sand. Generally sand dunes have variations of 4 to 5 m in height (CGWB report, 2013). Sri Ganganagar district is also situated in the northern most part of Rajasthan. It reaches out from $28^0 42' 30''$ to $30^0 12' 00''$ north latitude and $72^0 39' 15''$ to $74^0 18' 30''$ east longitude.

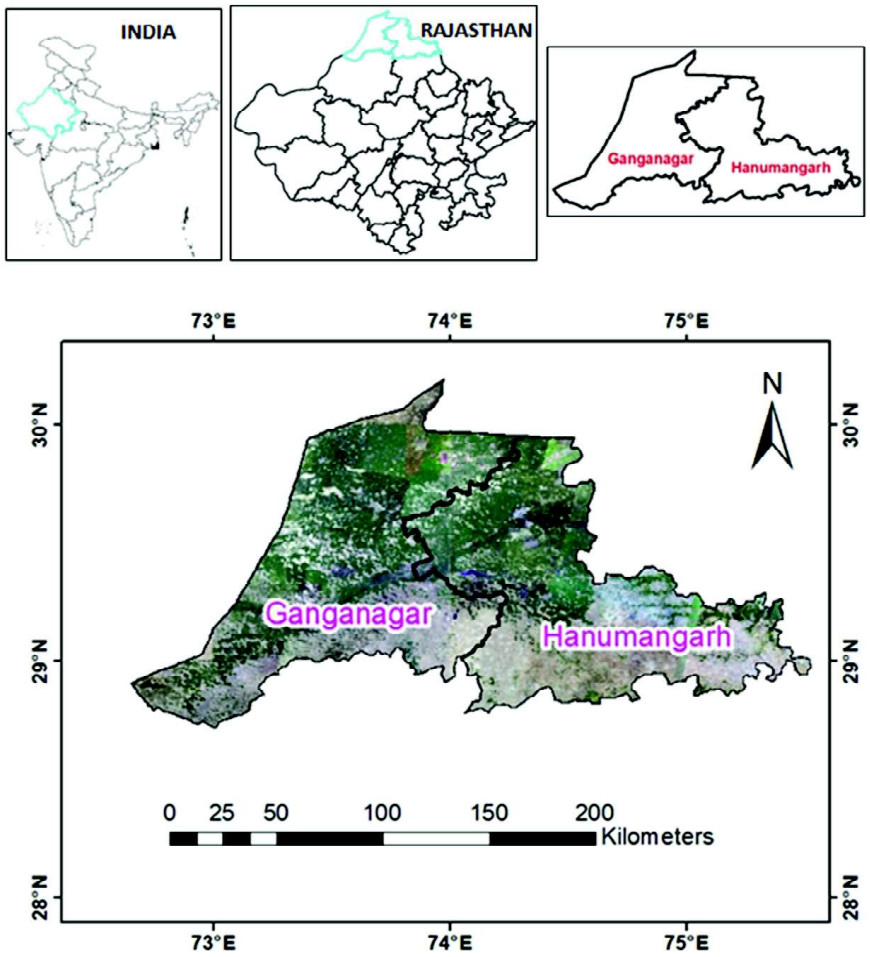

Fig. 1: Location map of Hanumangarh and Ganganagar districts on LISS-IV Cartosat-1 Merged (2016) image

Materials and Methods

Datasets used

Land use / Land cover map (LULC map)

LULC maps provide information regarding utilization of land in various aspects and these also play a vital role in the creation and implementation of development programs and policies required for development and sustainable growth of the land. In this study, Land use / Land cover (LULC) data of Hanumangarh and Sri Ganganagar districts at 1: 10,000 scale (source: Bhuvan) is used as a base layer. Land cover class of archaeological mounds is mapped in open and sparse scrub land class in LULC map.

Digital Elevation Model (DEM)

Archaeological mounds exist on undulating terrain land surfaces which can be characterized using DEM data. The Cartosat-1 Digital Elevation Model (CartoDEM) is a National DEM developed by the Indian Space Research Organization (ISRO). It is derived from the Cartosat-1 stereo pair images launched in May 2005. Carto DEM tiles with 30m posting at equator are freely available on ISRO Bhoonidhi portal. For our current research purpose, Carto DEM tiles of the study area have been downloaded. We mosaicked all Carto DEM tiles covering both Hanumangarh and Sri Ganganagar district.

Palaeo Channel

In ancient times, most of the civilizations were flourished near river banks where sufficient water sources were available. Many rivers, which were flowing in the past, \ have now disappeared completely or fully buried due to some natural, tectonic as well as anthropogenic disturbances. Traces of any palaeochannels nearby are strong indicator of probable sites for mounds.The palaeo channels layer used in this study is generated based on Saraswati palaeo channels data available on ISRO Bhuvan Portal.

Settlement

Archaeological mounds are remnants of past human settlements inhabited by once-lived ancient civilizations. Hence these mounds have close association with existing village settlements. Settlement data has also been used to characterize a mound. In this study, settlement data has been generated based on settlement layer available at ISRO Bhuvan Panchayat Portal.

Methodology

Archaeological mounds have been characterized in terms of various thematic layers viz. LULC, Palaeo channel, Settlement and DEM by using all ASI known mound sites. All known archaeological mounds are mapped in open and sparse scrub land class in LULC map. These mounds are located within buffer boundary of 2 km of existing Settlement and buffer boundary of 5 km of Palaeo channels. The area covered by the mounds has the height variations with 5m or more. The area covered by a single mound is less than or equal to 40 hectares. The methodology has been developed as shown in Figure 2 to implement these conditions. A GIS model has been developed to implement the methodology. Finally, all the detected mound sites are visually checked on high resolution imageries and false mound sites have been removed.

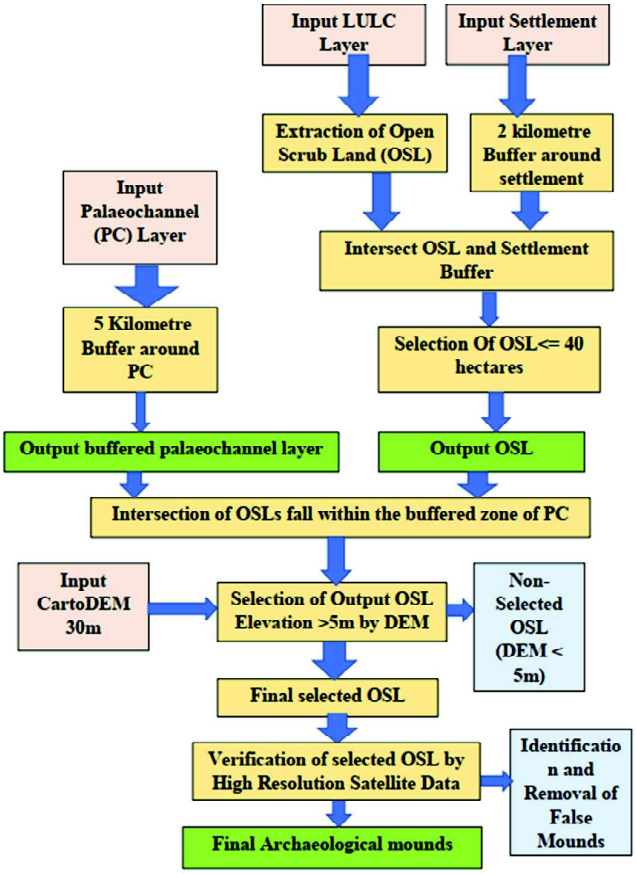

Fig. 2: Methodology Flow Chart

The methodology uses land use land cover mapped at 1: 10000 scale as an input. Hence it is not able to detect small mounds less than 0.1 hectare. Besides this, some of the mound features are converted to agriculture land or industrial land which is also not detectable by using this method. It is also necessary to perform HERT survey in clean atmosphere avoiding any rainfall or natural calamity. The resistivity instrument should be properly calibrated before using it in the field. Resistivity check operation is performed for each electrode to check the wire connections in proper condition. The equipment is not able to detect small size objects (<1m) buried under ground surface. Similarly, electrode spacing should be kept minimum to collect highly dense data points and to increase accuracy of 2D tomograms.

Results and Discussion

The developed GIS model was run by providing inputs of LULC, Palaeo channel layer, Settlement layers and mosaic of Carto DEM. By running the GIS model, we extracted total 912 features fulfilling all criteria. These features are manually inspected on high resolution image and we extracted total 177 features as possible mounds showing red colored tone on the image. The accuracy of GIS model totally depends on accuracy of LULC data. In total 177 features have been finalized as mounds after applying all criterions of the methodology. These features are shown with overlay of LISS-IV Cartosat-1 Merged (2016) image as shown in Fig. 3(a). The merging of LISS-IV & Cartosat-1 images provides 2.5m spatial resolution multi-spectral images. A zoomed in view of marked red circle is shown in Fig. 3(b), where polygons of mound features are shown. Based on model output, few unknown sites (Villages of Dabli Rathan, Lakhuwali, and Karnimata temple in Hanumangarh district) have been inspected and verified at field. The unknown mound sites are identified as true mounds as these were also covered by broken pieces of pottery shreds of red and black color, burnt bricks of various sizes and partially exposed brick as shown in Fig. 4. These mounds are easily identified on land surfaces as elevated zones covered by pottery shreds mixed with mud bricks as shown in Fig. 4(a) to 4(d).The entire list of detected mounds with latitude and longitude has been shared with ASI for further validation and investigation.

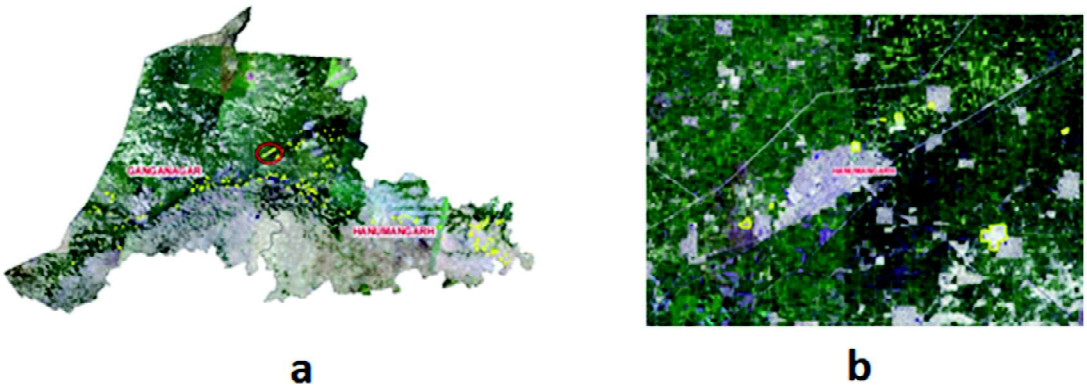

Fig. 3: (a) Detected mounds shown in yellow color on LISS-IV Cartosat-1 Merged (2016) image
(b) Zoomed in view of red zone marked in (a), showing mounds near to Hanumangarh town

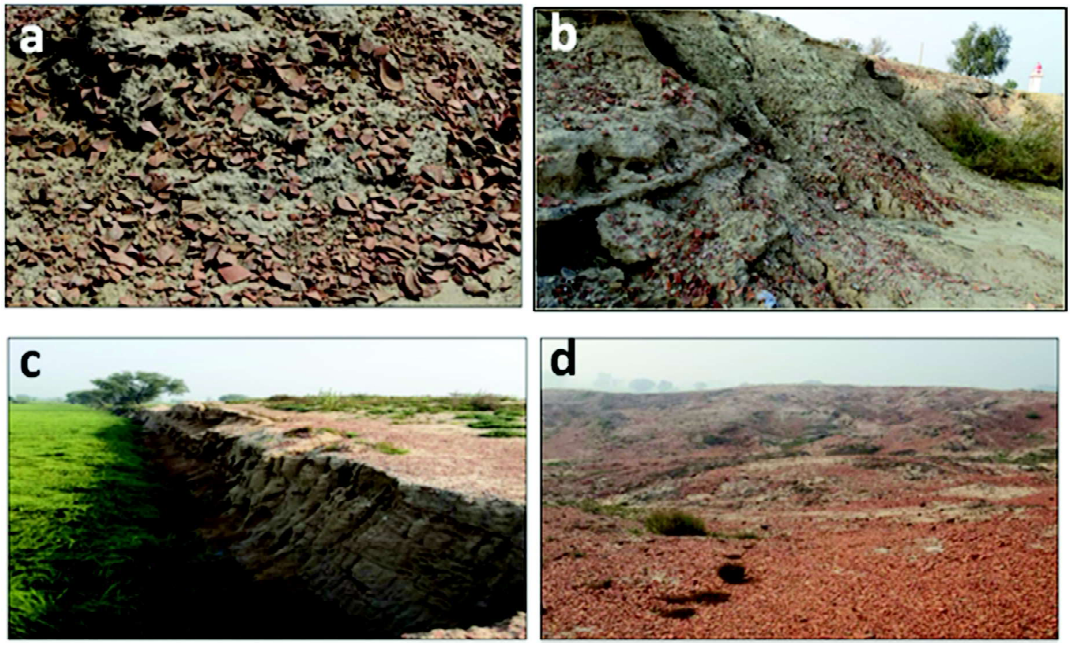

Fig. 4: (a) & (b) Field photographs of Karnimata Temple unknown mound site
(c) Field photograph of Lakhuwali unknown mound site (d) Field photograph of Dabli Rathan unknown mound site.

High resolution electrical resistivity survey has been conducted at Kalibangan (ASI known site) with prior permission from ASI for extraction of subsurface features. The IRIS Pro 72 of 10 channels was used for High resolution resistivity survey and it has been carried out for collecting data at well, fortified wall and kiln area locations by using Wenner-Schlumberer (WS) and Dipole-Dipole array configuration of 5m electrode spacing for the total length of 55m. The well location was excavated by ASI in earlier times and it has been covered by ASI for protection of the site. The array configuration was programmed using Electro Pro software and inserted into the instrument. After performing the survey, data was downloaded using Prosys software and data inversion process was completed using RES2D Inv software. 2D resistivity tomogram was generated by using inversion process. The tomogram in Fig. 5 represents subsurface resistivity data across the well location up to 12.5 m depth. The tomogram shows high resistivity zone in middle of top surface layer up to 5m depth and having width less than 5m. The depth position and dimensions of the well match with ASI records. This zone shows the existence of material having high resistivity range from 74.0 to 131 Ωm used for construction of buried well. The material used for construction of the well is burnt mud bricks made by clay material (terracotta). The resistivity values of clay material also fall in the same range. Hence, HERT survey is able to identify high resistivity zone corresponding to material of the structure. This zone is surrounded by two low resistivity zones from 4.34 to 13.5 Ωm which represents existence of alluvium material.

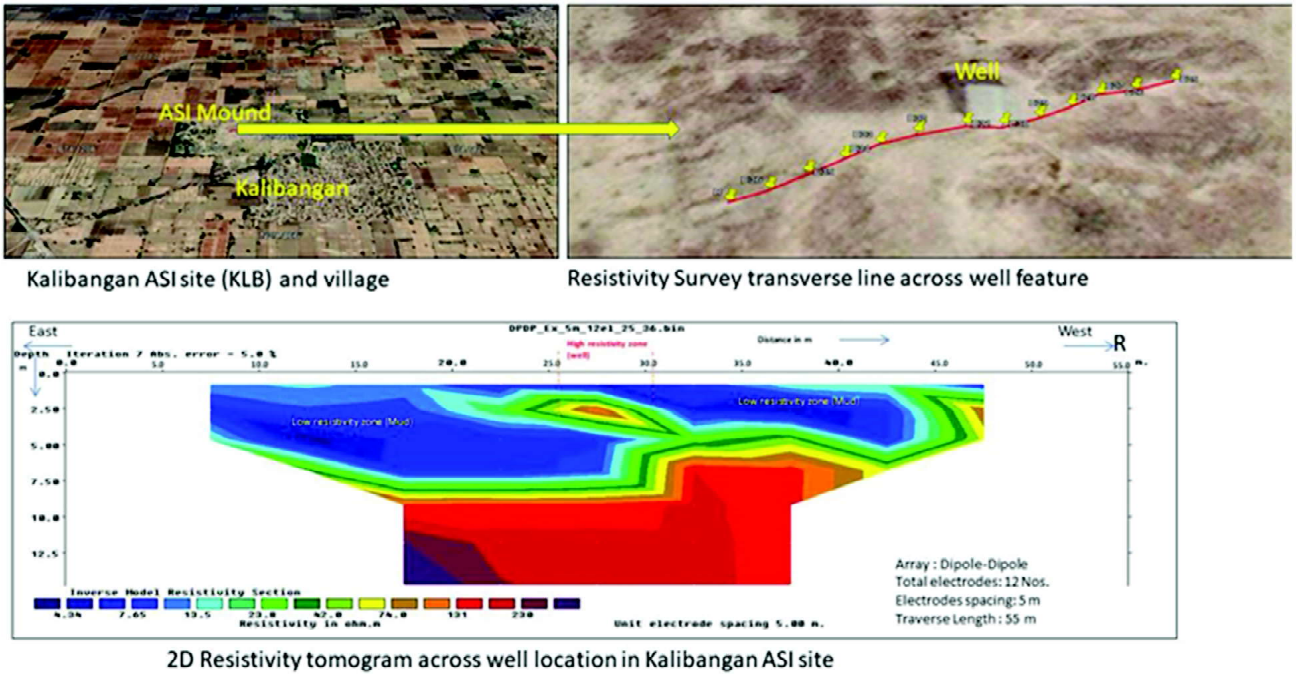

Kalibangan ASI site (KLB) and village

Resistivity Survey transverse line across well feature

2D Resistivity tomogram across well location in Kalibangan ASI site

Fig. 5: Kalibangan ASI site and adjoining village shown on high resolution image, laying of electrical cable with 5m electrode spacing and 2D tomogram showing well structure below ground surface

Conclusion

Archaeological mounds are readily visible due to their prominence and shape, and the fact that they are composed of accumulated debris of earthen materials such as mud bricks and pottery shreds, which create distinguishing color and surface texture over the soil surface. In this project, Archaeological Survey of India (ASI) known sites have been investigated to characterize mound in context of various thematic layers viz. LULC, Settlement, Palaeo channels and DEM. A GIS model has been developed to incorporate the mound characteristics in GIS environment. Further, these mounds have been filtered by making visualization on high resolution satellite images. Few unknown sites (Villages of Dabli Rathan, Lakhuwali, and Karnimata temple in Hanumangarh district) have been inspected and verified. The unknown mound sites are identified as true mounds as these are

covered by broken pieces of pottery shreds of red and black color, burnt bricks of various sizes and partially exposed brick which strongly points the existence of an ancient settlement in past periods.

The High-resolution Electrical Resistivity Tomography (HERT) survey has been carried out on archaeological mounds of Kalibanga site to detect size and location of well, kiln and fortified wall. The similar exercise may be performed to detect buried objects in unexcavated archaeological mounds. The methodology developed in this project may be used to scale up in arid and semi-arid regions of North-West India with the help of line departments and other stakeholders to rejuvenate ancient Indus river civilization (pre / post Harappan) through development of geo-heritage sites and also to address the availability of drinking water issues. Similarly, machine learning approach with Random Forest Classification may be implemented on cloud platform like Google Earth Engine to process multi-temporal data. Moreover, microwave satellite images may be used with its distinct ability to identify high moisture zone and particular surface features. The unknown mound sites have reddish signature of broken pottery shreds similar to ASI known sites. Hence, carbon dating of these pottery shreds at unknown sites may be executed to determine the age of organic material to establish a link with old Indus Valley Civilization. As excavation of archaeological sites is linked with old civilization and culture, it needs immense care to protect old objects found on these sites. HERT survey may be most suitable to detect buried objects with maintaining its properties and characteristics. Remote sensing also plays a major role to cover the large area with its synoptic view capability. Hence, potential of both remote sensing and HERT survey may be utilized to detect unknown archaeological site and its sub-surface structures with non-destructive technique.

References

Abraham Resler, ReuvenYeshurun, Filipe Natalio & Raja Giryes (2021). A deep-learning model for predictive archaeology and archaeological community detection.Humanities and Social Sciences Communications |. https://doi.org/10.1057/s41599-021-00970-z.

Casini Luca, NicolòMarchetti, Andrea Montanucci ,ValentinaOrrù & Marco Roccetti (2023). A human-AI collaboration workflow for archaeological sites detection. Scientific reports, https://doi.org/10.1038/s41598-023-36015-5.

CGWB Report (2013). Groundwater Scenario, Hanumangarh district, Rajasthan.

Chen Fen, Zhou Rui, Van de Voorde Tim, Chen Xingzhuang et al. (2021). Automatic detection of burial mounds (kurgans) in the Altai Mountains, 0924-2716/© 2021. International Society for Photogrammetry and Remote Sensing, Inc. (ISPRS).

Deshbhandari Praveen G., ShettyAteeth. (2024). Archaeological Investigations of Honnavar Fort in Uttara Kannada District of Karnataka, India Using Geospatial Technology. J of the Indian Society of Remote Sensing,52(5):1031–1043. https://doi.org/10.1007/s12524-024-01855-9.

Dylan S. Davis, Matthew C. Sanger & Carl P. Lipo. (2019). Automated mound detection using lidar and object-based image analysis in Beaufort County,South Carolina. Southeastern Archaeology. https://doi.org/10.1080/0734578X.2018.1482186.

Kelsey M. Reese (2021). Deep learning artificial neural networks for non-destructive archaeological sitedating.Journal of Archaeological Science. https://doi.org/10.1016/j.jas.2021.105413

Marco Fiorucci,Wouter B. Verschoof-van der Vaart, Paolo Soleni , Bertrand Le Sauxand Arianna Traviglia. (2022). Deep Learning for Archaeological Object Detection on LiDAR: New Evaluation Measures and Insights.. https://doi.org/10.3390/rs14071694

Menze, B.H., Ur, J.A. and Sherratt, A.G. (2006). Detection of Ancient Settlement Mounds: Archaeological Survey Based on the SRTM Terrain Model.Photogrammetric Engineering & Remote Sensing Vol. 72, No. 3, March 2006, pp. 321–327

Orengo, H.A., Conesa, F.C., Garcia-Molsosa, A., Lobo, A., Green, A.S., Madella, M., Petrie, C.A. (2020). Automated detection of archaeological mounds using machine learning classification of multisensor and multitemporal satellite data.PNAS 117, 18240–18250.

Tapete Deodato, Traviglia Arianna, Delpozzo Eleonora, Cigna Francesca. (2021). Regional-Scale Systematic Mapping of Archaeological Mounds and Detection of Looting Using COSMO-SkyMed High Resolution DEM and Satellite Imagery. Remote Sens. 2021, 13, 3106.https://doi.org/10.3390/rs13163106

Trier Oivind Due, Zortea Maciel, Tonning Christer. (2015). Automatic detection of mound structures in airborne laser scanning data. Journal of Archaeological Science: Reports. http://dx.doi.org/10.1016/j.jasrep.2015.01.005

Zhaoa Wenke, Tiana Gang, Linb Qiang, Wangb Xing, Wanga Yimin, Bie Kang. (2018). Integrated characterization of ancient burial mounds using ERT and limited drillings at the Hepu Han Tombs, in coastal area of Southern China. Journal of Archaeological Science: Reports 23 (2019) 617–625. https://doi.org/10.1016/j.jasrep.2018.11.016.

Acknowledgements

Field Data used in this study are collected as part of the Technology Development Projects (TDP) funded by Indian Space Research Organization, Government of India. Authors thank to Director, NRSC for encouragement and support. The authors wish to acknowledge ASI Officials from ASI Circle, Jodhpur for their continuous support and help to carry out this study.

Indian Cartographer, Vol. 44, No. 1 & 2, pp. 63-69
ISSN: 0972-8392 © INCA, 2024

Disease Detection in Rice Plant using Artificial Intelligence

Arati Paul[1]*, Sanskar Goel[2] and **Suparn Pathak[1]**
[1]Regional Remote Sensing Centre - East, NRSC (ISRO), Kolkata (India)
[2]ECE Department, Amity University, Kolkata (India)
**Corresponding Author: aratipaul@yahoo.com*

Abstract

India is a leading producer of rice that contributes a lot to its economic growth. Disease is one of the leading factors that affect the growth and production of rice. Therefore, healthy growth and production of the rice plants is very much essential. Hence, rice plant disease needs to be detected well in advance so that the required treatment can be applied. In India most of the farmers are not that equipped with basic education in this respect. Even for an educated farmer, correctly identifying the paddy crop disease is not an easy task. Manual detection of these diseases costs a large amount of time, money, and human resources, and requires the farmer to take external help from a professional, who could guide them with the right treatment for their distinct plant's specific issues. In case of large farms, the manual detection process becomes lengthy and expensive. Thus, there is a sure need of a more independent, fast, and automated system, that can help the farmers in detecting the disease that their rice crops are suffering from, in a quick succession of time and at a comparatively less price. Hence, in the present work an Artificial Intelligence (AI) enabled rice plant disease detection system is developed that works on a smart phone. A Deep Convolutional Neural Network (DCNN) is trained using various images of disease affected rice leaves. After successful training and testing, the trained model is deployed into an android application, which would perform complete on-device processing to detect the rice plant diseases. The proposed system provides around 96% accuracy on the test dataset. The smart phone-based system would be easily accessible to the farmers and would help them predict the disease in just one click and thus will save their time, money and effort.

Keywords: Paddy; disease; artificial intelligence; rice plant; deep learning.

Introduction

Disease is one of the leading factors that affect the growth and production of rice. Diseases in rice or paddy cause a large quantity of loss in the grain yield. India is both the leading producer and consumer of rice. Rice production contributes a lot to the economic growth of the nation, and it is a part of the staple diet of majority of the population. India is the second-largest producer of rice in the world after China. The major 5 states in rice production in the country include West Bengal, Uttar Pradesh, Andhra Pradesh, Punjab, and Tamil Nadu. More than one-third of the world's population and more than half of India's population depend on rice as their primary source of nourishment (Statista, 2023). With more advanced ways that are being introduced, the main motive is to increase the production rates to even for higher numbers. But one aspect that the farmers are still struggling with, is the timely identification of the paddy disease, such that they can save their crop from getting destroyed. Every hour that passes due to the conventional method of identifying the disease, matters a lot. In several rice-growing ecosystems in the tropical and temperate regions of the world, illnesses continue to be a puzzling issue among the various biotic variables, limiting rice output and productivity.

Thus, to ensure healthy and proper growth and production of paddy, it is very much essential to detect the disease that the rice crop is suffering from, well in advance so that required treatment can be done. There are more than 20 different diseases in paddy that have been detected so far and every disease has a different treatment and way to cure. Therefore, identifying the disease the paddy crop is suffering from, is not an easy task. Manual detection of these diseases costs a large amount of time, money, and human resources. Additionally, farmers are required to take external help from professionals, who would guide them with the right treatment for their plant's specific issues. If in case there is a huge land area of a farm, then the manual detection process gets even more time taking and expensive. Thus, there is a sure need of a more independent, fast, and automated system, that can help the farmers in detecting the disease that their rice crops are suffering from, in a quick succession of time and at a comparatively less price.

One device that has made it possible to reach even into the most distant places, that has reached even to the most remote area, is a smartphone. A smartphone has been able to make its worth count to people of all professions, ideologies, and beliefs and something that has gone into the hands of people belonging to all strata, irrespective of their financial position. Whether it is a rural area or a well-developed city, low-cost smartphones are affordable by everyone because of the technological advancement. When smartphones have been able to creep so deep into the hands of everyone, everywhere, one should be taking the best use out of them. Machine Learning (ML) has been able to find its application in almost all issues and obstacles that humans are facing (Paul et al., 2022, Paul et al. 2023a), then why not try to use this artificial intelligence to solve the problems of the agricultural sector, a very important part of our society. The enormous variations in shape, size, texture, color, backdrop, layout, and imaging illumination of plant diseases in a real-world natural environment make identification challenging. The convolutional neural network (CNN)-based methods are most often used for classification of plant diseases because of CNN's excellent feature extraction capabilities (Kanjilal and Paul, 2023). Many researchers made advantage of CNN's potent feature extraction capabilities in the early studies on deep learning-based methods for classifying plant diseases and pests. These techniques were then integrated with conventional classifiers (Paul et al., 2018). Before using a traditional machine learning classifier for classification, the images are first fed into a pretrained CNN network to get image characterization attributes. The trials utilizing support vector machine (SVM) classifiers with various kernels and feature descriptors, verified the efficacy of the approach. Hence, a convolutional neural network architecture is utilized to extract the characteristics of images.

Ahmed et al. (2019) used different machine learning algorithms including that of K-Nearest Neighbor (KNN), Decision Tree, Naive Bayes and Logistic Regression for detecting rice plant diseases. Wang et al. (2021) proposed ADSNN-BO model on the Huy Do (2019) Rice diseases image dataset. They also tested VGG16, ResNet50, DenseNet121, MobileNetV1, Inception V3, and Xception model. Sreejith et al. (2022) performed detection by developing an enriched neutrosophic C-means (ENCM) clustering. Prajapati et al. (2017) applied Support Vector Machine (SVM) for disease recognition on segmented image. Anandhan and Singh (2021) performed the classification using Faster R-CNN algorithm. For disease classification, a fully connected layer followed by a SoftMax layer was placed as the last layer of the CNN model to classify the plant disease by Upadhyay et al. (2022). Five network structures viz. ResNet, DenseNet, SENet, ResNeXt, and ResNeSt were selected and tested by Deng et al. (2021). Ensemble learning was carried out by combining the three best network sub models out of the five sub models. Shrivastava et al. (2019) used AlexNet for features extraction and SVM for classification. Feature descriptor viz. Kurtosis, skewness, cluster prominence, Local Binary Patterns (LBP), Histograms of Oriented Gradient (HOG), cluster shade and gray level co-occurrence matrix (GLCM) texture are used followed by classification by ML algorithms viz. SVM etc. in some of the studies (Rumy et al., 2021; Saha & Ahsan, 2021; Shah et al., 2016; Pothen & Pai, 2020; Dutta et al., 2021; Khan et al., 2022). Inception ResNetV2 was applied by Krishnamoorthy et al. (2021) whereas Joshi et al. (2022) used CNN for the classification.

When an ML model is implemented into a mobile application, the app is loaded with the model's learnt parameters. The app does not need to communicate with a server to produce a prediction because it performs all inference computations locally on the device. The primary justification for performing inference directly on the device is speed. The prediction occurs instantly with on-device inference of ML models rather than requiring the user to send a request over the internet and wait for a response. Hence the proposed solution to the problem of

rice leaf disease identification and classification is implemented through a smartphone application. The ML model is trained by using various images of disease affected rice leaves including heathy leaves. After successful training, the trained model is deployed into an android application, which would perform complete on-device processing for identifying the disease from an input image of rice leaf. The Mobile Net Large V3 architecture is used to obtain high accuracy in disease detection task using smart phone. The main motivation of developing a mobile application is to make the prediction model easily accessible to the farmers and to help them predict the disease in just one click and thus saving a lot of their time, money, and effort. The subsequent sections of this article describe the present work and its outcome in details.

Materials and Methods

Data Base

The present work has been carried out using 'Rice Leaf's 5 diseases' dataset of 'Kaggle' created and formulated by Ade Fiqri (2023). The dataset comprises of a total of 2710 images in jpeg format. All the 2710 images have been divided into two categories, namely train and validation. The train folder has the images that would be used for training the deep neural network and the validation folder has images to validate/ test the predictions made by the trained model. Both the train and validation folders have six sub-categories each. The 6 sub-categories basically comprise of the different disease names and are as follows – Bacterial Leaf Blight, Leaf Blast, Leaf Scald, Narrow Brown Spot, Brown Spot and the last one holding the images of healthy paddy leaves. All the images have a dimension of 1600 X 1600 with a whitish background of different tone. Sample images from each category are shown in Fig. 1, whereas Table 2 presents the number of training and testing samples used in the present work.

Methodology

The overall methodology involves two major steps: (i) development of the deep learning model, and (ii) development of the android application. Fig. 2 represents the entire workflow of the proposed method. A two-dimensional matrix f (x, y) with M columns and N rows can be used to describe a digital image, with the intersections of the columns and rows being referred to as pixels (picture element) or the smallest component of an image. There are several different color models used in color picture processing. The present work considers images of 224 X 224 dimensions. The RGB (red, green, and blue) space considers three different color components to represent images. In the present work RGB images of paddy leaves are used to train the model as well as to draw inferences.

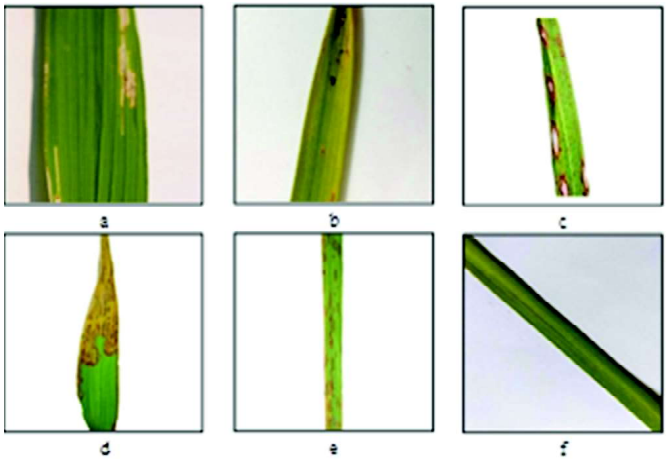

Fig. 1: Sample data a-f Bacterial Leaf Blight, Leaf Blast, Leaf Scald, Narrow Brown Spot, Brown Spot and healthy paddy leaves respectively.

Table 1: Dataset Description

Disease Category	No. of Training Images	No. of Testing Images
Bacterial Leaf Blight	350	88
Brown Spot	373	93
Leaf Blast	363	91
Leaf Scald	358	90
Narrow Brown Spot	352	88
Healthy	371	93
Total No. of samples	**2167**	**543**

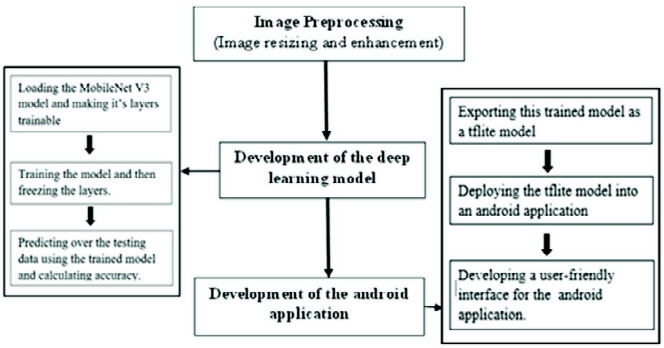

Fig. 2: Flowchart of the Workflow

Development of the Deep Neural Network Model

Supervised Classification is applied on the rice leaf dataset to detect the five different categories of paddy diseases and the healthy one. Since the target model will be deployed in a smart phone a light weight network is to be trained for this purpose. Hence, in the present work Mobile Net Large V3 architecture is used to train the classifier. Mobile Net Large Version 3 is used for performing the classification because of the given two reasons – firstly, this model has proved to return very high accuracy in various other image classification-based projects that have already been developed. Secondly, because Mobile Net Large Version 3 model works efficiently in the mobile run times, within the constraints of space and the processing requirements. This DNN works with much efficiency with the performance constraints of mobile runtimes. Mobile Nets are architecture that have been introduced by Google, which is a family of Computer Vision models that are based on Tensor Flow.

In contrast to the hand-designed previous version of Mobile Net, Mobile Net V3 relies on automated machine learning (Auto ML) to find the best possible architecture in a search space friendly to mobile computer vision tasks. Auto ML is thought to be about method choice, model hyper parameter adjustment, iterative modelling, and model assessment. It aims to simplify machine learning operations by using less code and avoiding human hyper-tuning. The MobileNetV3 (Howard et al., 2019; Paul et al., 2023) search space builds on multiple recent advances in architecture design that has been adapted for the mobile environment. Firstly, a new activation function called hard-swish (h-swish) has been introduced which is based on the Swish nonlinearity function. The critical drawback of the Swish function is that it is very inefficient to compute on mobile hardware. So, instead they have used an approximation that can be efficiently expressed as a product of two piecewise linear functions. Additionally, the mobile-friendly squeeze-and-excitation block has been introduced, which replaces the classical sigmoid function with a piecewise linear approximation. Combining h-swish plus mobile-friendly squeeze-and-excitation with a modified version of the inverted bottleneck structure introduced in MobileNetV2 yielded a new building block for MobileNetV3 (Fig. 3).

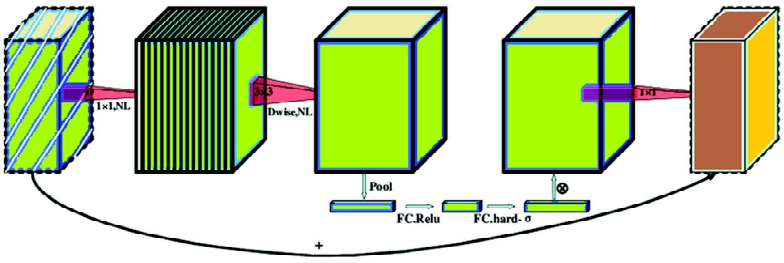

Fig. 3: Mobile Net V3 block

In the present work the Mobile Net V3 is trained using the training samples of the dataset and tested with the testing samples. Subsequently, the performance of the model is measured with respect to accuracy of detection. The performance of the model is also compared with other state of the art methods. After achieving satisfactory performance, the model is considered for integrating in the Android application for smart phone.

Development of the Mobile Application

Android Studio was used as the integrated development environment (IDE) for developing and building the android application, because of it's convenient and flexible editor. The task of development of the android application starts with the creation of a new project. The important prerequisite for making the app function efficiently is to load all the necessary dependencies, plugins, repositories, python, and machine learning libraries (Paul et al., 2022a). The minimum software development kit (SDK) version that the application will function is in SDK version 29. The next important step is to frame the design of the applications, with all the text views, action buttons and image views, which is done in the XML file. The python code for performing the image preprocessing step is imported into the resources folder of the android application and then the trained Mobile Net V3 model in the tflite format is imported into the ML resource folder of the android application. The java programme controls every action button, image view, the preprocessing and prediction. After all these steps are carried out, the app is built and worked on a virtual android device. After successful installation and working of the app in the virtual device, it is made to be built in an .apk format, such that it can be installed in a physical android device with minimum SDK 29.

There are two action buttons in the application, which are the SELECT button and the CAPTURE button.

The SELECT action button, will trigger the action to lead the user of the app to the gallery of the android device, such that he or she can select the image of the rice leaf, whose disease is to be detected and after the selection of the image, the next automatic triggered operation would be to put the selected image as input to the ML model. The prediction made by the model is then displayed in the text view. The function of the CAPTURE action button is very much similar, with a slight difference that it allows the user to capture an image using the android device camera.

Results and Discussion

In the present work, firstly the deep neural network model is trained using the training images and subsequently, performance of the model is evaluated using the testing dataset. The detailed description of the training and testing dataset is given in the '*Data used*' subsection of this article. Finally, an Android application is developed that helps in identification of paddy leaf disease with a smart phone. The results are discussed in this section.

Model Performance

The number of epochs is a hyperparameter of gradient descent that controls the number of complete passes through the training dataset. The present model is trained for 10 epochs to achieve a stable model performance with increasing accuracy and decreasing loss. The present model archives 95.50% accuracy with the testing dataset. The performance of the present method is also tested with other different models using the same dataset and their results are analyzed and depicted in Fig. 4. After achieving a satisfactory performance, the model is finalized to deploy in an Android application.

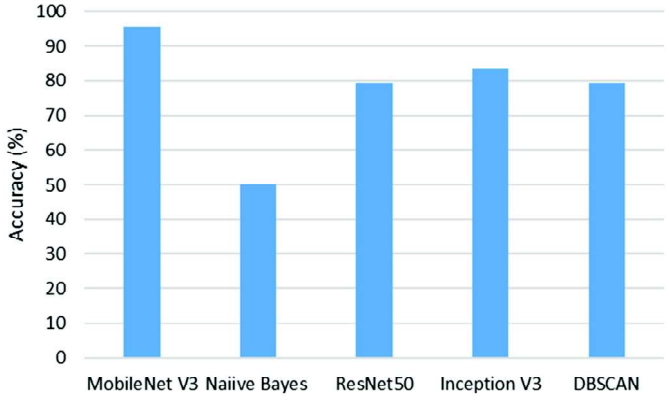

Fig. 4: Model performance comparison

User Interface of the Mobile Application

The android application developed using the trained model is deployed in a smart phone. Fig. 5 shows the user interface of the application. The home page of the application is having two action buttons: 'SELECT IMAGE' and 'CAPTURE IMAGE' (Fig. 5a). User can either select an available picture of a rice leaf from the local device as shown in figure 5b or can capture a new photo by the phone's camera through the app. This input image is subsequently analysed by the system to identify the disease. Finally, the predicted disease name is shown on the screen along with the input photo of the rice leaf (Fig. 5c).

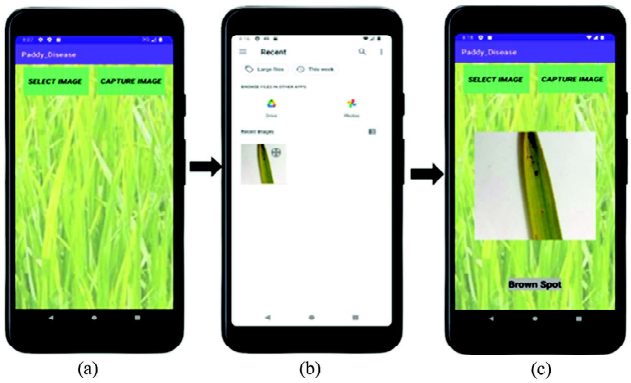

Fig. 5: User interface of the mobile application: (a) The home screen of the application to capture/ select an image of rice leaf, (b) Option for selecting available picture from local device, (c) System predicted disease name is shown on the screen along with the photo of the input rice leaf

Conclusion

The present deep neural network gives better output for disease prediction in rice plant using Mobile Net V3 architecture compared to other tested methods. Moreover, it works efficiently within the constraints of a mobile device, providing it an edge over other deep learning based models. One of the most sophisticated mobile computer vision architectures is still Mobile Net. The present work achieved a good accuracy for on-device rice plant disease detection from the affected rice leaf photo. In future, more disease type may be included by enhancing the training dataset for developing more generic application for this purpose. The present version of the mobile app works independently without being connected to the Internet. However, if the disease name along with the location details of the mobile device is collected systematically at a centralized server, a spatial map of rice plant disease can be created to help which would serve as an important input in monitoring the rice plant disease status at spatio-temporal dimension.

References

Ade, fiqri (2023). https://www.kaggle.com/datasets/adefiqri12/riceleafsv3 (accessed on 13 October 2023)

Ahmed, K., Shahidi, T. R., Alam S. M. I. & Momen, S. (2019). Rice Leaf Disease Detection Using Machine Learning Techniques, Int. Conf. on Sustainable Technologies for Industry 4.0, 1-5, doi: 10.1109/STI47673.2019.9068096.

Anandhan, K. & Singh, A. S. (2021). Detection of Paddy Crops Diseases and Early Diagnosis Using Faster Regional Convolutional Neural Networks, Int. Conf. on Advance Computing and Innovative Technologies in Engineering, 898-902, doi: 10.1109/ICACITE51222.2021.9404759

Deng, R., Tao, M., Xing, H., Yang, X., Liu, C., Liao, K. & Qi, L. (2021). Automatic Diagnosis of Rice Diseases Using Deep Learning. Front. Plant Sci. 12:701038. doi: 10.3389/fpls.2021.701038.

Dutta, S.,et al. (2021). Elephant–railway conflict minimisation using real-time video data and machine learning. J Reliable Intell Environ 7, 315–324. https://doi.org/10.1007/s40860-021-00131-8.

Howard, A. et al. (2019). Searching for MobileNetV3, IEEE/CVF Int. Conf. on Computer Vision, Seoul, Korea (South), 1314-1324, doi: 10.1109/ICCV.2019.00140.

Joshi, P., Das, D., Udutalapally, V., Pradhan, M. K. & Misra, S. (2022). Rice BioS: Identification of Biotic Stress in Rice Crops Using Edge-as-a-Service," in IEEE Sensors Journal, 22(5), 4616-4624, doi: 10.1109/JSEN.2022.3143950.

Kanjilal, S. & Paul, A. (2023) Detection of Water Bodies from Satellite Images: A Deep Learning Based Technique, 3rdInt. Conf. on Smart Generation Computing, Communication and Networking, Bangalore, India, 1-6, doi: 10.1109/SMARTGENCON60755.2023.10441880.

Khan, R., Singh, A. K., Sreenivasu, SVN, Mahalaxmi, U.S.B. K; Sharma, H. & Patil, D. (2022). Hybrid Feature-Based Disease Detection in Plant Leaf Using Convolutional Neural Network, Bayesian Optimized SVM, and Random Forest Classifier/ 0146-9428, 10.1155/2022/2845320.

Krishnamoorthy, N., Prasad, L.V.N., Kumar C.S.P., Subedi, B., Abraha, H.B. & Sathishkumar, V.E. (2021). Rice leaf diseases prediction using deep neural networks with transfer learning, Environmental Research, 198, 111275, doi: https://doi.org/10.1016/j.envres.2021.111275.

Paul, A., Tripathi, D. & Dutta, D. (2018) Application and comparison of advanced supervised classifiers in extraction of water bodies from remote sensing images. Sustain. Water Resour. Manag. 4, 905–919. https://doi.org/10.1007/s40899-017-0184-6

Paul, A., Bandyopadhyay, S. & Raj, U. (2022). Brick kiln detection in remote sensing imagery using deep neural network and change analysis, Spatial Information Research, 607–616, DOI: https://doi.org/10.1007/s41324-022-00458-1.

Paul, A., Dutta, D. & Jha, C. S. (2022a). Open-Source Geospatial Technology for Coastal Asset Mapping and Management. In Y. Zhang, & Q. Cheng (Eds.), Geographic Information Systems and Applications in Coastal Studies. IntechOpen. https://doi.org/10.5772/intechopen.104321.

Paul, A., Chauhan, S. & Dutta, D. (2023). Mobile based image interpretation and geotagging using artificial intelligence and open-source geospatial technology, Applied Geomatics, DOI: https://doi.org/10.1007/s12518-023-00522-x.

Paul, A., Bhattacharyya. S. & Chakraborty, D. (2023a). Estimation of Shade Tree Density in Tea Garden using Remote Sensing Images and Deep Convolutional Neural Network, Journal of Spatial Science, 68(3): 415–429, doi: https://doi.org/10.1080/14498596.2021.2013966.

Pothen, M. E. & Pai, M. L. (2020). Detection of Rice Leaf Diseases Using Image Processing, 4thInt. Conf. on Computing Methodologies and Communication, pp. 424-430, doi: 10.1109/ICCMC48092.2020.ICCMC-00080.

Prajapati, Harshad kumar, Shah, Jitesh & Dabhi, Vipul (2017). Detection and classification of rice plant diseases. Intelligent Decision Technologies. 11. 357–373. 10.3233/IDT-170301.

Rumy, S.M.S.H., Hossain, M.I.A., Jahan, F. & Tanvin, T. (2021). An IoT based System with Edge Intelligence for Rice Leaf Disease Detection using Machine Learning, IEEE Int. IOT, Electronics and Mechatronics Conf., 1-6, doi: 10.1109/IEMTRONICS52119.2021.9422499.

Saha, S. & Ahsan, S.M.M., (2021). Rice Disease Detection using Intensity Moments and Random Forest, Int. Conf. on Info. and Communication Tech. for Sustainable Development, 166-170, doi: 10.1109/ICICT4SD50815.2021.9396986.

Shah, Jitesh, Prajapati, Harshad kumar & Dabhi, Vipul. (2016). A survey on detection and classification of rice plant diseases. 1-8. 10.1109/ICCTAC.2016.7567333.

Shrivastava, V. K., Pradhan, M. K., Minz, S. & Thakur, M. P. (2019). Rice Plant Disease Classification Using Transfer Learning of Deep Convolution Neural Network", ISPRS – Int. Archives of the Photogrammetry, Remote Sensing and Spatial Information Sciences, 423, 631–635. doi:10.5194/isprs-archives-XLII-3-W6-631-2019.

Sreejith, R. & Balaji, N. V. (2022). Emerging neutrosophic C means clustering based segmentation for rice plant leaf disease detection. International Journal of Health Sciences, 6(S2), 10212–10223. https://doi.org/10.53730/ijhs.v6nS2.7730

Statista (2023). https://www.statista.com/statistics/1080013/india-economic-contribution-of-paddy/ (accessed on 13 October 2023)

Upadhyay, S.K. & Kumar, A. (2022). A novel approach for rice plant diseases classification with deep convolutional neural network. Int. j. inf. tecnol. 14, 185–199. https://doi.org/10.1007/s41870-021-00817-5

Wang, Y., Wang. H. & Peng, Z. (2021). Rice diseases detection and classification using attention based neural network and Bayesian optimization, Expert Systems with Applications, 178, 2021,114770, ISSN 0957-4174.

Indian Cartographer, Vol. 44, No. 1 & 2, pp. 70-80
ISSN: 0972-8392 © INCA, 2024

Spatio-Temporal Analysis of Ground Water Scenario in Nagaur District of Rajasthan

Govind Singh
Department of Geography, Jai Narain Vyas University, Jodhpur (India)
Email: govind5550@gmail.com

Abstract

During the last few years modern facilities have brought about significant changes in the lives of people as well as many job opportunities. This study aims to find out the effects of 35 years' worth of groundwater table up-down in the study area during pre and post-monsoon timespan. Earth's interior, soil taxonomy, physiography and changes in land utilization, all impact the infiltration capacity, which determines the groundwater depth. The present study intends to conduct a spatial-temporal analysis of ground water status in Nagaur district of Rajasthan during 1985-2020. The main sources of water resources in the district are rainfall and groundwater. But, rainfall occurs only during two months of the monsoon, during which there are very few rainy days. Thus, the entire geographical situation is impacted by the reliance on subsurface water resources. The study has examined the groundwater situation, its causes, its effects on the local economy and community, and it also tries to provide some suitable solutions. The findings are expected to assist the decision-makers in crafting water policies that are suited for the local population's well-being. With a water level depth of<10 mbgl, the 1985 result indicates that the depth of the water level was quite promising for the entire Ladnu block. In 2020, the number of wells with a water level depth of less than 10 meters below ground level (mbgl).is limited to three in the north side of the Ladnu block, two in the middle of the Degana block, and two in both the northern and southern parts of the Nagaur block. The portion which has a water level depth of more than 60 mbgl appears to have devoured the remainder of the district. The relationship between irrigation and groundwater depletion, which has impacted crop output, is evident in the cropping and irrigation patterns in the district.

Keywords: Water Table, Water Level, Infiltration, Spatial, Temporal, Pre & Post Monsoon.

Introduction

Water is crucial for all forms of life, including human existence. The prevailing natural aridity has led to a severe shortage of freshwater in Rajasthan, particularly in its western part. The groundwater in this part of Rajasthan is both deep and rapidly depleting due to overexploitation, and it is of poor quality, posing significant health risks to the local population. In this area, groundwater serves as the primary resource for numerous industries, with irrigation accounting for the majority of its usage (Singh, 2023). This research is targeted to examine the effects of variations in the groundwater table in Nagaur district of Rajasthan before and after the monsoon seasons. Factors such as earth's inner activities, soil condition, physical features, and changes in land use all influence the infiltration capacity, which in turn determine the depth of the groundwater. The study intends to understand the spatial-temporal scenario of underground water in Nagaur district during 1985-2020. To precisely find out random values in some specific locations, one type of stochastic model geostatistical analysis is considered useful (Uyan & Cay, 2013). Geostatistical models are based on spatial

correlation, usually represented by variograms (Wameling, 2003).

The Study Area

The study is carried out in Nagaur district of Rajasthan, which is situated between 26°25′ N and 27°40′ N latitudes and 73°10′ E and 75°15′ E longitudes, encompassing an area of 17,778 square kilometer. It shares its borders with Bikaner and Churu districts to the north; Sikar and Jaipur districts to the east; Ajmer and Pali districts to the south; and Jodhpur district to the west. It accounts for 5.2 percent of the total area of Rajasthan. The district comprises 13 tehsils with their headquarters in Nagaur, Didwana, Merta, Jayal, Nawa, Parbatsar, Degana, Ladnun, Makarana, Khinwsar, Kuchaman, Riyanbadi, and Mundwa. It is divided into 14 blocks (Panchayat Samitis): Nagaur, Mundwa, Jayal, Merta, Riyan, Degana, Didwana, Ladnun, Parbatsar, Makarana, Kuchaman, Nawa, Khinwsar, and Molasar.

The district has an arid to semi-arid climate, with a noticeable increase in rainfall over the past 30 years. The analysis of data revealed normal rainfall during 1901-1970 with 363.1 mm. The average annual rainfall for the period 2012-2021 is found to be 496.04 mm as against 616 mm in 2021. This is indicative of a deviation of 41.08% from normal rainfall and 19.50% from average rainfall. Due to its desert location, the district experiences extreme heat in summer and cold in winter. The topography is relatively flat, with a westward slope and elevations ranging from 250 meters above Mean Sea Level (MSL) in the south to 640 meters above MSL in the north. The district's soil ranges from sandy loam to clayey loam, and its general geological formation is quaternary. Some areas have early Cambrian geological formation, while others have Mesoproterozoic formation.

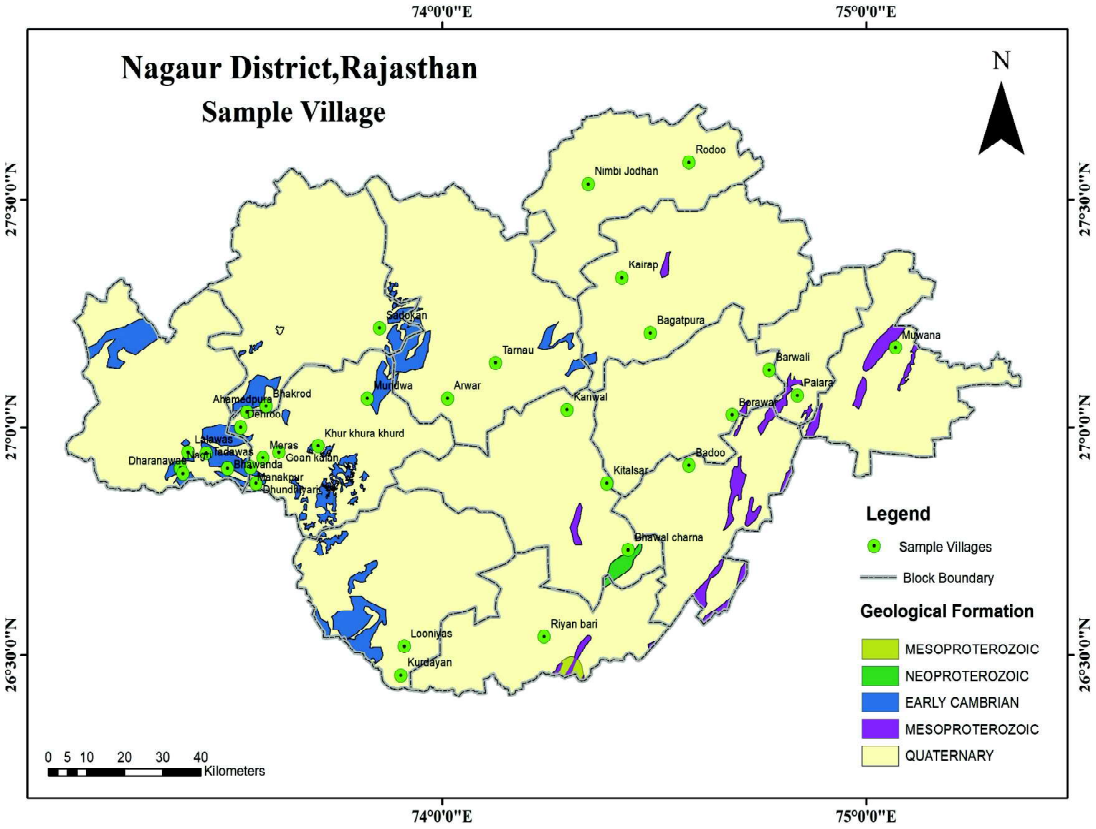

Fig. 1: Location map of the study area showing geological formations
(Prepared by Author based on GSI Resource map)

Materials and Methods

The data for underground water status was meticulously gathered from numerous wells in the Jodhpur region by the dedicated team of the groundwater department. The precise coordinates of the locations of wells were recorded in degrees, minutes, and seconds, and then entered into an Excel document. To ensure compatibility with GIS

software, the coordinates were converted from the "DMS format" to decimal degrees. The data was then exported to a .csv format before being transformed into a shape file format for further analysis. The groundwater level data, along with the corresponding well locations, were initially presented in x, y location format. Subsequently, annual maps were created to visualize the pre and post-monsoon groundwater levels, showing the spatial distribution and seasonal fluctuations. These maps were generated using the geostatistical toolbox in ArcGIS 10.5, with Kriging employed as the interpolation method. Kriging operates under the assumption that locations closer to known points will have similar values to those located farther away can be found in the neighboring areas, indicating a consistent pattern across the region.

To validate the accuracy of the data, an "empirical semi variogram" was utilized, and the resulting graph was analyzed to assess spatial autocorrelation. This analysis involved evaluating the line representing points in the empirical semi-variogram cloud graph to identify the best match. Additionally, the spatial autocorrelation between predicted and measured locations was examined, and Kriging weights were allocated to a variety of measured parameters. The resulting water level maps for every year effectively depict the spatial changes based on the available well data. It was noted that the number of wells with available data increased in recent years compared to previous years, indicating an improvement in data collection efforts.

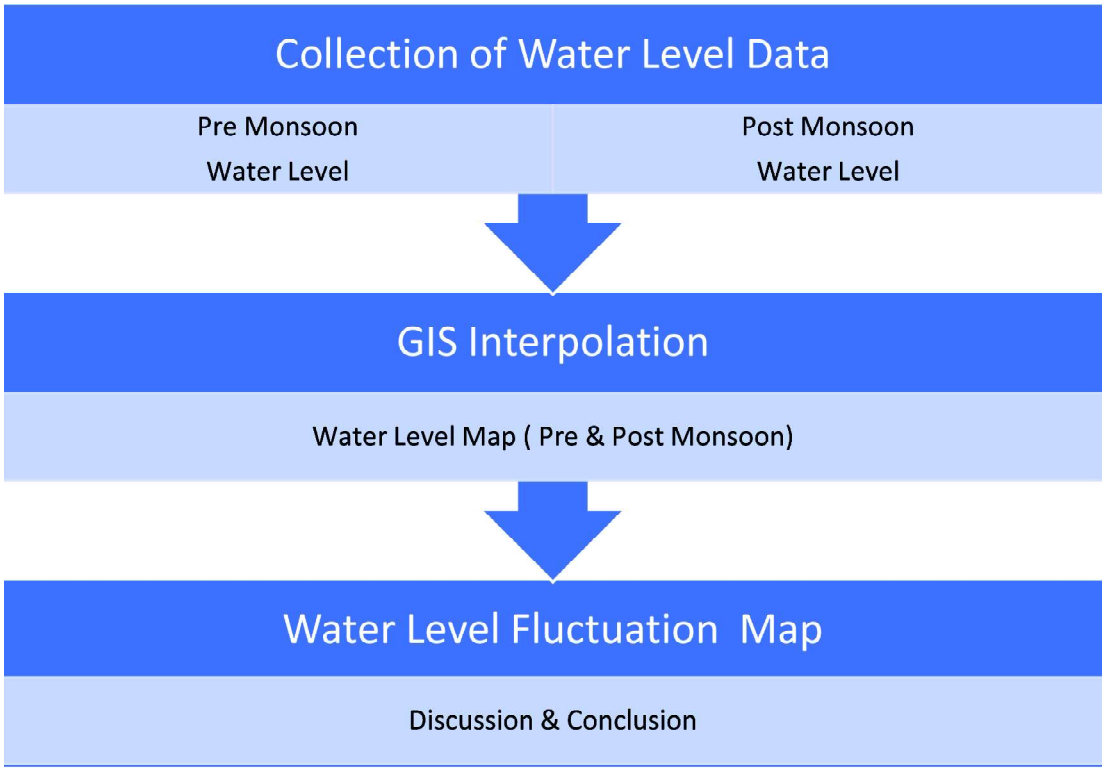

Fig. 2: Flow chart of materials and methods

Results and Discussions

The Central Ground Water Board (CGWB) has established a network of stations called National Hydrograph Network Stations (NHS) for monitoring Groundwater Level. As of March 31, 2021, the study area comprises 36 such National Hydrograph Network Stations, including 18 dug wells and 18 piezometers. The data has been analyzed as discussed below.

Spatial Variation in Water Table

In 1985, the water levels in the Ladnu block were generally favorable, with depths of less than 10 meter below ground level (mbgl). Encouraging water level was also observed in east Jayal and west Didwana. The horizontal half of the Didwana block had a water level of <20 mbgl before the starting of the monsoon, which increased up to 30 mbgl in the post-monsoon season of

the same year. Additionally, the conditions nearby Kuchaman, Makrana, and Degana blocks appeared favourable during before and after monsoon seasons. However, the northern portions of Nagaur and Mundwa showed discouraging scenario with water level depths > 60 mbgl.

The water level in 1990 is indicative of the area with favorable water level, with most of the areas with good water level spread around northern part of Ladnu, east Nagaur, and western part of Jayal block, and around the eastern Parbastar, west Nawa, and mid of Riya Badi. Conversely, the area with low water levels appeared to have expanded in the western part of Nagaur district. However, in the post-monsoon season, some wells in the western part showing a rise in water level.

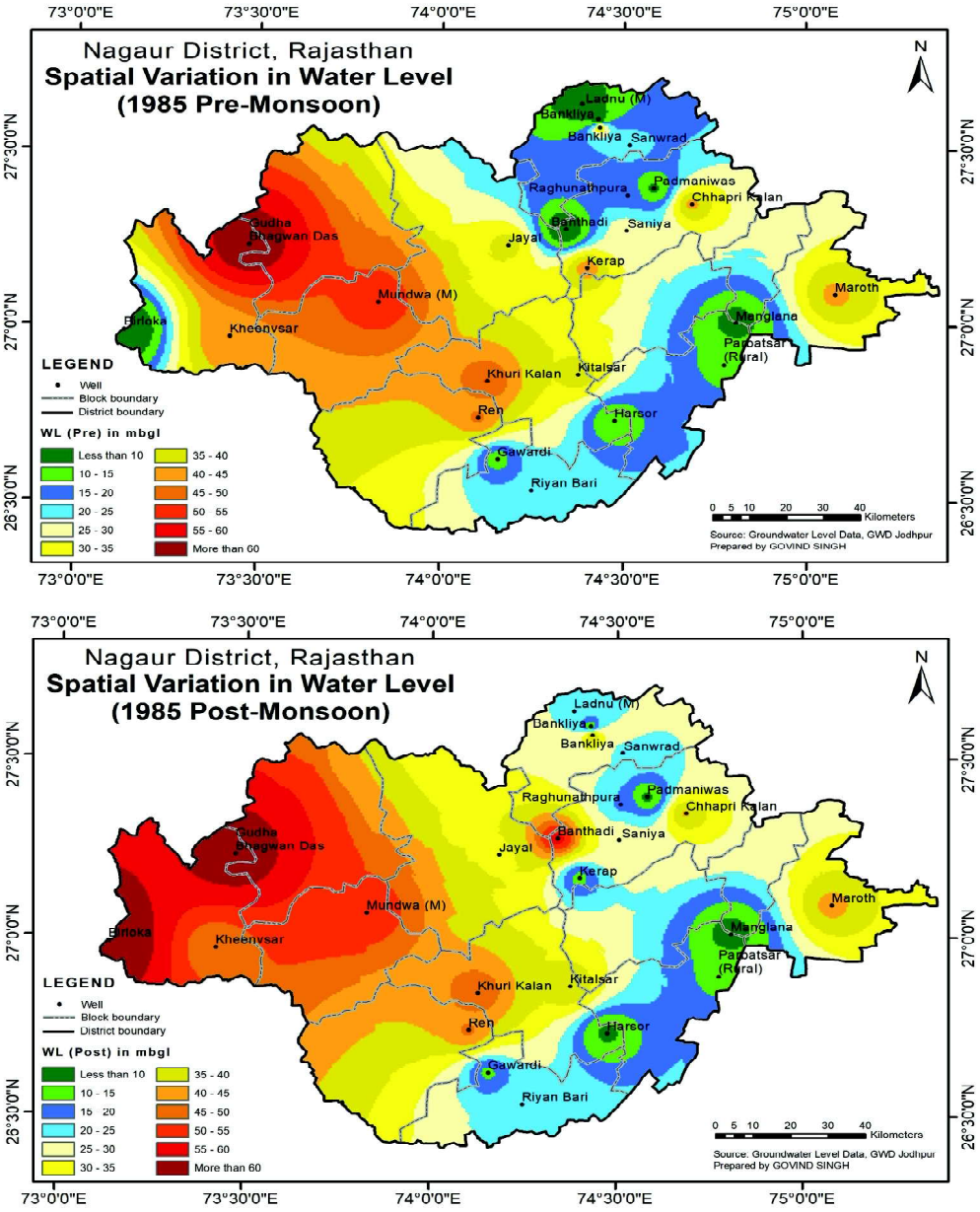

Fig. 3: Spatial variation in Pre & Post Monsoon Water Level of Nagaur District, 1985

In 1995, during both seasons, an upliftment was observed in the area with water levels exceeding 60 meter below ground level (mbgl) in the middle part of the district. Even wells with favourable depths of < 10 mbgl also appeared to be shrinking. The data for before and after the 1995 monsoon showed the highest positive groundwater scenario in RiyaBadi, followed by other locations, such as Phardod, Deh, Jhordaof Jayal,

Kanwaladof Parbatsar, Palara, Meethdi, Nawa of Nawa block, Koliya of Didwana, Upadara, Ledi of Ladnu, and Anandpura. By the year 2000, the condition regarding depth of water level got further worsened, with wells in the northern part shrinking and the area with water level exceeding 60 mbgl expanding to the west. Based on current boundaries, the entire Khimsarpanchayat samiti, southof Mundava, and eastern Merta experienced a significant decline in groundwater level in 2000. A small area near Riyanbari and scattered spots throughout the district, such as Rodoo, Ledi, Upadara, Soneli, Phirod, Phardod, and Deh, had water level up to 25 mbgl, which is considered satisfactory. The remaining areas of the district are in an alarming stage.

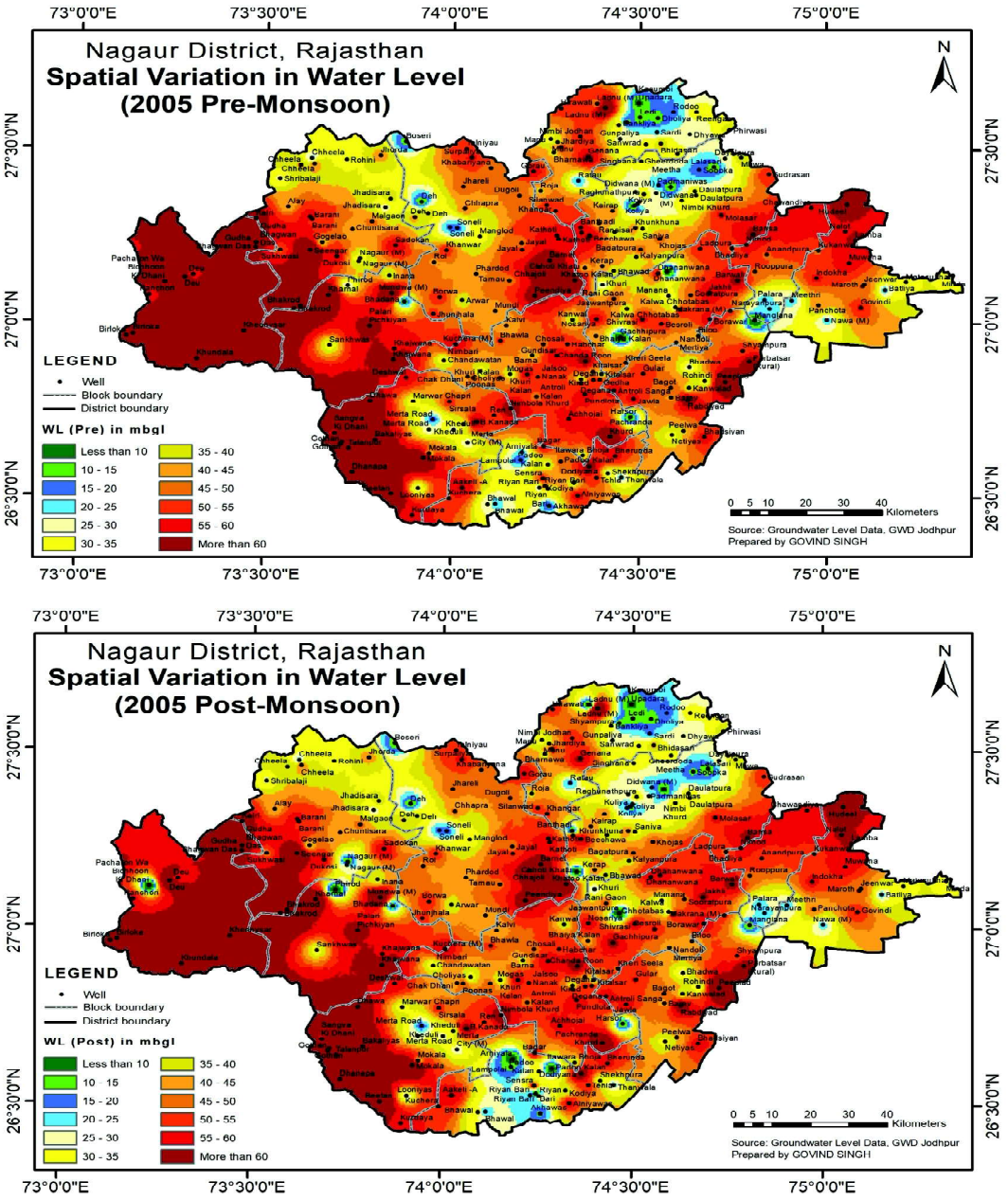

Fig. 4: Spatial variation in Pre & Post Monsoon Water Level of Nagaur District, 2005

In 2005, an increment in the depth of water level between 15 and 20 meters below ground level (mbgl) was noted in the southern part of the Riyan Bari block and northern Ladnu and Didwana block during both pre and post monsoon seasons. It was observed that the area under the alarming water level depth had expanded, particularly around the southern part of the Riyan Bari block and the northern part of the Ladnu and Didwana blocks.

Additionally, the western part of the district consistently maintained a water level depth of above 60 meters below ground level.

The 2010 data revealed an encouraging upliftment in water depth level after the monsoon season in the southern part of the Kheenswar block, which was considered a rare phenomenon in recent years. Furthermore, the wells in the northern part of Ladnu, central part of Didwana, and Degana experienced a motivating rise in water level, ranging between 10 and 20 mbgl.

In 2015, a sudden increment in the depth of water level was observed in many wells north of the study area in the pre-monsoon season. However, after the monsoon period, the water level fell to a worrying stage of >60 mbgl. The consistent change in the water level depth in 2015 prompted a need for closer monitoring and analysis in the affected areas.

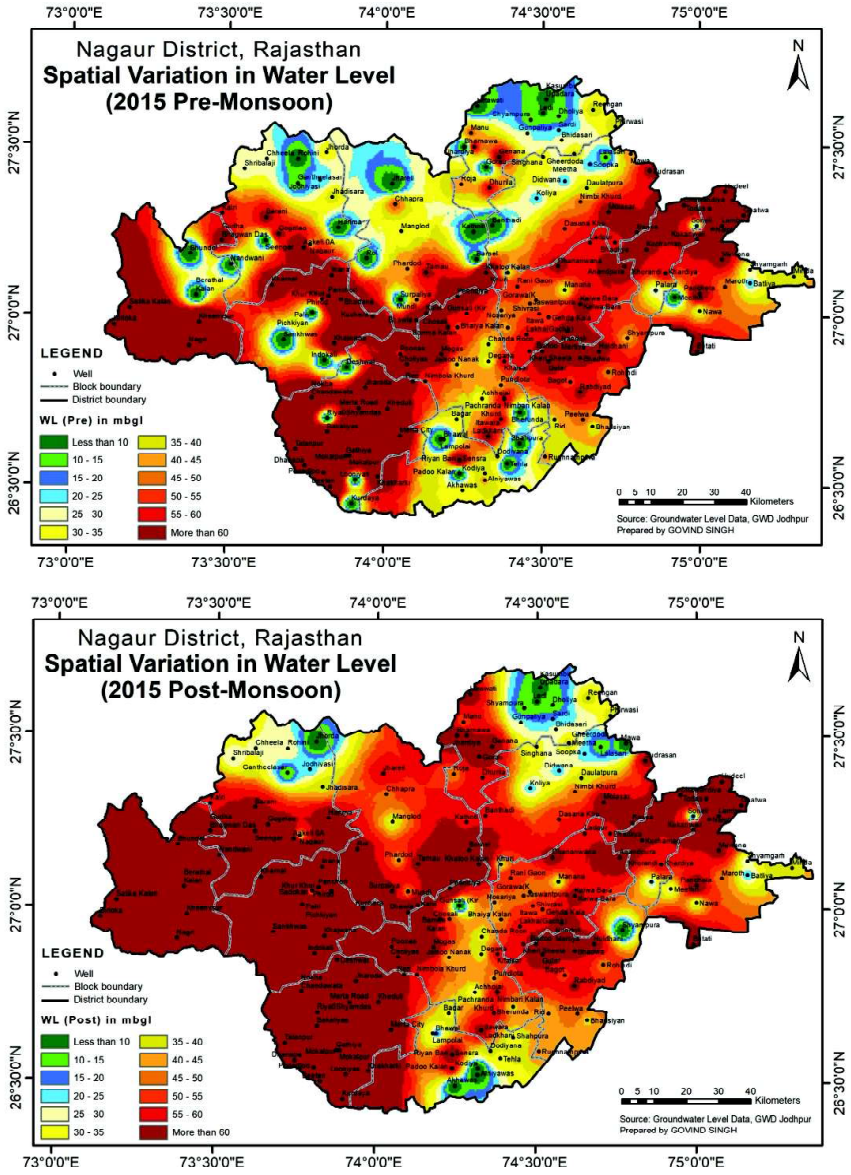

Fig. 5: Spatial variation in Pre & Post Monsoon Water Level of Nagaur District, 2015

In 2020, the level of groundwater in the district was found to be in a critical stage. Only 3 wells in the northern part of Ladnun block, 2 wells in the middle portion of Degana block, and 2 observing wells in both the northern and southern parts of Nagaur block witnessed a water level depth of < 10 meter below ground level (mbgl). The rest of the district is likely to be facing water level depths of > 60 meter below ground level (mbgl).

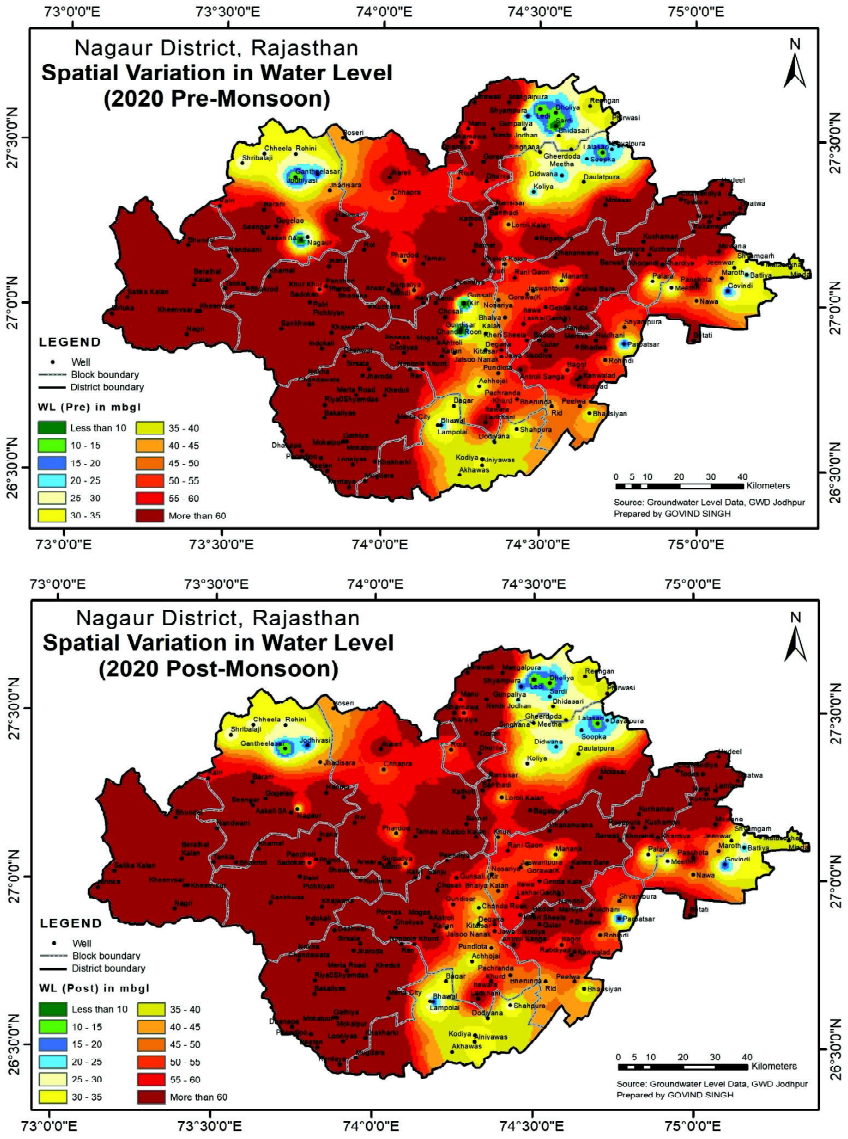

Fig. 6: Spatial variation in Pre & Post Monsoon Water Level of Nagaur District, 2020

Table 1: Well Wise Categorization of Depth to Water Level (DTWL) In Nagaur District, 2021-22

Sl. No.	Point of Time for Observation	No of well analyzed	DTWL mbgl		No of well in different Ranges					
			Min	Max	0 to 2 (m)	2 to 5 (m)	5 to 10 (m)	10 to 20 (m)	20 to 40 (m)	>40 (m)
1	May, 2021	21	10.65	112.1	0	0	0	4	9	8
2	August, 2021	20	10.35	114	0	0	0	6	9	5
3	November, 2021	21	10.65	115.1	0	0	0	5	9	7
4	January, 2022	19	9.53	114	0	0	2	3	8	6

Source: Ground Water Year Book, 2021-22, Rajasthan

Throughout 2021-22, on an average of 20 wells were assessed at various intervals. The depth of nearly all wells exceeded 10 meter, with the depth to water level averaging between 10.3 meter below ground level (mbgl) and 113.8 mbgl. In May 2021, 43% of observations were between 20 meter and 40 meter in depth, while 38% were above 40 meter. By August 2021, 45% of observations fell within the 20-40 meter depth range, with only 25%

above 40 meter, suggesting a potential improvement would be likely due to favourable monsoon conditions. Finally, in January 2022, almost 10% of observations displayed a positive shift into the 5 to 10meter range.

Groundwater Level Fluctuation

The fluctuations in groundwater levels are considered important indicators of groundwater recharge and stress on water resources. These fluctuations are influenced by changes in groundwater storage that occur due to various factors, including aquifer recharge and drainage. Additionally, changes in pressure can result from water mass loading and unloading above the aquifer surface. These processes are important to monitor and understand in the management of groundwater resources and the assessment of potential impacts on the surrounding environment.

In Nagaur district, the fluctuations in groundwater level during 1985-2020 were calculated by comparing the water level depth data of pre and post-monsoon seasons. These fluctuations provide a clear image of the groundwater scenario of each year. In 1985, the most extreme groundwater fluctuations were observed in the western part of the study area, particularly in the west of Khinwsar block, with fluctuations ranging from -58.17 to -34.59 meter. The rest of the district experienced fluctuations between -3.69 and 1.96 meter (Table 2).

By 1990, the groundwater level fluctuations had changed significantly. The south-western part of Merta block experienced the most negative fluctuations, ranging from -14.95 to -5.33 meter. Most of the district experienced fluctuations between -1.09 and 4.03 meter. In 1995, the groundwater fluctuation scenario shifted, with negative fluctuations moving from the western part of the district to the central, southern and eastern parts, ranging from -8.43 to -3.09 meter. Positive fluctuations were observed in the most upper and the most lower parts, ranging from 2.14 to 5.89 meter.

The year 2000 saw erratic groundwater level fluctuations, with most of the central and eastern parts experiencing negative fluctuations ranging from -2.93 to -0.74 meter, and in some areas from -0.73 to 0.72 meter. Only the westward side of Merta and Mundwa, and some north-western part of Ladnu experienced positive fluctuations of 7.23 to 15.09 meter.

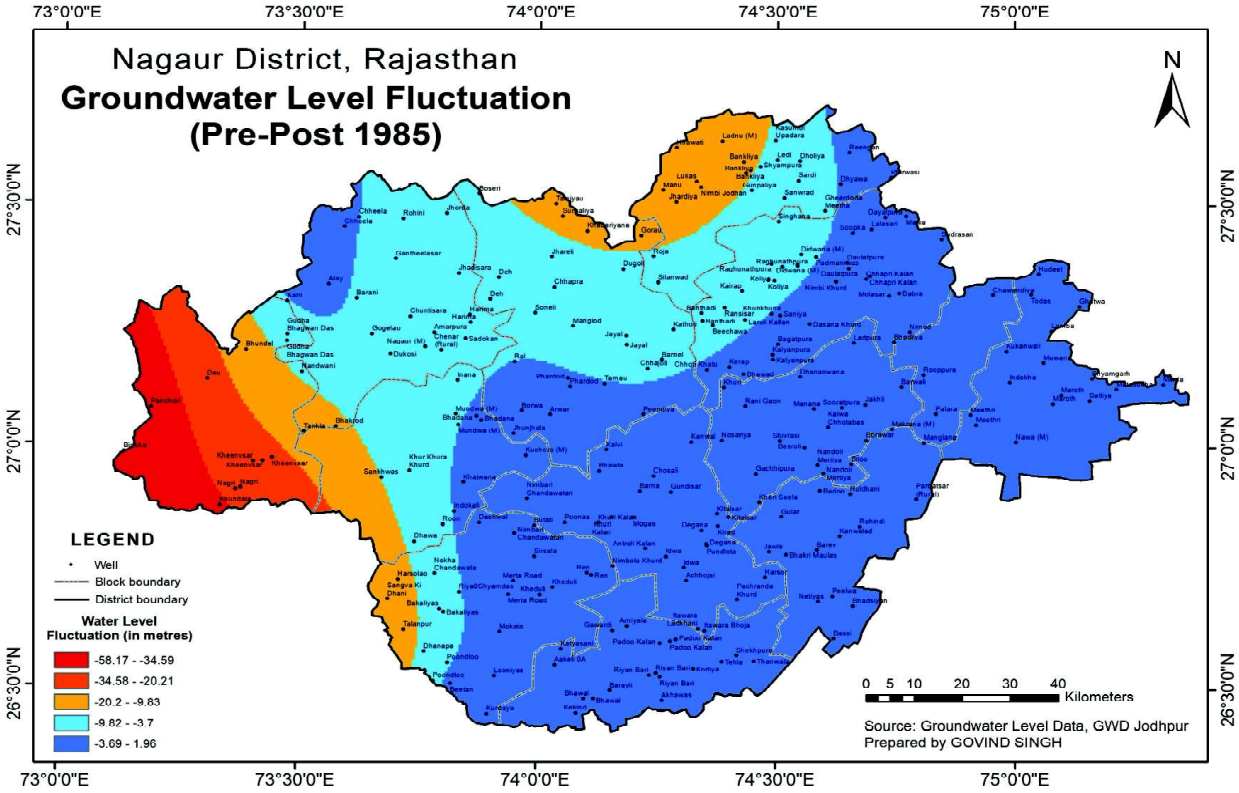

Fig. 7: Pre & Post Monsoon Ground Water Level Fluctuation in Nagaur District, 1985

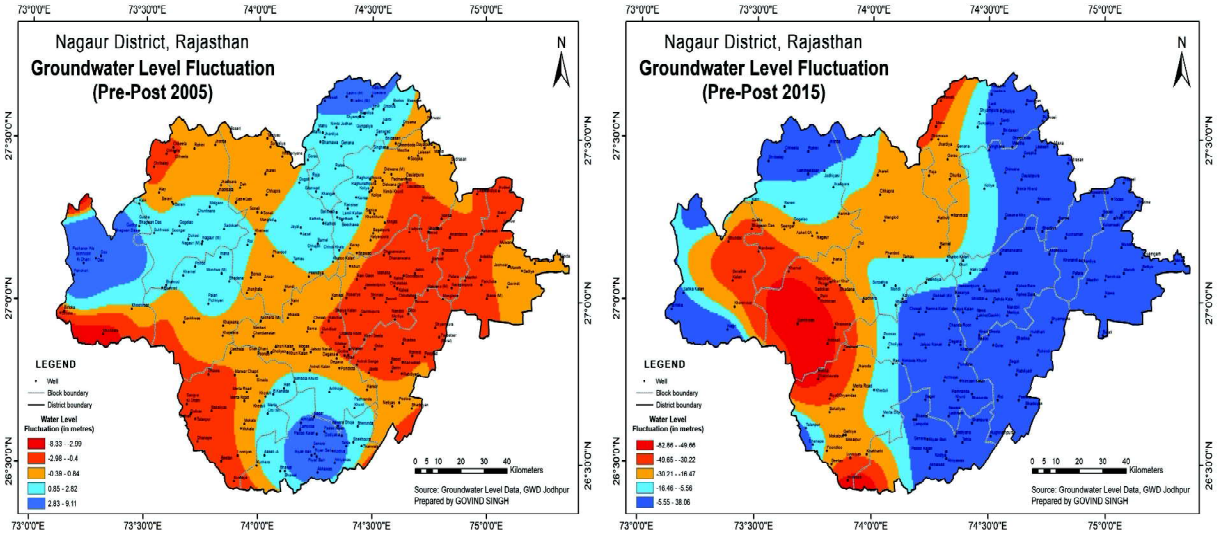

Fig. 8: Pre & Post Monsoon Ground Water Level Fluctuation in Nagaur District, 2005 & 2015

In 2005, there was minimal negative fluctuation in groundwater level, and it was mainly confined to the western part of the district. Most of the region experienced motivating fluctuation in both the pre-monsoon and post-monsoon seasons. During 2010, the highest demotivating groundwater fluctuation occurred in the western and southern parts of the district, ranging between -18.58 and -4.67 meter. The highest motivating fluctuation between the pre-monsoon and post-monsoon seasons for 2010 ranged from 53.3 to 163.33 meter and was dispersed around the south-western parts of the study area.

In 2015, negative fluctuation was centered near the south-western part, encompassing the Merta and Mundva blocks, with values ranging from -82.66 to -49.66 meter. The entire eastern part of the district showed a hybrid fluctuation ranging from -5.55 to -38.06 meter. For 2020, the highest encouraging fluctuation values were found near the south-eastern part, including Riyan Badi and some parts of the Parbastar block, ranging from 2.8 to 5.68 meter. The discouraging fluctuation values ranging from -5.32 to -3.2 meter were largely found in the middle western part of the study area, including Mundwa and Nagaur blocks.

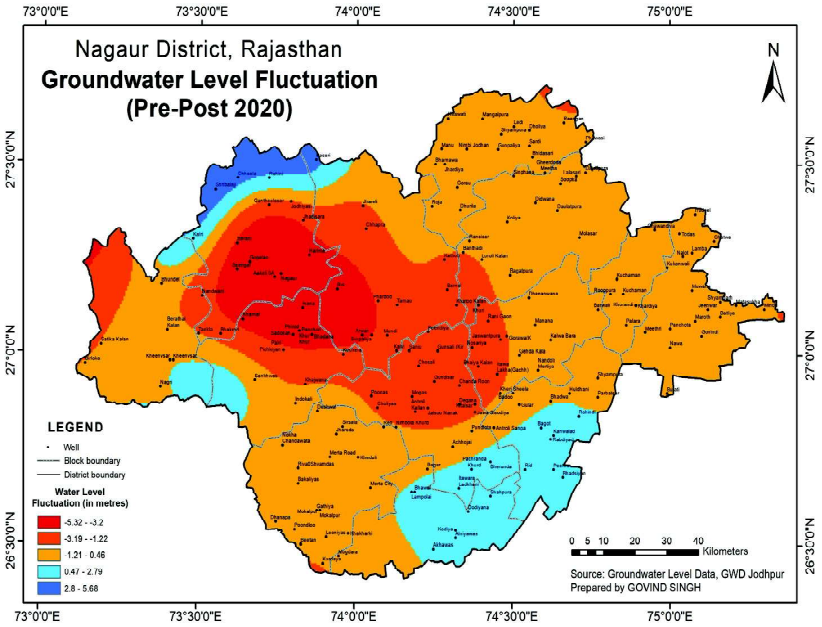

Fig. 9: Pre & Post Monsoon Ground Water Level Fluctuation in Nagaur District, 2020

Table 2 indicates that on an average of 20 wells were examined over the decade spanning 2011-2021. The data reveals that 59.26% of the wells experienced an increase in water level, while 40.74% experienced a decrease. The average recorded increase ranged from 0.22 to 11.21 meter, and the decrease ranged from 0.31 to 6.24 meter.

In January 2022, a remarkable 73.68% of the wells recorded an increase in water level as compared to the January average for the period 2012-2021. This extraordinary improvement is attributed to exceptionally good monsoonal rains in some years.

Table 2: Temporal Categorization of Water Level Fluctuation in Nagaur District, 2011-21

Sl. No.	Period of Time for Observation	No of well analyzed	Range of Fluctuation (m)				No. of Wells representing Fluctuation						Total No. of wells	
			Rise		Fall		Rise			Fall				
			Minimum	Maximum	Minimum	Maximum	0 to 2	2 to 4	>4	0 to 2	2 to 4	>4	Rise	Fall
1	During May, 2021 with Respect to Decadal Average of May (2011 To 2020)	21	0.45	11.75	0.08	8.79	3	5	4	4	2	3	12	9
2	During August, 2021 with Respect to Decadal Average of August (2011 To 2020)	20	0.15	14.36	0.5	11.49	1	6	4	6	1	2	11	9
3	During November, 2021 with Respect to Decadal Average of November (2011 To 2020)	21	0.24	9.35	0.27	9.83	2	5	4	6	0	4	11	10
4	During January, 2022 with Respect to Decadal Average of January (2012 To 2021)	19	0.05	9.39	0.39	4.88	5	4	5	2	1	2	14	5

Source: Ground Water Year Book, 2021-22, Rajasthan

Conclusion

The foregoing discussion reveals that Nagaur district is facing challenges of depleting water table and lower water quality. Poor water management could lead to a severe tragedy in the future. Hence, both the government and the general public need to be aware of the importance of conserving every drop of water. Water conservation is necessary for its sustainability. To improve groundwater resources, there is a strong need for a groundwater recharge system, including rooftop rainwater storage, the construction of various land barriers, dams, anicuts, and other suitable recharge structures at appropriate locations. Traditional water harvesting techniques used in the past should also be revived. The government should encourage community-based water management solutions like nadi, nada, johad, talai, talab, khadeen, and individual practices like 'Tankas' for rainwater collection. Modern irrigation techniques should be promoted for the sustainable use of water resources. High water-consuming crops should be discouraged, and farmers should be motivated to grow alternate low water-consuming crops. Additionally, high water-consuming animal husbandry, especially buffalo husbandry, should be replaced by low water-consuming animals. The situation can be mitigated through encouraging social forestry, saving orans, gochars, agores, etc., and educating people through various awareness programmes.

References

Arslan, H. (2012). Spatial and temporal mapping of groundwater salinity using ordinary kriging and indicator kriging: The case of Bafra Plain, Turkey. Agricultural Water Management, 113, 57–63

Borges, Pd. A., Franke, J., da Anunciação, Y. M. T., Weiss, H., & Bernhofer, C. (2016). Comparison of spatial interpolation methods for the estimation of precipitation distribution in Distrito Federal. Brazil Theoretical and Applied Climatology, 123(1), 335–348. https://doi.org/10.1007/s00704-014-1359-9

District Statistical Outline-District Nagaur (Yearly Volumes from 1996 to 2020), Directorate of Economics and Statistics, Jaipur, Govt. of Rajasthan.

GOI Central Ground Water Board (2013). Ground Water Information Nagaur District Rajasthan. Western Region Jaipur.

GOI Central Ground Water Board (2022). Ground Water Year Book,2021-22, Rajasthan. Western Region Jaipur.

Kumar, V. (2007). Optimal contour mapping of groundwater levels using universal kriging — a case study. Hydrological Sciences Journal, 52, 1038–1050. https://doi.org/10.1623/hysj.52.5.1038

Singh, Govind. (2023). Animal Husbandry and Its Sustainability Dimensions in Nagaur District of Rajasthan: A Geographical Appraisal, Ph.D. Thesis, Jai Narain Vyas University, Jodhpur, Rajasthan

Uyan, M., & Cay, T. (2013). Spatial analyses of groundwater level differences using geostatistical modelling. Environmental and Ecological Statistics, 20, 633–646.

Wameling, A. (2003). Accuracy of geostatistical prediction of yearly precipitation in Lower Saxony. Environmetrics, 14, 699–709.

Acknowledgements

This research has been conducted under a project titled “Geographical Analysis of Ground Water Scenario in Nagaur: A Case Study of Mundwa Block” sponsored by Rajasthan Higher Technical Quality Improvement Scheme (RHTQIS).

Guidelines to Author

1. Manuscripts in prescribed format can be submitted through email only to the Chief Editor (editorinca.journal@gmail.com) any time.
2. Manuscript should be submitted in both Word document (doc, docx) and Portable Document Format (pdf) along with a brief cover letter addressed to the Chief Editor, Indian Cartographer, INCA mentioning the following:
   (a) Category of the manuscript (e.g. Research Paper, Research Article, Review Article, etc.)
   (b) What is the study all about? (in brief)
   (c) How your study contributes to the aims and objectives of the journal?
   (d) Why do you think the journal should accept your paper for publication?
   (e) Please include a list of Names, email IDs (institutional ID is preferred), designations, affiliations, field of expertise and contact details of 3 potential reviewers for your manuscript.
   (Please note that your manuscript may or may not be sent to these potential reviewers)
3. Manuscript should be typed in A4 page using font Times New Roman with 12 font size and 1.5 spaces along with 1// margin on all sides of the paper.
4. The paper has not been submitted elsewhere, for which a certificate needs to be given at the time of submission.
5. Equations and tables used in the paper should be editable.
6. Divide your article into clearly defined and numbered sections. Subsections should be numbered 1.1 (then 1.1.1, 1.1.2, ...), 1.2, etc.
7. Please avoid foot notes.
8. Aurhors are advised to check their writing with Grammarly or any other similar free software to avoid grammatical errors.
9. The paper should accompany a plagiarism check report with Similarity Index of below 10%.
10. For further details please visit https//www.incaindia.org/inca-journal.

INDIAN NATIONAL CARTOGRAPHIC ASSOCIATION

Survey of India, Uppal, Room No. 234, APGDC Block
Hyderabad – 500 039 (Telangana, India)
Email: secretarygeneralinca935@gmail.com
Fax No.: 040-2702217
Website: https://www.incaindia.org
Registration No.: 789 of 1979

Executive Committee [2023-2024]

Office Bearers

President : Shri Hitesh Kumar S. Makwana, *IAS, Survey of India, Dehradun*

Past President : Dr. Prakash Chauhan, *NRSC, Hyderabad*

Senior Vice-President : Dr. Binod Kumar Singh, *NATMO, Kolkata*

Vice-President-I : Prof. (Dr.) Bimal Kumar Kar, *Gauhati University, Guwahati*

Vice-President-II : Vice Admiral L.S. Pathania, *NHO, Dehradun*

Vice-President-III : Dr. S.K. Srivastav, *NRSC, New Delhi*

Secretary General : Shri Manchala Santhosh, *Survey of India, Hyderabad*

Secretary-I : Shri Narendran J., *NRSC, Hyderabad*

Secretary-II : Shri Rajesh Kumar Khatri, *NHO, Dehradun*

Treasurer : Shri P. Krishnaiah, *NRSC, Hyderabad*

Chairman, Editorial Board : Prof. (Dr.) Bimal Kumar Kar, *Gauhati University*

Executive Committee Members

Dr. U. N. Mishra (Survey of India); Shri S. V. Singh (Survey of India); Rear Admiral Peush Pawsey (NHO, Dehradun); Dr. R. A. Prasad (NHO, Dehradun); Dr. B. K. Ramprasad (NHO, Dehradun); Shri M. P. Gupta (NHO, Dehradun); Dr. A. K. Bera (NRSC, Jodhpur); Shri Amitabh (ISRO-SAC, Ahmedabad); Dr. Vandita Srivastava (IIRS, Dehradun); Shri Sajikrishnan K. (NATMO, Kolkata); Dr. Sraboni Bhattacharya (NATMO, Kolkata); Dr. Gaurav Kalotra (Panjab University, Chandigarh); Dr. Sucheta Mukherjee (S.S. College, Kalyani University)

ISSN: 0972-8392

INDIAN CARTOGRAPHER

Volume 44 Number 1 & 2 2024

Published by Indian National Cartographic Association (INCA), INCA Headquarters, Survey of India, Uppal, Room No. 234, APGDC Block, Second Floor, Hyderabad – 500 039 (Telangana, India)
Website: https://www.incaindia.org/inca-journal Email: secretarygeneralinca935@gmail.com

Printed at: M Tact Multimedia, Guwahati, Assam **Chief Editor:** Prof. Bimal K. Kar